



DESIGN AND CONTROL OF FLAPPING WING MICRO AIR VEHICLES

DISSERTATION

Michael L. Anderson, Major, USAF

AFIT/DS/ENY/11-12

**DEPARTMENT OF THE AIR FORCE
AIR UNIVERSITY**

AIR FORCE INSTITUTE OF TECHNOLOGY

Wright-Patterson Air Force Base, Ohio

APPROVED FOR PUBLIC RELEASE; DISTRIBUTION UNLIMITED

The views expressed in this thesis are those of the author and do not reflect the official policy or position of the United States Air Force, Department of Defense, or the U.S. Government.

This is declared a work of the United States Government and is not subject to Copyright protection in the United States.

AFIT/DS/ENY/11-12

DESIGN AND CONTROL OF FLAPPING WING MICRO AIR VEHICLES

DISSERTATION

Presented to the Faculty

Department of Aeronautics and Astronautics

Graduate School of Engineering and Management

Air Force Institute of Technology

Air University

Air Education and Training Command

In Partial Fulfillment of the Requirements for the
Degree of Doctor of Philosophy in Aeronautical Engineering

Michael L. Anderson, BS, MS, PE

Major, USAF

September 2011

APPROVED FOR PUBLIC RELEASE; DISTRIBUTION UNLIMITED

AFIT/DS/ENY/11-12

DESIGN AND CONTROL OF FLAPPING WING MICRO AIR VEHICLES

Michael L. Anderson, BS, MS, PE

Major, USAF

Approved:

Richard Cobb, PhD (Chairman)

Date

Mark Reeder, PhD (Member)

Date

Ronald Coutu, Jr., PhD (Member)

Date

Accepted:

M. U. Thomas, PhD
Dean, Graduate School of
Engineering and Management

Date

Abstract

Flapping wing Micro Air Vehicles (MAVs) continues to be a growing field, with ongoing research into unsteady, low Re aerodynamics, micro-fabrication, and fluid-structure interaction. However, research into flapping wing control of such MAVs continues to lag. Existing research uniformly consists of proposed control laws that are validated by computer simulations of quasi-steady blade-element formulae. Such simulations use numerous assumptions and cannot be trusted to fully describe the flow physics. Instead, such control laws must be validated on hardware. Here, a novel control technique is proposed called Bi-harmonic Amplitude and Bias Modulation (BABM) which can generate forces and moments in 5 vehicle degrees of freedom with only two actuators. Several MAV prototypes were designed and manufactured with independently controllable wings capable of prescribing arbitrary wing trajectories. The forces and moments generated by a MAV utilizing the BABM control technique were measured on a 6-component balance. These experiments verified that a prototype can generate uncoupled forces and moments for motion in five degrees of freedom when using the BABM control technique, and that these forces can be approximated by quasi-steady blade-element formulae. Finally, the prototype performed preliminary controlled flight in constrained motion experiments, further demonstrating the feasibility of BABM.

Acknowledgments

This work represents a milestone in a lifetime journey that is my education. Therefore, every one of my teachers, relatives and mentors has contributed, and I am grateful for their wisdom and encouragement. Specifically, my MAV work was aided by dozens of people. I thank Dr. Dan Jensen, of the US Air Force Academy, who first recruited me in 2006 to work with Cadets on MAV research, thus starting me down this path. Dr. Greg Parker of AFRL/Air Vehicles was critical to this effort in providing funding and initial guidance and introducing me to Dr. Dave Doman and Mr. Mike Oppenheimer, who pointed me in the right direction at the very start and have been encouraging and assisting me ever since. The staff of AFRL's MAV Fab Lab, including Lt's Eric Wolf, Danny Lacore, and Luis Miranda helped me develop a fabrication capability. I am similarly indebted to Mr. Jay Anderson and the entire ENY lab staff for their continuing support, as well as Dr. Peter Collins and Mr. Charles McNeely of ENG for lending the use of their laser. Dr. Robert Wood of Harvard University and his students, especially Mr. Peter Whitney and Mr. Andy Baisch, were very generous in their collaboration. Further, Dr. Larry Dosser, Mr. Kevin Hartke, and Mr. Chris Taylor of the Mound Laser and Photonics Center very generously provided hundreds of hours of laser micromachining *pro bono*. The later prototypes simply would not exist without MLPC. My classmates in the AFIT MAV group; Maj Ryan O'Hara, Lt Nate De Leon, Lt Nate Sladek, Lt Bob Dawson, Capt Travis Tubbs, Lt John Tekell, and Capt Garrison Lindholm provided immeasurable support on a daily basis. I am grateful for their friendship. I thank the members of my committee for taking the time to evaluate my ideas and provide honest feedback. Finally, I must thank my wife and boys for their patience and understanding over the last three years.

Michael L. Anderson

Table of Contents

	Page
Abstract	iv
Acknowledgments	v
Table of Contents	vi
List of Figures	viii
List of Tables	xiii
List of Symbols and Abbreviations	xiv
1. Introduction	1
1.1 Research Challenges for Flapping Wing Micro Air Vehicles	2
1.2 Problem Statement	3
1.3 Research Approach	4
2. Background and Previous Work	6
2.1 Flapping Wing Aerodynamics	8
2.2 Biological Flight Stability and Control	16
2.3 Design Considerations for Flapping Wing Micro Air Vehicles	23
2.4 Concepts for the Control of Micro Air Vehicles	40
3. A Novel Technique for Flapping Wing Control of MAVs	61
3.1 Split-cycle, Constant Period, Amplitude Modulation	62
3.2 Bi-harmonic Amplitude and Bias Modulation	71
3.3 Remaining Assumptions	82
4. Flapping Wing MAV Design and Fabrication	84
4.1 Flapping Mechanism Design and Fabrication	85
4.2 Wing Design and Fabrication	103
4.3 Fuselage and Actuator Design and Fabrication	109

5. Open Loop Flapping Wing Trajectory Control	120
5.1 Frequency Response of MAV Drive Actuator to Non-Harmonic Forcing	121
5.2 Discrete Harmonic Plant Compensation	128
5.3 Resonant Non-harmonic Wing Flapping.....	143
6. Evaluation of BABM for Flapping Wing MAV Control	149
6.1 Experiment Equipment and Procedures	150
6.2 Preliminary Cycle-Averaged Forces and Moments	155
6.3 Improved Cycle-Averaged Forces and Moments.....	163
7. Conclusions	180
7.1 Research Conclusions	182
7.2 Significant Contributions	185
7.3 Recommendations for Future Work.....	187
Appendix.....	191
Bibliography	202
Vita	212

List of Figures

	Page
Figure 2.1. Flapping wing kinematics.....	9
Figure 2.2. Wing geometry for blade element model.	11
Figure 2.3. Flying animal allometry and MAV sizing, data from [21, 35, 58, 75].....	25
Figure 2.4. Comparison of linear actuators to insect flight muscle.	30
Figure 2.5. Insect flapping mechanism and its mechanical analogies	32
Figure 2.6. Flapping mechanism for PZT bimorph cantilever actuator.....	33
Figure 2.7. Double crank-slider mechanism of the Harvard Robofly [92]. Rotary joints are shown in blue, fixed right angle joints are shown in red.....	36
Figure 2.8. Kinematic variants for controlling the Harvard Robofly (adopted from [37]).	49
Figure 2.9. Coordinate frame definitions from [28]	52
Figure 2.10. Split-cycle constant period frequency modulated waveform.	54
Figure 2.11. Normalized angular position, velocity and acceleration resulting from a split- cycle waveform	55
Figure 3.1. Comparison of the bi-harmonic waveform (Eq. 3.52, dashed) to the piecewise version (Eqs. 3.1 and 3.2).....	73
Figure 3.2. Comparison of approximate closed-form derivatives to exact numerical derivatives.	78
Figure 4.1. Four bar linkage kinematics.	86
Figure 4.2. Matlab animation of desired wing flap kinematics.	88

Figure 4.3. Transmission ratio; wing stroke angle vs. actuator tip deflection (blue). The green line is linear and is included for comparison.....	89
Figure 4.4. Link reaction force vectors (green) as the mechanism completes a stroke. ...	90
Figure 4.5. Link reaction forces (N) as a function of actuator tip displacement.	91
Figure 4.6. Carbon fiber and Kapton linkage.	95
Figure 4.7. Carbon fiber linkage 3-step manufacturing process.	96
Figure 4.8. Composite laminate assembly.	97
Figure 4.9. Folding of the flapping mechanism.	99
Figure 4.10. Precision alignment tools folding a version 4 flapping mechanism.	100
Figure 4.11. Measured wing kinematics compared to predicted and desired kinematics.	101
Figure 4.12. Evolution of the AFIT wing flapping mechanism.....	102
Figure 4.13. Sladek's initial wing manufacturing process.....	106
Figure 4.14. Improved wing manufacturing process.	107
Figure 4.15. Evolution of AFIT wing designs.	109
Figure 4.16. Version 2 fuselage, before and after folding.	110
Figure 4.17. Version 3 fuselage.	111
Figure 4.18. Version 4 fuselage assembly.	112
Figure 4.19. Harvard (left) and AFIT (right) actuator designs.	113
Figure 4.20. Actuator fabrication.....	117
Figure 5.1. Test rigging (only a single piezo actuator is shown for clarity).	124

Figure 5.2. Normalized actuator response to split-cycle input; measured velocity is in red, the desired velocity is in blue.....	126
Figure 5.3. Actuator's response to filtered split-cycle input with 100 Hz cutoff frequency.	127
Figure 5.4. Actuator's response to filtered input with 200 Hz cutoff frequency.	128
Figure 5.5. Velocity frequency response function of the wing flap actuator.....	129
Figure 5.6. Truncated Fourier series representation of the split-cycle waveform. On the left, $\Delta = 0.1$, on the right $\Delta = 0.4$	135
Figure 5.7. Fourier coefficients as a function of split-cycle parameter, Δ . The vertical lines (± 0.21) represent the proposed bounds on Δ	136
Figure 5.8. Phasor form Fourier coefficients as a function of split-cycle parameter, Δ . Note, each phase term has been normalized to the frequency of the 1 st harmonic by dividing it by its harmonic number.	137
Figure 5.9. Comparison of truncated Fourier sum representations of a split-cycle waveform for $\Delta = 0.3$	138
Figure 5.10. Actuator's response to the preconditioned 2-term Fourier waveform. The blue plots represent the preconditioned drive signal, the red lines are the measured actuator trajectory, the black lines represent the “desired” split-cycle trajectory....	141
Figure 5.11. Actuator's response to the preconditioned 3-term Fourier waveform.....	142
Figure 5.12. Frequency Response Function of the complete wing flapping mechanism.	144
Figure 5.13. Rigid body wing motion, visualized with a strobe lamp.	145

Figure 5.14. Wing response to the bi-harmonic waveform with DHPC.....	146
Figure 6.1. Flapping wing MAV prototype and test stand.	151
Figure 6.2. Simulink model for generating wing trajectories.	153
Figure 6.3. Test profile for asymmetric split-cycle test.	154
Figure 6.4. Time-varying lift data.	155
Figure 6.5. Force (mN) and moment ($mN\text{-}mm$) measurements for symmetric flapping, colors represent repeated trials.	157
Figure 6.6. Force (mN) and moment ($mN\text{-}mm$) measurements for asymmetric flapping.	159
Figure 6.7. Cycle-averaged F_z force resulting from split-cycle wing flapping.....	161
Figure 6.8. Frequency response functions of the right and left wings of the Version 3 MAV prototype.	164
Figure 6.9. Version 3 MAV prototype and test stand with axes labeled.	165
Figure 6.10. Improved force (mN) and moment ($mN\text{-}mm$) measurements for symmetric flapping.	166
Figure 6.11. Improved force (mN) and moment ($mN\text{-}mm$) measurements for asymmetric flapping.	167
Figure 6.12. Symmetric frequency modulation.	170
Figure 6.13. FRFs of left and right wings of version 2 prototype.	170
Figure 6.14. Symmetric split-cycle modulation.....	172
Figure 6.15. Asymmetric split-cycle modulation.	172

Figure 6.16. Laser vibrometer measurement of right wing trajectory for $\Delta = 0.05$ (top)	
and $\Delta = 0.15$ (bottom).	174
Figure 6.17. Examples of constrained motion MAV flight control experiments.	176
Figure 6.18. Pitch constrained motion experiment.	177
Figure 6.19. Video capture of the MAV pitching forward as a result of wing bias	
modulation.....	177
Figure 6.20. Yaw constrained motion experiment.....	178
Figure 6.21. Video capture of the MAV yawing as a result of asymmetric wing amplitude	
modulation.....	178

List of Tables

	Page
Table 2.1. Linear Actuator Characteristics	29
Table 2.2. Generalized Forces and Moments from [28]	59
Table 2.3. Control Derivatives from [29]	60
Table 3.1. Summary of kinematic variations used by various control techniques to impart aerodynamic wrench inputs.....	81
Table 4.1. Proposed linkage geometry.....	87
Table 4.2. Effects of geometry on predicted actuator performance.....	116
Table 4.3. Actuator resonance measurements.....	118
Table 4.4. Subsystem mass breakdown.	118
Table 5.1. Details of Test Equipment.	124
Table 5.2. Testing program.....	125
Table 6.1. Kinematic control parameters tested.....	155
Table 6.2. MAV parameters used for blade-element calculation.	159

List of Symbols and Abbreviations

A	stroke amplitude (rad)
AoA	Angle of Attack
α	Angle of attack (rad)
BABM	Biharmonic Amplitude and Bias Modulation
β	harmonic phase shift (rad)
c	chord length (m)
C_L, C_D	lift and drag coefficients
C_{rot}	rotation force coefficient
COM	Center of Mass
DHPC	Discrete Harmonic Plant Compensation
DOF	Degree(s) of Freedom
D_{LU}, D_{RU}	instantaneous drag during up-stroke for the left and right wing (N)
D_{LD}, D_{RD}	instantaneous drag during down-stroke for the left and right wing (N)
δ	split-cycle parameter (frequency shift of upstroke) (rad/s)
Δ	frequency normalized split-cycle parameter
E	Young's modulus (Pa)
EAP	Electro Active Polymers
η	wing stroke bias angle (rad)
FWMAV	Flapping Wing Micro Air Vehicle
FWF	Flapping Wing Flyer
FRF	Frequency Response Function

\vec{F}_R^{RWS}	instantaneous aero force on the right wing in the right wing spar frame (N)
\vec{F}_L^{LWS}	instantaneous aero force on the left wing in the left wing spar frame (N)
g	gravitational acceleration (m/s ²)
θ	elevation angle (rad), or beam deflection angle (rad)
I	rotational inertia (kgm ²)
ISR	Intelligence, Surveillance, and Reconnaissance
I_A	second moment of area (m ⁴)
J	advance ratio
J_n	Bessel function of the “nth” kind
K	beam stiffness (N/m)
k_L	blade element coefficient for lift terms
k_D	blade element coefficient for drag terms
L_i	length of the i th link (m)
L_{LU}, L_{RU}	instantaneous lift during up-stroke for the left and right wing (N)
L_{LD}, L_{RD}	instantaneous lift during down-stroke for the left and right wing (N)
l	characteristic length (m)
LEV	Leading Edge Vortex
LW	Left Wing
LWS	Left Wing Spar
m	vehicle/insect mass (kg)
MAV	Micro Air Vehicle
MEMS	Micro Electro-Mechanical Systems

MFI	Micromechanical Flying Insect
M	moment (Nm)
M_n	“nth” harmonic coefficient
M_x	roll moment (Nm)
M_y	pitch moment (Nm)
M_z	yaw moment (Nm)
p	roll rate (rad/s)
q	pitch rate (rad/s)
Re	Reynolds number
RC	Radio Controlled
RCM	Reciprocating Chemical Muscle
RW	Right Wing
RWS	Right Wing Spar
S	wing area (m ²)
SCCPFM	Split-Cycle, Constant-Period Frequency Modulation
SMA	Shape Memory Alloy
r	yaw rate (rad/s)
ξ	split-cycle phase shift
R	wing length (m)
\hat{r}	non-dimensional radial position
R_I^B	rotation matrix from inertial frame to body frame
R_{RWS}^B	rotation matrix from the right wing spar frame to the body frame

$\vec{r}_{cp,R}^B$	location of the center of pressure of the right wing with respect to the vehicle center of mass (m)
ρ	air density (kg/m ³)
σ	split-cycle frequency shift of down-stroke (rad), or stress (N/m ²)
Σ	frequency normalized frequency shift of down-stroke
T	wing-beat period (s)
T_D	duration of upstroke (s)
t	velocity in the z direction (m/s), or thickness (m)
τ	split-cycle deviation from nominal period (t)
U	potential energy (Nm)
U_t	wing tip velocity (m/s)
UAV	Unoccupied Air Vehicle
u	velocity in the x direction (m/s)
V_∞	freestream velocity (m/s)
v	velocity in the y direction (m/s)
w	width (m)
ω	flapping frequency (rad/s)
ϕ	wing stroke angle (rad)
$\dot{\phi}$	wing angular velocity (rad/s)
Φ	wing stroke amplitude (rad)
χ	body angle (rad)
Δx	x-axis distance from vehicle center of mass to wing root (m)

Δz	z-axis distance from vehicle center of mass to wing root (m)
x_{cp}	wing center of pressure location, measured along the X_{RWPU} and X_{LWPU} axes (m)
y_{cp}	wing center of pressure location, measured along the Y_{RWPU} and Y_{LWPU} axes (m)
y	horizontal position along wing length (m)
x_B	MAV body-fixed x-axis coordinate
y_B	MAV body-fixed y-axis coordinate
z_B	MAV body-fixed z-axis coordinate
X	force in the body-fixed x-direction (N)
Y	force in the body-fixed y-direction (N)
Z	force in the body-fixed z-direction (N)

DESIGN AND CONTROL OF FLAPPING WING MICRO AIR VEHICLES

1. Introduction

Unoccupied Air Vehicles (UAVs) have become pervasive in modern warfare by providing real-time intelligence, surveillance and reconnaissance (ISR) to the war-fighter without the limitations and massive logistics footprint of manned flight. Recently, Micro Air Vehicles (MAVs) have been proposed to provide a similar capability in a smaller package [25:29]. MAVs are autonomous vehicles with a maximum dimension of 15cm or less, weighing 90g or less [59:xiii]. They can be easily carried by small combat units and flown in confined spaces such as urban canyons, caves and indoors. MAVs will provide an organic ISR capability to small combat teams in the field, reducing or eliminating their reliance on larger UAVs that are in high demand, and increasing the team's autonomy.

MAVs of many shapes and sizes have been proposed but most have either fixed wings, rotary wings or flapping wings. Flapping wing MAVs (FWMAVs) have several advantages over fixed and rotary wing vehicles. They capitalize on several unsteady aerodynamic effects that generate additional lift at the low Reynolds numbers (Re) experienced by vehicles of this size, they have superior maneuverability including the ability to hover, and they mimic biological flyers so they are less conspicuous to potential adversaries.

1.1 Research Challenges for Flapping Wing Micro Air Vehicles

The design of flapping wing MAVs currently faces several significant challenges.

Perhaps the most significant are:

- Predicting the low Re and unsteady aerodynamics
- Designing for highly coupled fluid-structure interactions
- Micro-fabrication
- Stability characterization and control

Of these challenges, the most critical may be the stability and control problem because it is the farthest from a solution. All of the other challenges listed have been overcome to some degree and detailed in the literature.

Numerous researchers have built wings that generate lift and thrust, several have even lifted vehicles off the ground. So, while there is still uncertainty about flapping wing aerodynamics, our understanding is sufficient to generate useful aerodynamic forces. These same experiments prove that the problems of fluid-structure interactions and micro-fabrication are not insurmountable. The stability and control problem, however, has not been solved. While several vehicles have flown with flapping wings, all of them were either tethered to eliminate the need for control, or used a traditional fixed-wing tail to provide for the control while the flapping wings provided lift and thrust [93]. These latter designs help to prove the feasibility of flapping wing MAVs, but they severely limit their capabilities.

A fixed tail requires air flow over it to control the vehicle, greatly reducing or eliminating the MAV's ability to hover, a problem that grows with diminishing size. As

the vehicle scale is reduced, the control surfaces shrink and the corresponding Re is reduced, significantly reducing the aerodynamic efficiency of the control surfaces, and limiting their ability to generate adequate control forces and moments. So, while fixed tails may be suitable to control the shoebox-sized MAV's of today, they will be insufficient to control the insect-sized MAV's of tomorrow. Furthermore, one only need observe insects in flight to realize that flapping wing control provides for much greater maneuverability than achievable with a fixed tail. Insects are capable of translating in and rotating about all three spatial axes – decoupled 6 degree of freedom (DOF) maneuverability, something no tailed vehicle can come close to [35]. Therefore, to truly realize the potential of flapping wing flight, research should focus on flapping wing control and accept fixed tail control as only an intermediate step, not a final solution to the stability and control problem.

The research challenges for flapping wing MAVs listed above are important topics of ongoing research and all of them will play a role in flapping wing MAV development, but only the stability and control problem has not yet had a demonstrated solution [46, 92, 93]. It is the last step required to achieve un-tethered, truly autonomous flapping wing flight, and will continue to hold down the development of these vehicles until major strides are made towards solving it. Therefore, the stability and control of flapping wing MAVs is the most critical challenge to flapping wing MAV development.

1.2 Problem Statement

The goal of this research is to increase understanding of the stability and control problem. The concepts that have been proposed for flapping wing control to date can be

grouped in two categories; those requiring wings with multiple DOF and those requiring only one. The minimum DOF to be utilized that defines a flapping wing vehicle is the wing stroke angle, while multi DOF designs add modulation of angle-of-attack (AoA) and possibly stroke plane deviation as the second and third DOF. AoA modulation requires a mechanism such that the wing stroke and wing AoA can be prescribed arbitrarily (within reason) at any point in time. Given such a mechanism, simulations have shown that 6-DOF control can be achieved. Wing stroke velocity modulation requires a mechanism such that only the wing stroke velocity need be prescribed at any point in time, and simulations have likewise shown the concept's promise. Thus wing stroke velocity modulation has the advantage that it requires a simpler mechanism. This advantage is critical at this point in time because, to date, no flight-worthy mechanism has yet been built that has the ability to arbitrarily prescribe wing stroke velocity and wing AoA at the size and frequencies of interest. Thus, wing stroke velocity modulation is the only concept that can be tested on hardware at this point in time.

Thesis Statement: Direct modulation of each wing's stroke velocity alone is sufficient to provide a minimum 5-DOF control of an insect-sized flapping wing MAV.

1.3 Research Approach

The research will proceed as follows; a thorough survey of the literature will summarize the current state-of-the-art of flapping wing MAV control, a promising concept for controlling flapping wing MAVs will be identified, and finally, the selected concept will be implemented with hardware to determine its feasibility. The remainder of this document is arranged as follows; Chapter II provides a summary of previous work

described in the literature in the field of flapping wing MAVs, while Chapter III presents a novel technique for flapping wing control of MAVs. Chapter IV describes the design process used in building MAV prototypes (defined for the purposes of this document to be a fuselage, actuators, flapping mechanism and wings, while lacking a power source, sensors, command and control and a payload). Chapter V presents a novel technique for open-loop control of the flapping wing trajectory, Chapter VI describes experiments that demonstrate the feasibility of the proposed control technique, and Chapter VII summarizes the results of this research while suggesting the next steps to be taken in the field of flapping wing control of MAVs.

2. Background and Previous Work

Autonomous flight vehicles are nothing new. The first UAVs were developed as early as World War I in the form of guided munitions, later expanding their roles into radio controlled target drones, reconnaissance aircraft and glide bombs – forerunners of the modern-day cruise missile [59:6-7]. The first radio controlled (RC) aircraft flights in Germany in 1936 led the way to further refinement of small UAVs in the postwar era. The interest in small UAVs was held primarily by RC hobbyists as the military had no meaningful payloads small enough to be carried by such small vehicles. Today this situation is reversed. The rise of Micro Electro-Mechanical Systems (MEMS) technology has enabled the development of micro scale sensors, creating a practical use for smaller air vehicles. Unfortunately, it is not possible to merely scale down an aircraft to the desired dimensions. As was discovered with the development of MEMS technology, the physics of the small are different from that of the large (for example, friction is more important than gravity) [54:12]. For MEMS technology to progress, researchers had to develop a new understanding of these physics, and develop new techniques for overcoming and capitalizing on them. This is the case with small scale, or low Re aerodynamics today.

Re is the ratio of inertial forces to viscous forces, and as scale decreases, volume, and thus, mass and inertia decrease significantly. The accompanying decrease in Re is not merely a changed constant to be accounted for in an equation, it marks a significant change in the flow physics; so significant as to render conventional aircraft flight irrelevant [58:2]. As scale decreases and the aforementioned viscous forces become

more significant, the flow becomes more laminar, the boundary layer becomes critical and drag increases by as much as an order of magnitude while lift changes only slightly [58:36]. This has a debilitating effect on the aerodynamic efficiency (L/D) of airfoils at small Re . Furthermore, as the vehicle size is further limited, the fixed wing aircraft designer is tempted to use low aspect ratio wings to keep the chord length, and thus, Re as high as possible. Unfortunately, low aspect ratio wings come with their own host of problems, including strong wing tip vortices that increase drag, roll instability and highly nonlinear lift curve slopes [59:45-52]. Although scaling down conventional fixed-wing aircraft has resulted in successful MAVs as small as 6 inches, the physics strongly suggest that there is a lower bound for such aircraft [58,59,75].

Despite the difficulties of low Re physics, biology clearly demonstrates that small scale flight is possible. Indeed, two approaches to overcoming low Re physics are rotary and flapping wings, which enable a smaller scale vehicle to fly at a higher Re by moving the wings relative to the body. For example, the bumblebee, *bombus terrestris*, flaps its wings at approximately 150 hz, which corresponds to a wing velocity of approximately 3.83 m/s at the second moment of area point along the wing span (55% of wing span) [33, 34]. So even if the insect has no forward velocity, the wing still moves relative to the air at a Re of approximately 1200 [35:18]. When coupled with forward flight, the wing velocity relative to the surrounding air increases further, giving the insect the benefit of higher Re physics than it would otherwise experience. Rotary wing vehicles also enjoy this benefit of relative wing motion, and they may be a viable solution to the

MAV problem, however, they do not share the advantages of unsteady aerodynamic mechanisms that flapping wings experience.

Contrary to fixed wing aircraft under steady level flight, the aerodynamics of flapping wings is unsteady under all flight conditions owing to the oscillatory nature of the wing motion. Four unsteady mechanisms are consistently cited throughout the literature; leading edge vortex (LEV), rapid pitch up, wake capture, and clap-and-fling dynamics [1, 2, 35, 58, 75]. These mechanisms are difficult to predict with analytical methods, but it is clear that they provide a boost in lift, making flapping wing flight the preferred solution for MAVs as the scale is reduced.

2.1 Flapping Wing Aerodynamics

A hypothetical flapping wing can have up to four substantial DOF if structural elasticity is ignored (assume a rigid body). Two DOF are required to specify the orientation of the wing's leading edge in space, while a third is required to specify the rotation of the wing about the leading edge. In the case of most birds and some MAVs, a fourth major DOF is included to allow the wing tip to flex relative to the rest of the wing [58]. From this point forward, only 3 DOF wings will be considered. The current convention uses four parameters to describe the kinematics of a 3 DOF wing, as shown in Figure 2.1, these parameters are the stroke plane angle, β , the stroke angle, ν , the elevation angle, θ , and feathering angle/angle of attack, α . The excess parameter makes it possible to specify the stroke plane, an idealized reference used to specify the nominal trajectory of the wings (note that if the elevation angle is zero, then the wing is in the stroke plane). Despite adding complexity to an already complex problem, the stroke

plane actually does simplify the discussion of kinematics and flight forces. A fifth parameter, χ , is often used to specify the angle of the body above the horizontal, which gives a complete description of the insect's motion relative to the air, assuming no sideslip.

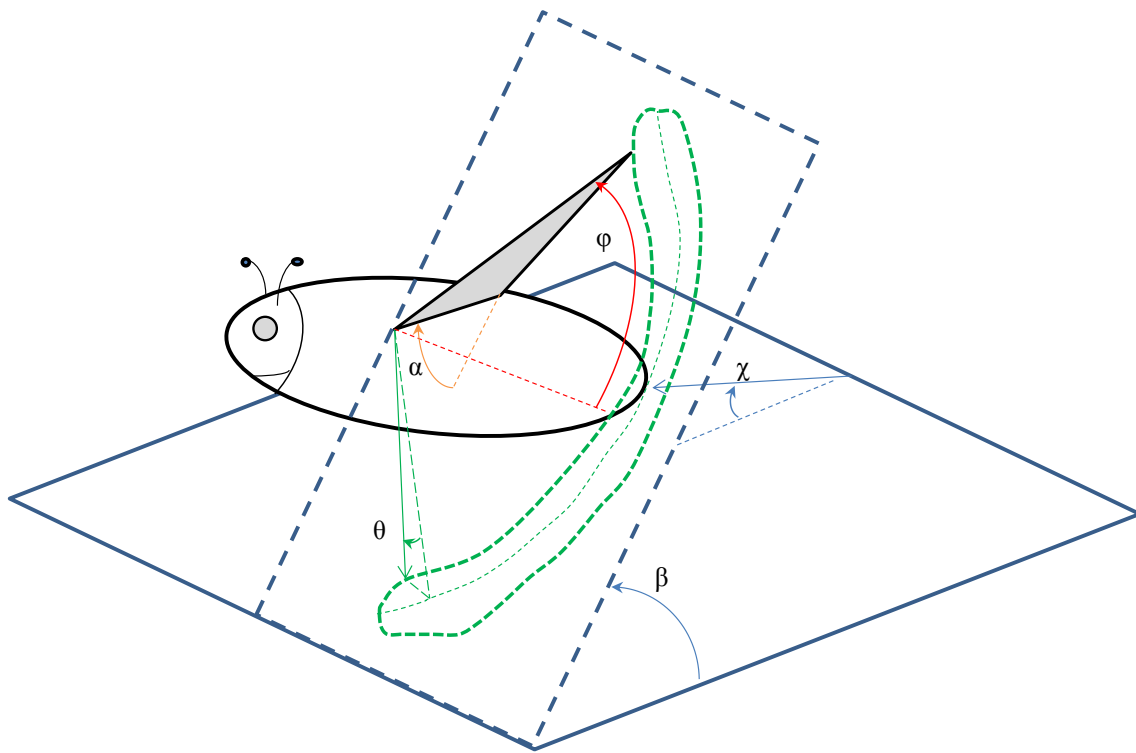


Figure 2.1. Flapping wing kinematics.

For a flapping wing flier (FWF) at any flight speed, the aerodynamic forces can be considered as a combination of forces resulting from quasi-steady mechanisms and unsteady mechanisms. The relative contribution of steady or unsteady mechanisms depends on the forward velocity of the FWF. As the FWF speeds up, the flow over the

wing approaches a steady-state condition, and a greater portion of the aerodynamic forces can be accounted for by the quasi-steady mechanisms. Conversely, as the forward velocity decreases, unsteady mechanisms dominate. A non-dimensional measure of the FWF's forward velocity that aids comparison across species and vehicles is the advance ratio [35:94]:

$$J = \frac{V_{\infty}}{2\Phi\omega R} \quad (2.1)$$

where V_{∞} is the *freestream velocity* of the FWF, Φ is the *wing stroke amplitude*, ω is *flapping frequency*, and R is the *wing length*. The advance ratio gives a ratio of the forward velocity to the wing tip velocity, and can therefore be used to quantify the relative importance of steady and unsteady aerodynamic mechanisms. Though there is no clear cutoff, Dudley suggests that steady aerodynamics dominate for $J > 10$, while unsteady aerodynamics are present and must be accounted for when $J < 10$ [35:94]. Furthermore, hovering is arbitrarily defined to be slow forward flight such that $J < 0.1$.

The quasi-steady aerodynamics of flapping flight have been modeled primarily in two ways; the actuator disk and blade element models. The actuator disk model is a momentum-based model that seeks to account for the lift of the FWF by calculating the momentum imparted on the jet of air that is forced downward by the flapping wings [1, 35, 58, 75]. More commonly, the blade element approach is used which considers the instantaneous speed and orientation of the wing, calculates the resulting instantaneous forces based on steady-state lift coefficients and classical airfoil theory, then integrates

these instantaneous values over an entire wing stroke period to calculate the total lift force over the period. Consider the proposed wing shown in Figure 2.2 [1, 35, 58, 75].

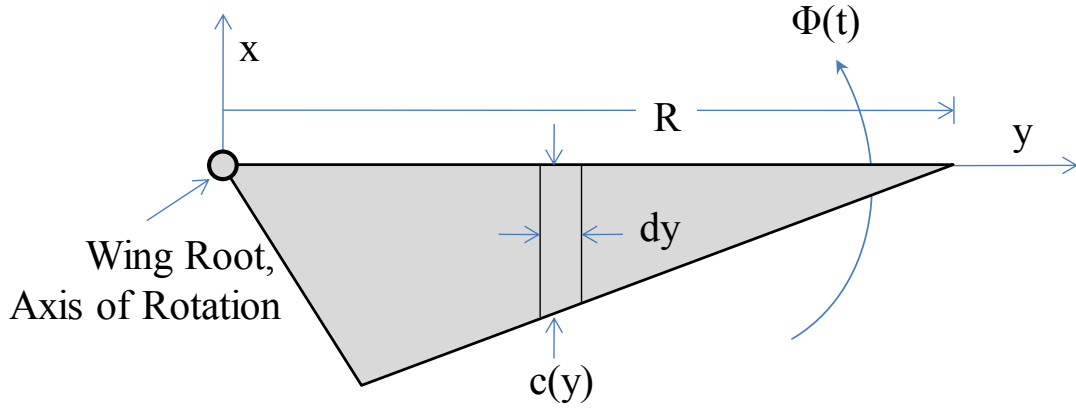


Figure 2.2. Wing geometry for blade element model.

For a given wing stroke angular velocity, $\dot{\phi}(t)$ and angle of attack $\alpha(t)$, the instantaneous differential lift produced by a differential strip of the wing (the blade element) can be calculated from the generic lift equation as:

$$L = \frac{1}{2} \rho C_L V_\infty^2 S \quad (2.2)$$

$$dL = \frac{1}{2} \rho C_L(\alpha(t)) \dot{\phi}^2(t) y^2 c(y) dy \quad (2.3)$$

where L is lift, ρ is air density, C_L is lift coefficient, S is wing area, α is angle of attack, and c and y are defined in Figure 2.2. Similarly, the instantaneous differential drag of the blade element is:

$$dD = \frac{1}{2} \rho C_D(\alpha(t)) \dot{\phi}^2(t) y^2 c(y) dy \quad (2.4)$$

Integrating over the length of the wing, the instantaneous aerodynamic forces are obtained:

$$L = \int_0^R dL = \frac{1}{2} \rho C_L(\alpha(t)) \dot{\phi}^2(t) I_A \quad (2.5)$$

$$D = \int_0^R dD = \frac{1}{2} \rho C_D(\alpha(t)) \dot{\phi}^2(t) I_A \quad (2.6)$$

where I_A is the *second moment of area* of the wing, and R is the *wing length*. Given values for $\dot{\phi}(t)$ and $\alpha(t)$ at a point in time, the quasi-steady components of the aerodynamic forces could be calculated as a function of time over the wing-beat period. Typically, however, such values are only known at discrete intervals, and a summation is used to approximate the forces. It is interesting to note that many of the values of lift and drag coefficients of insect wings that are cited in the literature are obtained by comparing the lift equation to the weight of the insect, applying the wing angular velocity and angle of attack gained from video analysis and solving for C_L and C_D [75:120]. As a result, such values should be used with caution.

In 2001 Sane and Dickinson published data of a scaled up robotic fruit fly model used to measure aerodynamic forces [71]. Because these experiments measured a large device in which the kinematics could be precisely specified, the results are likely more reliable than previous studies conducted on insects that pushed the envelope of available sensing technology and derived kinematic data from blurry video images. They

compared their measured results (which include the unsteady aerodynamic mechanisms) with predictions based on a quasi-steady blade element model for a wide range of wing kinematics. The quasi-steady model consistently gave a conservative estimate of the aerodynamic forces suggesting that the unsteady contributions tend to increase the aerodynamic forces. This suggests that if the MAV designer builds to the quasi-steady model, he can expect to be able to generate greater lift than expected, but will also experience greater drag, and thus, greater power requirements.

In 2002, Sane and Dickinson published a revised quasi-steady model that accounted for the aerodynamic forces due to rotation and added mass of the air surrounding the wing [72]. The rotational lift depends on the angular velocity of the wing rotation, and acts perpendicular to the wing, as does the added mass force. The expression for the force due to added mass is:

$$F_a = \frac{\pi}{4} \rho R^2 \bar{c}^2 \left(\frac{1}{2} \alpha \cos \alpha \right) \int_0^1 \hat{r} (\hat{c}(\hat{r}))^2 d\hat{r} - \frac{\pi}{16} \alpha \rho \bar{c}^3 R \int_0^1 (\hat{c}(\hat{r}))^2 d\hat{r} \quad (2.7)$$

where \bar{c} is the *mean chord*, \hat{r} is the *non-dimensional radial position* along the span, and $\hat{c}(\hat{r})$ is the *non-dimensional chord length* at the specified location along the span. The expression for rotational lift is:

$$F_r = \rho C_{rot} U_t \omega \bar{c}^2 R \int_0^1 \hat{r} (\hat{c}(\hat{r}))^2 d\hat{r} \quad (2.8)$$

where U_t is *wing tip velocity*, ω is *angular velocity* and C_{rot} is the *rotational force coefficient* given by:

$$C_{rot} = \pi \left(\frac{3}{4} - \hat{x}_0 \right) \quad (2.9)$$

where \hat{x}_0 is the *non-dimensional distance from the leading edge to the axis of wing rotation*. Sane and Dickinson's experiments showed that the expression for rotational force coefficient did not completely capture its variation due to angular velocity. Instead they chose a representative value for rotational force coefficient ($C_{rot} = 1.55$) for their wing model and used Eqs. 2.7 and 2.8 to augment their quasi-steady aerodynamic predictions of force production. The revised predictions model the time-varying behavior of force production much better than previous quasi-steady models had, and may be adequate as a basis for flapping wing MAV flight control design.

As stated previously, no reliable analytical models exist for predicting the force contributions resulting from the unsteady aerodynamic mechanisms. As such, they will only be discussed qualitatively here. Probably the most significant unsteady mechanism is the leading edge vortex (LEV), which results as air rolls around the leading edge at high angles of attack, primarily during the downstroke [58:235]. The low pressure vortex core creates a strong suction that enables higher angles of attack without stalling, thus creating higher than normal lift. This phenomenon is often referred to as “delayed stall” because of this feature. The leading edge vortex remains attached to the wing and functioning for three to four chord lengths before it breaks down or separates from the wing [75:124]. The strength, shape and stability of the LEV varies with Re and insect species, but a general trend is that spanwise flow in the LEV decreases as Re decreases and the LEV is more stable. The LEV has been singled out for creating short but strong

lift peaks during flapping wing experiments, prompting researchers to seek techniques for controlling the LEV and the lift peaks [35, 58,75]. At some point in the future, the LEV could play a key role in the control of MAVs by modulating the wing forces if their strength, location, and/or timing could be controlled.

The second prominent unsteady mechanism is rapid pitch up, which relies on the Kramer effect; an airfoil's ability to generate higher lift coefficients than the steady-state stall value if it is pitched up from low to high AoAs [75:132]. As they transition from downstroke to upstroke, the wings experience a quick rotation which engages the Kramer effect producing higher lift coefficients and lift peaks at the beginning of each half stroke. The precise timing and duration of this rotation can alter the lift peaks, suggesting another possible avenue for MAV control [35:129,58:236,71,72].

Wake capture, the third unsteady mechanism, occurs as an oscillating wing travels back through the wake caused by the previous wing-beat. Wake capture is difficult to predict because the location and shape of the wake depend on the past history of the wing motion. Nevertheless, experiments have shown that aerodynamic force peaks resulting from wake capture can be altered by adjusting the phase relationship between wing stroke reversal and wing rotation [35, 58, 71, 72]. Therefore, similar to rapid pitch-up, wake capture is a mechanism through which the precise control of the phase relationship between wing stroke and rotation could be used to control a MAV.

The final unsteady mechanism is the clap-and-fling, which is an interaction between the wing pairs at the top of the upstroke as they come close together, and in some cases, touch. When wings separate at the beginning of the downstroke, the peeling

apart of the wings starting at the leading edge is thought to rapidly increase circulation and thus, increase circulation. Furthermore, the clap-and-fling is thought to initialize the LEV. Not all insect species use the clap-and-fling, and those that do may only use it when carrying loads or generating high lift for rapid maneuvering, suggesting that it is a powerful lift enhancement. In fact, experiments have shown 17-25% increases in lift production resulting from the clap-and-fling mechanism [75].

The aerodynamics mechanisms that enable flapping wing flight can be categorized quasi-steady and unsteady mechanisms. The unsteady mechanisms provide the boost in aerodynamic forces necessary to make flight at the low Re of the smallest insects possible. Though we understand these unsteady mechanisms qualitatively, the current lack of quantitative data or analytic models makes them unusable as a strategy for MAV flight control at this time. However, the quasi-steady mechanisms are easily analyzed because they draw on over a century of research in steady flow aerodynamics. The resulting simple equations give a conservative estimate of the aerodynamic forces generated during flapping flight, and for lack of something better, can be used at least initially for the basis of an MAV flight control design.

2.2 Biological Flight Stability and Control

Characterizing the passive stability of insects is difficult because one cannot simply “turn off” the active control system to make measurements. Nevertheless, a number of system models have been obtained through experimentation, analysis or a combination of both from which stability properties can be derived [83, 86, 87, 88]. One technique for modeling an insect is tethering it to a force balance in a wind tunnel which

is similar to an open-loop condition, in that input forces and moments are prevented from acting on the free body. However, in this case the control system is still active, and one would expect accumulating steady-state error to saturate the control inputs over time, altering the system inputs. Nevertheless, reasonable estimates of the stability derivatives of some insects have been obtained in this way [88]. Alternatively, stability derivatives have been obtained through CFD simulation which has the benefit of being truly “open loop”, but offers less realism than insect experiments [83].

To date, the stability analyses performed on insects have focused on the longitudinal stability of bumblebees and locusts, producing linearized equations of motion based on small perturbations. The locust system model had stable modes similar to the phugoid and short period modes in aircraft and an unstable divergence mode in which an increase in pitch is accompanied by a decrease in forward velocity. This would cause the insect to stall out following a nose up disturbance, or nose dive following a nose down disturbance. Fortunately, this mode is slow to develop with a half life on the order of three wing-beat cycles, so it should be easily controlled by the insect [88]. The bumblebee model had two stable modes and one unstable oscillatory mode in which pitch oscillations accompany oscillations in forward velocity, similar to the behavior of the locust [83]. Error analysis that statistically varied the stability derivatives showed that even allowing for large errors in the experiments, the open loop roots of the insect were qualitatively correct. Furthermore, direct observations of insect flights confirm the flight handling predicted by these stability analyses [87].

In all cases presented in the literature, the flapping frequency was at least several times greater than the fastest dynamic mode (i.e. phugoid, short period, etc.) of the insect. This is a prerequisite for using a so-called “quasi-static” assumption that only the cycle-averaged forces and moments, and not the inter-cycle forces and moments are important in determining the dynamics of a FWF. In helicopters, such an assumption has been shown to be valid if the rotor frequency is an order of magnitude higher than the frequency of the fastest mode [88]. Such an assumption greatly simplifies the dynamic analysis and control system design. On the other hand, flapping at such a high frequency limits the ability of inter-cycle force adjustments to influence the dynamics of the vehicle as inputs at a higher frequency than the natural frequency are usually greatly attenuated. This would reduce the responsiveness of a vehicle, and possibly limit its maneuverability. Experiments on free flying insects seem to validate the quasi-static assumption in that seemingly “quick” maneuvers required several wing-beat periods to execute [38, 89], and these observations are supported by at least one simulation [66].

The examination of insect flight stability has several important implications for the MAV designer. The unstable mode observed in all experiments can be easily controlled if adequate pitch-rate damping is included in the system. This can be achieved by ensuring that the cycle-averaged or quasi-static aerodynamic force acts behind and/or above the center of mass (COM) [35:228, 87:363]. This will ensure that the pitching derivative, $\frac{\partial M}{\partial \alpha}$ is negative, providing a nose down torque to stabilize the divergent pitch mode. Furthermore, flapping flight is not intrinsically less stable than gliding or fixed wing flight, but the flapping motion could amplify any existing instability. A quasi-

steady blade element analysis revealed that if the wing stroke is purely planar, then the vehicle will have neutral pitch stability in hover (a condition also observed in helicopters) [87]. This situation can be improved by flapping above the stroke plane near the end of each half stroke, creating a convex-down conical wing tip trajectory similar to dihedral in a fixed wing aircraft, increasing roll, pitch and yaw stability in hover [35:228, 87:362]. Any flapping wing MAV should employ this design at least until flapping wing control evolves to a point where it can actively stabilize these DOF.

Very little is definitively known about active insect flight control, but numerous researchers have performed experiments that give insight to the MAV control system designer. Insects have a broad host of sensors that are integrated to provide a surprisingly detailed picture of its flight condition. Primary among them is the compound eye, which accounts for as much as 80% of brain function in some insects and uses the horizon and optic flow to sense pitch and roll attitude and rates as well as velocity. Experiments have shown that when the visual field surrounding an insect is rotated, the insect produces a restoring torque in an attempt to halt the rotation [23, 35:206]. Similar experiments showed a correlation between translational optic flow and wing-beat frequency, suggesting insects use flapping frequency to control airspeed [35:208]. Despite the apparent importance of vision in insect flight, experiments in which blinded houseflies were able to fly freely indicate that vision is not a necessary condition for flight, and further underscore our lack of understanding of insect flight control [35:212].

Relative airspeed is sensed by a number of hairs, and antennae. This information can be used to measure airspeed, angle of attack, and sideslip [35, 86]. Actively

controlled oscillation of the antennae has been suggested as a means for regulating wing flapping frequency in some species [35:214]. Wing-beat frequency has also been shown to be regulated by *campaniform sensillae*, dome-shaped mechanoreceptors that sense elastic deformation of the wing [35:215]. Perhaps the most unique and intriguing flight sensor is the gyroscopic haltere in *Diptera*. The halteres are small appendages, apparently evolved from the hindwing, that oscillate in flight at the same frequency as the forewings and measure accelerations through fields of campaniform sensillae at their base [35:217]. Halteres are thought to improve the maneuverability of *Diptera*, though numerous other sufficiently agile taxa get by without them.

Experiments on the pathways between these sensors and the flight muscles themselves suggest that insects have a dispersed control system consisting of multiple feedback loops with numerous redundancies that are capable of maintaining flight even when multiple senses are denied. Some sensor feedback, such as the campaniform sensillae that measure wing deformation, bypass the central nervous system and influence the flight control muscles directly [35:215]. Conversely, optical information is comprehensively passed through the central nervous system before control inputs are fed to the flight muscles [35:205]. This dispersion of control authority suggests the existence of a control hierarchy with inner feedback loops that precisely regulate the wing kinematics, intermediate loops that regulate body attitude and motion by prescribing the wing kinematics, while an outer navigation loop prescribes the desired body attitude. A hierarchical system such as this would simplify the design of MAV control by breaking the problem into more manageable pieces.

The intermediate control loop; that of regulating body attitude by prescribing wing kinematics, is currently the most challenging piece of the MAV control problem. The other two loops have been solved, to some degree, in other fields, but the link between wing kinematics, aerodynamic forces, and ultimately, body attitude is a mystery. No comprehensive theory exists to explain how insects perform this complex operation, but some experiments have resulted in useful discoveries [13, 35, 38, 88, 90]. Insect bodies and legs have a role in flight control, but are not generally considered to be primary actors [35:232]. One study noted that locusts used the abdomen and hind legs for control only during slow flight [86], while another suggested that the abdomens of butterflies are very active in flight control [17, 18].

Forward flight speed would logically seem to be correlated to flapping frequency, but consistent evidence of this in insects is lacking. Flapping frequency tends to be largely invariant in all species, so is not likely used as a control input unless used as small excursions from the mean in short bursts for acceleration [35:101]. Instead, airspeed seems to be controlled by minute changes in the wing kinematics that create nose-down pitching moments, an increased stroke plane angle and a resultant forward shift in the net aerodynamic force. Stroke amplitude has been studied closely in several species, and was not shown to be related to airspeed, but it is correlated with aerodynamic force production, so it could be used for acceleration if the force vector were rotated [75, 85]. Bumblebees and hawkmoths have been observed to increase their mean stroke angle when accelerating [90]. Increased wing rotation speeds and stroke plane deviations have also been linked to acceleration in bumblebees [35]. In fast forward flight, insects are

observed to have a nearly horizontal body angle (aligned with the velocity vector) and a near vertical stroke plane. For vertical accelerations, very little is published, but the prime mechanism for the increase in lift necessary to climb is likely an increase in stroke amplitude. During heavy lifting exercises, some insects have been observed to increase their stroke amplitude sometimes to the point where the clap-and-fling mechanism is engaged, giving an additional boost in lift, and this is likely used for climbing as well [75:137].

Rotations about the primary axes have been definitively linked to asymmetries in wing kinematics through tethered insect experiments [35:229]. Deviations in stroke amplitude, stroke plane angle, angle of attack, speed and timing of wing rotation, and interactions between fore and hindwings have all been identified as contributing to body torques. For example, a saccade is a 90° yaw maneuver which has been linked to a slight decrease in stroke plane angle and increase in stroke amplitude on the outside wing [38]. This change in kinematics increases the AoA on the outside wing at the beginning of the upstroke which increases the aerodynamic force (which is momentarily horizontal) at that instant, creating a torque about the vertical (yaw) axis. Very slight changes in the kinematics were needed to perform the saccade in only 50 ms.

Roll maneuvers in tethered locusts can be initiated by timing and magnitude of changes in elevation angle and stroke amplitude [35:231]. It seems unlikely that a single kinematic parameter or muscle is responsible for a single maneuver, but rather, complex interactions between numerous variables give an insect a wide range of possible means by which to maneuver [13]. The experiments by Sane and Dickinson [71] referenced

above demonstrated that slight variations in wing kinematics such as the duration of wing rotation and its timing relative to stroke reversal produce larger variations in cycle-averaged aerodynamic forces. These experiments, coupled with observations of insects make it clear that any number of kinematic control strategies could be successfully used to control a MAV.

Due to our meager understanding of insect flight control, it seems prudent to avoid an attempt at mimicking their techniques. Furthermore, the means of flight control used by insects are, to a large extent, irrelevant at this time, as no flight-worthy mechanism has yet been built that could mimic the complex kinematics exhibited by insects. Instead, it would be wise to consider how a MAV could be controlled through the DOF available to current wing flapping mechanisms while the entomologists refine our understanding of insect flight control.

2.3 Design Considerations for Flapping Wing Micro Air Vehicles

Considering the vast phylogenic and morphologic diversity of insects, it is clear that a vast number of flapping wing MAV designs are possible. It follows then, that a number of strategies for controlling them would also be successful. The control strategy of a given flapping wing MAV is strongly constrained by its physical design, and therefore, a discussion of flapping wing MAV control cannot proceed without a discussion of the complex tradeoffs facing the MAV designer. The key design features for flapping wing MAVs are vehicle size and flight regime, number of active DOF of the wings, and the wing actuator type. As with most difficult problems, these features are all strongly coupled.

Allometries

The relationships between mass, length, power and flapping frequency of birds, bats and insects have been well-documented in the literature [1, 12, 35, 45, 55, 58, 75]. These allometries result from the cubic relationship between length and volume, and subsequently mass. In steady level flight, the weight of a flyer must be balanced by the lift which is related to the wing area. Considering this, we would expect the weight of a flyer to be proportional to the cube of its representative length. For birds and airplanes this relationship has been shown to be [75:17]:

$$l_{Bird} = 1.704 m_{Bird}^{1/3} \quad (2.10)$$

$$l_{A/C} = 1.654 m_{A/C}^{1/3} \quad (2.11)$$

In insects, the relationship is not as clearly defined, but it can be derived. In insects, the relationship between wing area and mass is shown to be approximated by [35:88]:

$$S_{Insect} \propto m_{Insect}^{0.71} \quad (2.12)$$

Further study of the data in [35] reveals that an adequate constant of proportionality is 15.

The wing area is related to wing span by the relation:

$$l = \sqrt{S \cdot AR} \quad (2.13)$$

where AR is aspect ratio, which ranges from 2 to 10 in insects [35:56]. Synthesizing these relationships and choosing $AR = 2.5$, Eq. 2.12 can be rewritten as:

$$l_{Insect} = 1.58 m_{Insect}^{0.355} \quad (2.14)$$

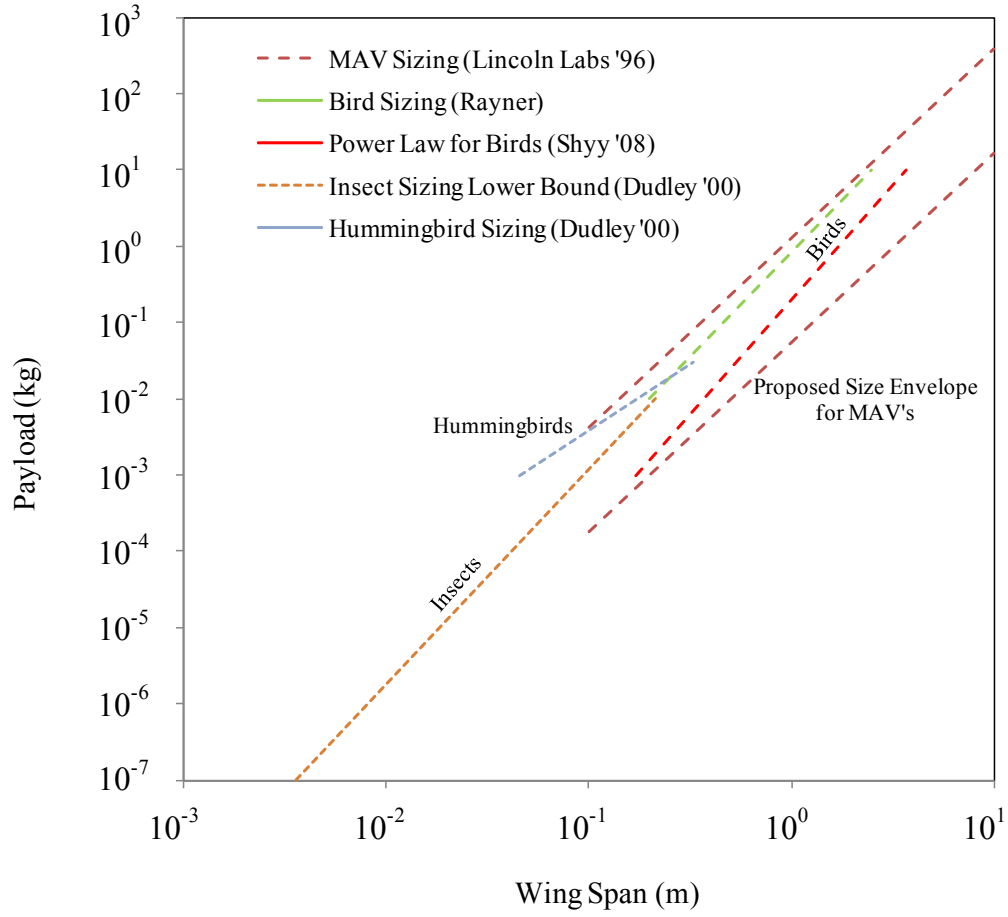


Figure 2.3: Flying animal allometry and MAV sizing, data from [21, 55, 56, 75].

which matches the relationships for birds and airplanes quite well. Figure 2.3 depicts these relationships, and includes a proposed size regime for MAVs from one of the earliest documents to propose them [21].

In addition to sizing, wing-beat frequency follows allometric laws, though there is greater variation across species. This relation is [35:89]:

$$f \propto m^{(-0.18 \text{ to } -0.29)} \propto l^{(-.51 \text{ to } -.82)} \quad (2.15)$$

Shyy et al., make two arguments for the relationship between mass and flapping frequency. The first notes that a given muscle mass can produce a limited force, which limits the angular acceleration possible, and thus the flapping frequency. This argument gives a theoretical upper bound of flapping frequency in animals as [75:20]:

$$f_{\max} \propto m^{-1/3} \propto l^{-1} \quad (2.16)$$

Meanwhile the minimum flapping frequency is determined by the induced velocity required to maintain sufficient lift, thus the theoretical lower bound is [75:20]:

$$f_{\min} \propto m^{-1/6} \propto l^{-1/2} \quad (2.17)$$

which agrees well with the range of values apparent in insect species.

Besides being interesting, these allometries have important implications for MAV design. As the desired MAV size is reduced, the mass of the payload and components must be reduced by a power of 1/3, and the flapping frequency must increase. The choice of wing flapping powerplant is probably most affected by this law. As MAV size is reduced, the flapping actuator(s) is required to be much smaller while also operating at a higher frequency; this requirement drastically limits the choice of actuators.

Powerplants

Wing flapping actuators currently fall into two major categories, rotary and linear. Rotary actuators used in MAV prototypes to date include DC electric motors [19, 20, 39, 44, 47, 49, 51] and internal combustion engines [101]. DC electric motors have thus far been the most popular choice of the MAV designer with several successful prototypes flying under their power. These vehicles are all larger than insect size probably because

larger vehicles are easier to build and larger components are more readily available off the shelf. MAVs driven by electric motor typically require a gear reduction, as motors in this size range typically operate in the range of 15,000 rpm, or 250 Hz [61]. A crank rocker mechanism is then used to transform the rotary motion into an oscillatory flapping motion. While electric motors have proven to be a successful design choice, they unfortunately have a lower size limit which translates to a lower bound of motor actuated MAV size. In insects, the flight muscles make up between 20 – 50% of the total mass depending on the species [35:245], while previous MAV designers have suggested the flight actuator should be approximately 15% of the vehicle weight [47]. Given that the smallest commercially available DC motors weigh in the range of 200 mg [61], the smallest MAV possible would be approximately 1 gram, which according to the relationship in Eq. 2.14 would correspond to a maximum vehicle dimension of 14 cm, or about the size of the largest butterflies and moths. In addition, the efficiency of electric motors is known to decrease as they are miniaturized while friction in the gearbox will become more significant, further limiting the extent to which motor driven MAVs can be miniaturized [59:83].

Numerous linear actuators have been proposed that avoid these size limitations including piezo ceramic materials (PZT), shape memory alloys (SMA), piezo polymers (PVDF), solenoids, dielectric elastomers (or electroactive polymers - EAP) and reciprocating chemical muscles (RCM). Two insect-sized MAV prototypes have successfully demonstrated the feasibility of linear actuators [16, 93], while the RCM has flown in a bird-sized MAV [57]. MAV's driven by linear actuators require a

transmission that converts the linear oscillation to a flapping motion. Researchers at UC Berkeley were the first to accomplish this with their Micromechanical Flying Insect (MFI) [10, 11, 79, 80, 81]. They used a slider-crank to link the arc motion of the tip of a bimorph cantilever PZT actuator to the arc motion of the four-bar linkage that drives the MFI's wings. This work has been continued and refined by Wood, et al. at Harvard using a similar transmission [93]. An alternate design created by researchers at Delft University in the Netherlands uses a solenoid mounted within a stiff ring-like structure [16]. The solenoid excites the first mode of the ring which then actuates four wings placed equidistantly around the ring. The design is currently limited by the low power density of the solenoid (though an axial PZT could be used in its place) and the resonant actuation of all four wings by one actuator limits the possibilities for control.

A suitable linear actuator for an insect-sized MAV must have the following characteristics; high power density, large displacement (strain), high force output (stress), high bandwidth, high efficiency and durability. Furthermore, all of these characteristics must be available in a device weighing less than 200 mg and less than 1 cm in size. An initial attempt to compare the candidate actuators was given by Conn, et al., but the actuators were compared to human skeletal muscle, which is of limited value [19]. Table 2.1 compares these actuators to insect flight muscle which is more appropriate. Figure 2.4 gives a direct comparison of these actuators to asynchronous insect flight muscle. Note that the data used for these comparisons (taken from [15]) are from many

Table 2.1. Linear Actuator Characteristics

Actuator Type	Strain (%)	Stress (MPa)	Frequency (Hz)	Specific Energy Density (J/g)	Efficiency (%)
Synchronous Flight Muscle	17 ^a	0.35 ^c	5.5 - 100 ^d	0.003 ^f	2-13% ^h
Asynchronous Flight Muscle	2 ^b	-	100 - 1046 ^e	0.002 ^g	5-29% ⁱ
PZT ^j	0.2	110	10 ⁸	0.013	90
PVDF ^j	0.1	4.8	10 ⁷	0.0013	90 ^k
SMA (TiNi) ^j	5	200	10 ¹	15	10
Solenoid ^j	50	0.1	10 ²	0.003	90
EAP (Dielectric Elastomer) ^j	63	3	10 ⁴	0.75	90

^a Monarch butterflies [35:176]

^b Bumblebees [35:176]

^c Locust from Alexander, pp. 19

^d [35:87]

^e [35:88]

^f Hawkmoth [35:191]. Note, energy density = (power density)/(flapping frequency)

^g Bumblebee [35:191]. Note, energy density = (power density)/(flapping frequency)

^h [35:193]

ⁱ [35:193]

^j [15:533]

^k[19]

different sources using different test methods. Therefore, the figure should be considered as only a general comparison. An initial look at the data suggests that the EAP actuators are far superior to all other options, being superior to insect flight muscle in all categories. Unfortunately, EAP's require large voltages (over 1000V) and the power electronics required to generate this from a 5V battery are large and heavy.

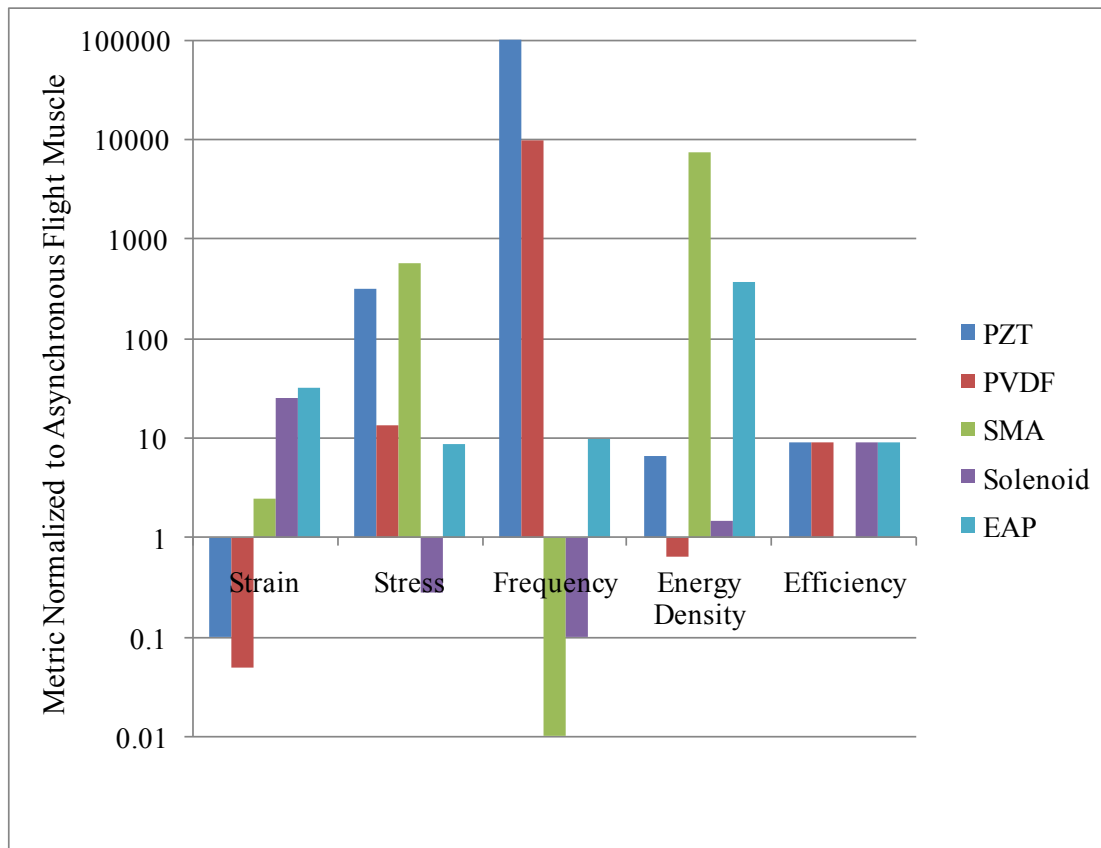


Figure 2.4. Comparison of linear actuators to insect flight muscle.

SMA and solenoids are hampered by their low bandwidth, and simply cannot operate fast enough to drive an insect-sized MAV. The PVDF is the only actuator with inferior energy density to flight muscle. Considering the critical role of mass in a flapping wing MAV and the very small margins for efficiency, it seems unlikely that an actuator that is less mass-efficient than insect flight muscle could result in a successful design. Finally, PZT is superior to insect flight muscle in all categories except strain. This can be overcome with the bimorph cantilever design that generates an order of magnitude

greater displacements. Similar to EAPs, however, PZTs also require large voltages (around 100V) and the accompanying power electronics.

Considering the important role of power electronics, actuators should be compared in conjunction with their required power electronics. Such an analysis was accomplished by Karpelson, et al., for use on sub-gram sized flapping wing MAVs [46]. They analyzed five general classes of actuators as well as various embodiments of those actuator types. These actuator types include electrostatic (comb drives and parallel plates), thermal (axial and bimetallic cantilevers), piezoelectric (bimorph and unimorph cantilevers), SMA (axial and bimetallic cantilevers), and dielectric elastomers. Using simplified constitutive equations for these various technologies, operating envelopes and performance estimates were created and compared. Again, thermal and SMA actuators were determined to be too slow for most flapping MAV applications, though they noted that these actuators should scale favorably as reduction in size will yield faster cooling and higher bandwidth. While SMAs are not currently applicable, as MAVs are further miniaturized, they may be an attractive option given their high power density and low voltage requirements. Electrostatic actuators were found to be incapable of producing sufficient work for their weight, and are thus unsuitable for FWMAV applications. This leaves PZT and EAP (dielectric elastomers) as the final candidates which both require voltage amplifying power electronics.

Three different types of voltage amplifying circuits were considered, with two of these being built and tested [46]. The voltage amplification required for PZT actuators is in the range of 20-40x, which can be accomplished at this scale in a flight-worthy

package. The EAP actuators require amplification of 200-400x. Given the current state of technology, such an amplification circuit would exceed the weight and size budget for an MAV of this size. Accounting for the weight of the vehicle's structure, actuator and power electronics, sensors and controller, and battery, Karpelson, et al., estimated the endurance of several candidate MAV designs based on a blade element analysis of lift and power requirements. They calculated that a PZT powered, 1g MAV would have an endurance of between 4 and 10 minutes. This far exceeded the estimated performance of MAVs powered by other actuator types. Given these considerations, it is clear that piezoelectric bimorph cantilevers are the superior choice for insect-sized MAVs.

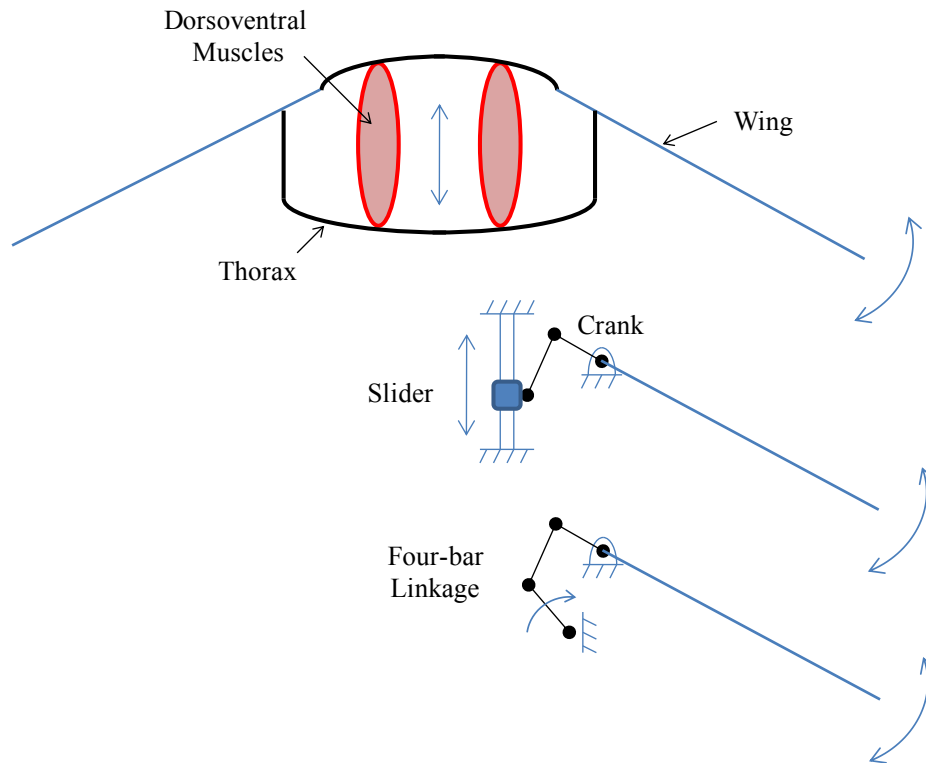


Figure 2.5. Insect flapping mechanism and its mechanical analogies

Mechanism Design

Flapping wing mechanism design is a complex problem. An entire dissertation could focus just on this area, and many have. Therefore, only a brief review will be accomplished here, constraining the topic to mechanism designs suitable for insect-sized MAVs and how they relate to flight control. A simplified model of the insect flight apparatus is given in Figure 2.5. The mechanism can be likened to a simple crank-slider linkage. This, in turn, can be simplified by replacing the slider with a fourth link to create a simple four-bar mechanism; most rotary actuator driven MAVs use a variation on this latter arrangement [19, 20, 39, 41, 51].

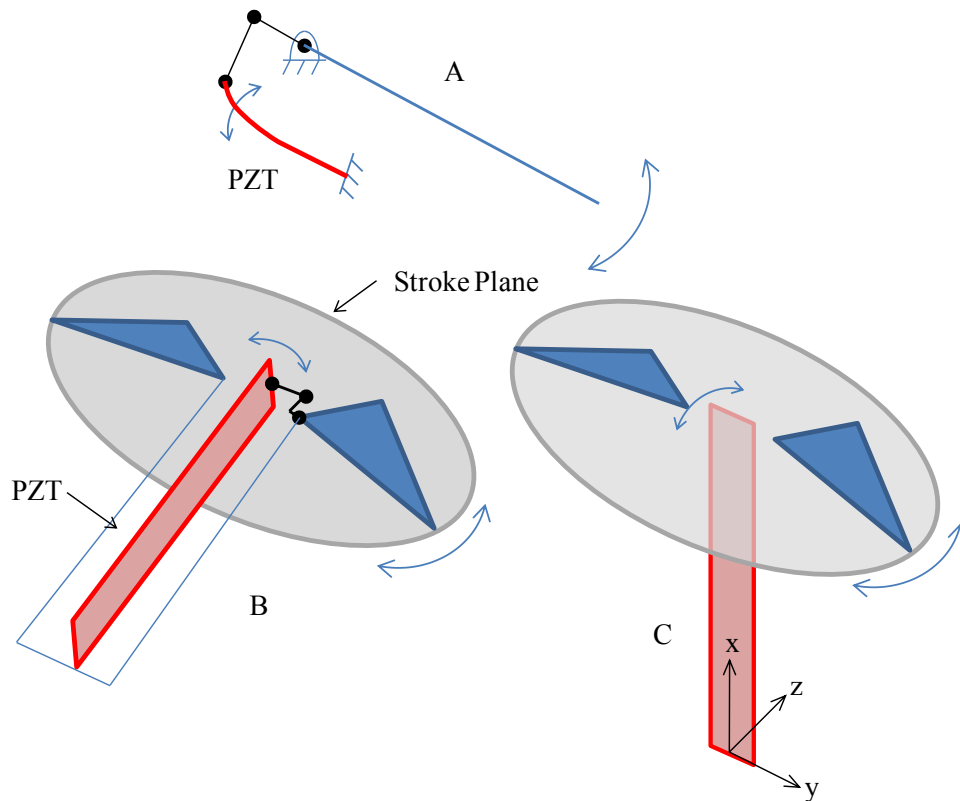


Figure 2.6. Flapping mechanism for PZT bimorph cantilever actuator

A PZT bimorph cantilever actuator, though categorized above as a “linear” actuator, actually moves in an arc. Therefore, it could replace the driving link in the four-bar linkage design as shown in Figure 2.6A. However, this arrangement places the actuator motion in the wing stroke plane, as is clear in the figure. As noted above, PZT actuators have limited strain ability, so to maximize the deflection of the actuator, the cantilever should be made as large as possible (for example, the UC Berkeley MFI and Harvard Robofly actuators are comparable in length to the wing length [79, 93]). Placing such large actuators in the wing stroke plane would be undesirable because it would raise the center of mass of the vehicle, reducing stability as shown in Figure 2.6B. Such an arrangement is also not seen in insects. Instead, the actuators should be placed along the longitudinal axis of the fuselage, and thus, perpendicular to the wing stroke plane as shown in Figure 2.6C. This rotation of the actuator precludes the use of the simple four-bar linkage.

The UC Berkeley and Harvard designs instead use a double crank-slider mechanism (Figure 2.7). The first crank-slider transforms the arc motion of the PZT tip (crank) in the x-z plane (refer to Figure 2.6) into a linear motion parallel to the z-axis. This linear motion is then transformed into rotary flapping motion in the y-z wing stroke plane through the shared slider and second crank. Because of the importance of friction as mechanisms scale down, flexures are used for the rotary joints. The apparently superfluous links in the figure are required to keep the flexures aligned in a neutral position when the vehicle is at rest. The flexures also can be designed to improve the

frequency response of the mechanism and tune it for the desired performance [10]. The length of the second crank determines the transmission ratio of the mechanism:

$$T = \frac{\phi}{\Delta} \approx \frac{1}{L} \quad (2.18)$$

where Δ is the linear displacement of the slider and L is the length of the second crank.

For the greatest wing motion, the crank length should be made as small as possible. The lengths of the other links are not critical to the wing motion, but they must be chosen carefully to avoid singularities in the mechanism and ensure the flexures are not over rotated.

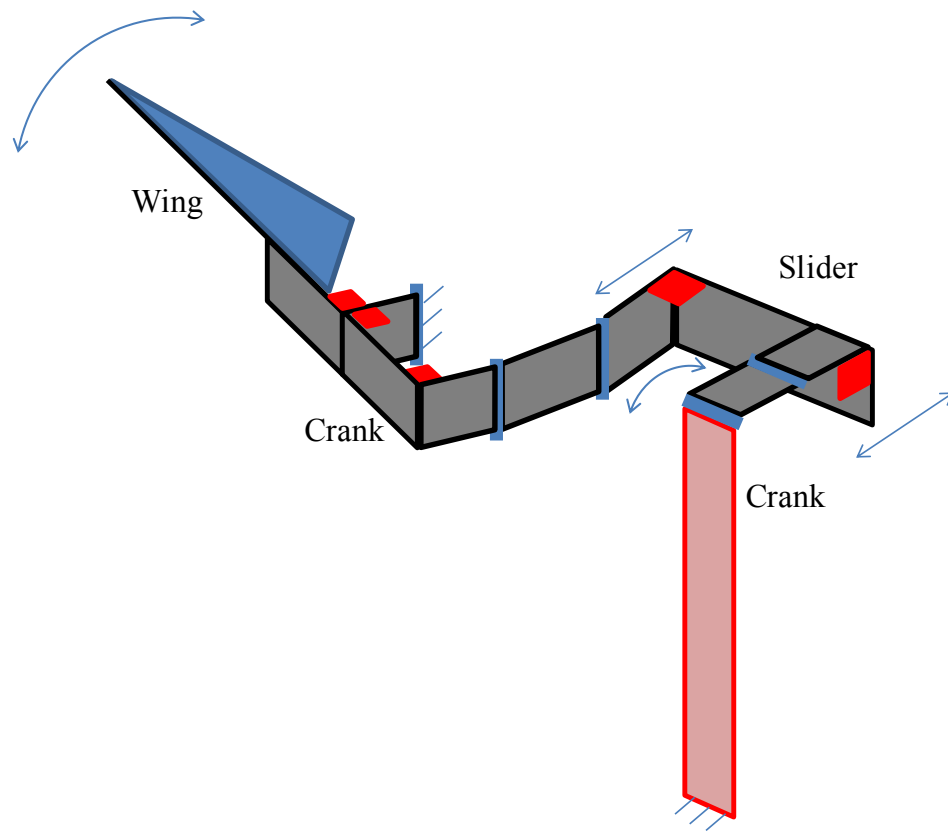


Figure 2.7. Double crank-slider mechanism of the Harvard Robofly [92]. Rotary joints are shown in blue, fixed right angle joints are shown in red.

In addition to actuator type, the number of actuators to include strongly influences the mechanism and control design. Increasing the number of actuators increases the mechanism complexity and vehicle weight and power requirements, while also giving more control options. Wing flapping mechanisms have been proposed with as many as 3 input actuators and as few as one [19]. How the actuators operate further influence the controllability they will provide. For example, rotary actuators driving a crank-rocker mechanism will have a fixed amplitude defined by the linkage geometry. For rotary

actuators in general, only the speed can be varied. This property can be used to alter wing velocity and phase relationships between other drive actuators (such as the phase between wing stroke and rotation). In contrast, mechanisms employing linear actuators could vary the actuation speed and amplitude, and will generally be less constrained by actuator inertia than an electric motor. The ability to alter two characteristics of one actuator could preclude the need for multiple actuators on one wing, provided an adequate control strategy is implemented. Given the strong coupling between number and type of actuator and control system design, this discussion will be continued in the following section on flight control concepts.

Significance of Flapping at Resonance

It is frequently proposed that insects flap their wings in such a manner as to excite the first natural frequency of the wing flapping apparatus. The thoracic cuticle, flight muscles and wings have all been implicated by biologists as providing the necessary elasticity for resonant flapping, though resonance of the thorax would be most critical, as its deformations are amplified by the crank-slider mechanism described above to generate larger wing deformations. Perhaps the strongest evidence for resonant wing flapping is the surprising consistency of a given species' wingbeat frequency across all flight regimes [35:49]. Studies performed on beetles determined that temperature induced variations in wing beat frequency could be accounted for in temperature-related changes to the elastic properties of the flapping apparatus [35:90]. Furthermore, wing amputation experiments have shown that wing beat frequency is related to wing inertia in a manner that suggests mechanical resonance [35:89]. Based on such experimental evidence as

well as theoretical predictions of power requirements based on blade element analyses, biologists appear uniformly convinced that insects flap their wings at “resonance”. To be more precise, insects apparently flap their wings at the resonant frequency of the muscle-thorax-wing-air system, which is likely not the 1st bending mode of the wing itself, but a combination of the contributed mass and stiffness of all the components of the system. Likewise, all further mention of the resonance of a mechanical flapper should be taken as the resonant frequency of the actuator-transmission-wing-air system.

The significance of resonant flapping is of critical importance to the control systems designer [32]. If there is an energy benefit to resonant flapping, then vehicle performance requirements such as range, endurance, speed, and payload will demand that it be used. However, flapping at resonance will make it extremely difficult, if not impossible, to drive the wings in any pattern other than simple harmonic motion. As will be shown, several promising control strategies depend on being able to do just that. Therefore, from the control perspective, it would be preferred to avoid flapping at resonance. However, if there is indeed an energy benefit to flapping at resonance, techniques for non-harmonic resonant flapping should be developed, if possible, as are presented here.

From an engineering standpoint, the importance of resonance is essentially a question of damping [56]. A lightly damped structure will oscillate when excited, and the less damping, the longer it will oscillate. Given enough damping, the structure will not oscillate, and the structure is said to be “critically damped”. In this case, kinetic energy from one wing beat is not passed to the next wing beat, and there is no energy benefit.

The damping in any flight system consists of viscoelastic damping in the structure and aerodynamic drag on the wing. The latter is likely most significant as it corresponds to the aerodynamic forces that enable flight. There can thus be no doubt that these forces are significant. Analytically predicting the significance of damping is not possible with linear techniques because the aerodynamic damping is not linear, but quadratic, and the numerous previously discussed unsteady aerodynamic mechanisms cannot be modeled analytically. Nevertheless, this question could be definitively answered given a prototype wing flapping mechanism and a means for measuring high amplitude wing displacement. Given these, a frequency response function could be measured from which the potential benefit of resonant flapping could be quantified from the relative height of any resonant peaks.

Experiments such as these were performed on the Berkeley MFI [10, 11]. FRF's of the wing flapping system were created by measuring the actuator motion with strain gauge sensors and optical position sensors while flapping the wing at high amplitudes ($\pm 60^\circ$ to $\pm 120^\circ$). In one case, a 1DOF fly-sized MAV wing had a quality factor¹ of 2.21 indicating that the system was under-damped, so it would indeed benefit from flapping at resonance, though a large range of frequencies would benefit from resonant behavior. These papers further reported that the wing flapping mechanism could be tuned to have differing frequency responses by changing the flexure stiffnesses and other material properties and geometries. A subsequent paper by the same group reported that their

¹ Quality factor is a dimensionless parameter indicating system damping, defined as: $Q = \frac{\omega_n}{\Delta\omega}$ where ω_n is the resonant frequency and $\Delta\omega$ is the bandwidth. The higher “Q”, the lower the damping.

mechanism was designed specifically to have a “low” quality factor of 3 or less to improve the controllability of the wing trajectory [23]. This suggests that a mechanism with even higher quality factor might be possible, if desired.

2.4 Concepts for the Control of Micro Air Vehicles

Early in the development of flapping wing MAVs the challenges of aerodynamics and microfabrication were so daunting that the issue of control was put aside. Significant progress in those areas has elevated the flapping wing control problem to the point of being the last major barrier to autonomous flapping wing MAVs, and the top priority for the MAV designer [92,93]. This problem has been probed with analysis and some simulation [23, 24, 26, 27-31, 42, 50, 60, 63, 65], but to date, hardware-in-the-loop simulations have been rare [36, 37, 93], and full-up system demonstrations nonexistent.

As noted in the previous section, there are likely a number of possible flapping wing MAV designs, and each will need its own unique control strategy. Therefore, a discussion of control strategies must be conducted in the context of the specific MAV design in question. The primary characteristic constraining control is the number of DOF inherent in the wing flapper mechanism. Secondary concerns are the range of each of those DOF, their bandwidth, and supplemental control surfaces which will directly affect the controllability of the vehicle and drive the control strategy. To date, discussions of flapping wing MAV control in the literature can be grouped into two major camps based on the number of DOF actively controlled by the wing flapper mechanism; multi-DOF control and single-DOF control. Wing stroke angle is a necessary condition for flapping wing flight, so all proposed control strategies in the literature have at least that DOF.

More complex schemes include wing rotation as a second DOF and wing elevation angle is usually the last to be included.

The rigid body equations of motion of a MAV can easily be derived from first principles, and they are presented here in the body frame of the MAV which will be most convenient for translating aerodynamic forces and moments (which will be calculated in the body frame) to motions of the body:

$$I \begin{bmatrix} \dot{p} \\ \dot{q} \\ \dot{r} \end{bmatrix} = \begin{bmatrix} L \\ M \\ N \end{bmatrix} - \begin{bmatrix} p \\ q \\ r \end{bmatrix} \times I \begin{bmatrix} p \\ q \\ r \end{bmatrix} \quad (2.19)$$

$$\begin{bmatrix} \dot{u} \\ \dot{v} \\ \dot{w} \end{bmatrix} = \begin{bmatrix} qw - rv \\ ru - pw \\ pv - qu \end{bmatrix} + \left(\frac{1}{m} \right) \begin{bmatrix} X \\ Y \\ Z \end{bmatrix} - R_I^B \begin{bmatrix} 0 \\ 0 \\ -g \end{bmatrix} \quad (2.20)$$

where I is the inertia matrix, $[p \ q \ r]^T$ are roll, pitch and yaw angular rates,

$[L \ M \ N]^T$ are the roll, pitch and yaw moments, $[u \ v \ w]^T$ are the translational

velocities, m is the mass, $[X \ Y \ Z]^T$ are the axial forces, R_I^B is a rotation matrix from

the inertial frame to the body frame, and g is gravitational acceleration [82]. Though

notational variations exist, these equations of motion are commonly used throughout the

literature [23, 26, 29, 50, 100]. The notation used here is common in the aircraft control

field.

Given the rigid body equations of motion, the challenge of predicting the dynamics of a MAV comes in predicting the forces and moments, $[X \ Y \ Z]^T$ and

$[L \ M \ N]^T$, or “wrench”, that result from given wing kinematics. Though there is some variation in how they are derived, all analyses present in the literature estimate the wrench with some sort of quasi-steady aerodynamics equations [23, 24, 26-31, 42, 50, 63, 65]. This fact ensures that all of these analyses are common in that they ignore the unsteady aerodynamics, which can be significant.

The simplest formulation uses translational blade element analysis to compute the instantaneous forces on the wing, then integrates over the wing-beat period to obtain cycle-averaged forces. The cycle-averaged moments are obtained by multiplying the instantaneous forces by the moment arm created by the offset between the COM and the center of pressure of the wing (which is considered fixed on the wing) and integrating over the wing-beat to obtain cycle-averaged moments [28]. The most elaborate quasi-steady formulation includes translational and rotational blade element forces as well as body drag forces to compute cycle-averaged forces as proposed by Sane and Dickinson’s revised quasi-steady model [72]. The moments are also calculated in a blade-element fashion by considering the elemental moment created by an elemental force and the moment arm between the elemental center of pressure and the COM [26]. This latter formulation accounts for change in the center of pressure as a function of angle of attack and yields time-accurate (within the limits of the quasi-steady model) aerodynamic moments. The simulation in question needed instantaneous rather than cycle-averaged forces and moments because it did not use the quasi-static assumption of flapping flight dynamics. The contents of the blade element equations can vary significantly depending on the DOF of the wing flapping mechanism.

Control Concepts Based on Multi-Degree of Freedom Wing Kinematics

The greatest control authority can be obtained by including the greatest number of DOF in the wing kinematics. The earliest attempt to design flapping flight control was performed by the Micromechanical Flying Insect group at the University of California, Berkeley and published by Deng, et al. [23, 24]. They presented a thorough hierarchical control system design including a navigation planner with sensor feedback, a flight mode stabilizer, and a wing trajectory controller. There is no evidence in the literature that they tested their design on hardware, rather, they only ran simulations, presumably because the sensors and control hardware could not be sufficiently miniaturized. The early versions of the MFI allowed for independent control of two DOF per wing; stroke angle and rotation, which were utilized in their control strategy.

Deng, et al. used a quasi-steady aerodynamic model that draws heavily from the work of Sane and Dickinson [72] including translational forces (identical to Eqs. 2.3 and 2.4) as well as an adjustment to account for rotational lift (identical to Eq. 2.8). Their model of the rigid body dynamics is identical to that presented above in Eqs. 2.19 and 2.20. They presented an impressive array of sensor designs including ocelli-like pitch and roll sensors, a magnetic compass for yaw, halteres for angular accelerations and optic flow sensors for navigation and obstacle avoidance [23]. By citing averaging control theory, they make an argument for the quasi-static assumption to avoid the time-varying dynamics problem. A condition of this argument is that the control inputs be T-periodic functions, where T is the wing-beat period, and inputs cannot be altered within a wing-beat, but only at the start of each wing-beat (a zero-order hold condition).

For the wing kinematic inputs, Deng, et al. propose nominal, harmonic stroke angle and wing rotation functions that can be adjusted away from the nominal position for control purposes. Specifically, these time-varying periodic functions are:

$$\begin{bmatrix} \phi(v, t) \\ \psi(v, t) \end{bmatrix} = \begin{bmatrix} g_\phi(t) \\ g_\psi(t) \end{bmatrix} + \begin{bmatrix} v_1 g_1(t) \\ v_2 g_2(t) \end{bmatrix} \quad (2.21)$$

where $\phi(v, t)$ is wing stroke angle, $\psi(v, t)$ is wing rotation angle, $g_\phi(t)$ and $g_\psi(t)$ are the nominal harmonic functions, v_1 and v_2 scale the perturbation function, and $g_1(t)$ and $g_2(t)$ are the perturbation functions which are $g_{1,2}(t) = \sin^3\left(\frac{1}{2}\omega t\right)$, where ω is the nominal flapping frequency. The scaling parameters, v_1 and v_2 are the control inputs which are used to define how much the wing trajectory varies from its nominal path [24]. Thus, four parameters are used to define the trajectory of the two wings. The perturbation functions, $g_1(t)$ and $g_2(t)$, are chosen to be twice continuously differentiable so that the 2nd-order dynamics of the wing actuators will not detect any discontinuities from one wing-beat to the next, an advantage over the split-cycle, constant period strategy described in detail below.

Given a method for altering the wing kinematics, it is necessary to identify how the kinematic parameters relate to the aerodynamic wrench. In traditional aircraft control, this takes the form of aerodynamic derivatives resulting from the linearization process that show how a small perturbation of a given input changes a given output [82:76]. These derivatives are analytically derived and experimentally validated. Deng, et al. were unable to analytically derive the aerodynamic derivatives, so instead, they ran

simulations in which the input parameters were randomly selected, and the wrench output calculated based on their quasi-steady aerodynamic equations. After many such simulations they were able to construct a mapping between the input parameters and the aerodynamic wrench. As long as the parameters satisfied: $\|v\|_{\infty} \leq 1$, the mapping was accurate. Finally, they developed feed-forward control for the wing trajectory which predicts the necessary actuator voltage required to create the desired wing motion. Using a 2nd-order linear model of the thorax-wing structure they show that their feed-forward control can track representative control inputs. However, they do not address the frequency response of this tracking, nor do they cite any hardware testing. As will be shown, this should not be taken for granted, especially near resonance. Taken as a whole, the work performed by Deng, et al. is an impressive first step toward flapping wing MAV control. They covered every major component of control system design, the only drawback being their lack of hardware validation.

A similar, but more recent control system design and simulation was published by Dickson, Straw and Dickinson in 2008 [26]. They modeled the flight control of a *Drosophila* with the goal of building an open framework for insect flight simulation that could be improved as our knowledge of insect flight mechanics grows. Their model included a simulated environment to feed information to a sensors model that estimated the insect's states which the control module used to generate desired wing kinematics that the rigid body dynamics and aerodynamics modules used to compute the "true" states. Because they were simulating an actual insect, they had full 3 DOF wing kinematics available for their controller, which is unlikely to be available in an MAV in the near

future. Nevertheless, many of their modeling techniques are of interest to the MAV designer.

The rigid body dynamics of the insect are modeled with a “physics engine”, which is commonly used in video game software to create physically honest renderings of motion based on Lagrangian dynamics. Therefore, the quasi-static assumption used by most researchers is not used by Dickson, et al., instead the two wings and body are each treated as separate rigid bodies, and instantaneous forces and moments are used to drive the dynamics simulation, rather than the cycle-averaged aerodynamic wrench. They use a quasi-steady-state aerodynamics model to compute the instantaneous wrench that is similar to that used by Deng et al., however, they include terms for added mass, and drag on the insect body. The added mass term is similar to F_a given in Eq. 2.7, and the body drag terms were experimentally determined in a tow tank.

After examining the literature on insect flight control, Deng et al. determined that the uncoupled motions of pitch, yaw, roll and velocity could be controlled by specific changes in wing kinematic patterns. The insect can pitch by changing the mean stroke angle of both wings in concert, yaw by changing the relative stroke amplitude between each wing, roll by changing the relative stroke plane angle between each wing, and accelerate by changing the stroke amplitude and frequency of both wings in concert. This mapping between wing kinematics and body motion has been observed in insects and is verified by the quasi-steady aerodynamic equations, giving MAV designers an excellent starting point for orthogonal MAV control.

Finally, Dickson, et al., propose a simple proportional control law for the insect attitude based on angular rate errors, which insects are suspected of using and experiments support [73]. Trajectory tracking uses a PID controller to ensure desired performance. The integrated fly model was simulated and it was able to regulate its flight path down a simulated corridor. To assess the stability robustness of the design, they measured a pseudo gain and phase margin by individually opening each feedback loop, perturbing the input and measuring the response. Though not directly related to gain and phase margin because this was not a linear system, their assessment demonstrated a robust design with pseudo gain and phase margins of 11-20dB and 32° - 86° , respectively. Dickson, et al.'s work from a biological perspective should be of interest to MAV designers as a possible upper bound of control system complexity and for several of the modeling techniques they used such as the detailed quasi-steady aerodynamic equations, time accurate dynamics and measures of stability robustness.

The two efforts described above represent the most complete multi-DOF control system concepts for flapping wing vehicles available in the literature. Other contributions to this field have been relatively minor. Hu et al., designed a control system based on modulating wing rotation timing and mid-stroke angle of attack and showed that 6 DOF vehicle control was possible, though they presented no mechanism design for controlling these kinematics [42]. Khan and Agrawal have published 2 papers that address flapping wing flight control using 3 DOF wing kinematics and an aerodynamic model based on their own experiments conducted on a dynamically scaled wing [48, 50]. Similar to Deng, et al.'s method, they draw upon averaging theory to

create a control scheme based on an average nominal wing trajectory with time-periodic perturbations from the nominal trajectory as control inputs. Again, some impressive analytical work is presented, but no hardware testing is used to validate their assumptions and design. Sakhaei and Liu presented a model-based predictive controller based on an unspecified vehicle requiring 3 DOF wing kinematics [69].

In more comprehensive work, researchers at the Naval Research Laboratory designed and built a 7.5cm flapping wing MAV prototype which included features for flight control. Their MAV was powered by a DC motor, but was designed to use shape memory alloy wires to move wedges that altered the kinematics of their drivetrain, and thus altered the wing kinematics. This control system was not actually implemented due to its complexity, but a simulation predicted 4 DOF of the MAV [39, 68]. Finally, AFRL researchers Oppenheimer, et al., proposed modulating wing angle of attack and flapping frequency for their “Prairie Flyer” MAV prototype powered by a DC motor. Their analysis showed that 4 DOF controllability was possible with such an arrangement, but so far, their experimental work has been inconclusive [65].

Control Concepts Based on Single DOF Wing Kinematics

The control concepts described above are all common in that they require the wings to flap with multiple DOF. More DOF require greater complexity, more actuation, increased vehicle weight, etc., so any control scheme that can provide adequate controllability with only one DOF in the wings will likely result in superior vehicle performance. Two such schemes have been proposed to date that seek a control design for the Harvard Robofly, or a similar vehicle. This design is novel in that wing rotation is

passive, rather than actively controlled. The first control technique, proposed by Finio, et al. [36, 37], suggests three kinematic variations for controlling the MAV as shown in Figure 2.8: symmetrically varying the wing stroke amplitude, asymmetrically varying the wing stroke amplitude and symmetrically varying the wing stroke bias. Such kinematic variations would act to alter the X-body force, the yawing moment (M_z) and pitching moment (M_y), respectively. These kinematics can be physically realized in two ways: First, a three actuator design that uses a primary wing flapping actuator in concert with two small shoulder actuators [36], or second, a hybrid actuator consisting of a smaller actuator mounted orthogonally on the tip of the larger wing drive actuator [37].

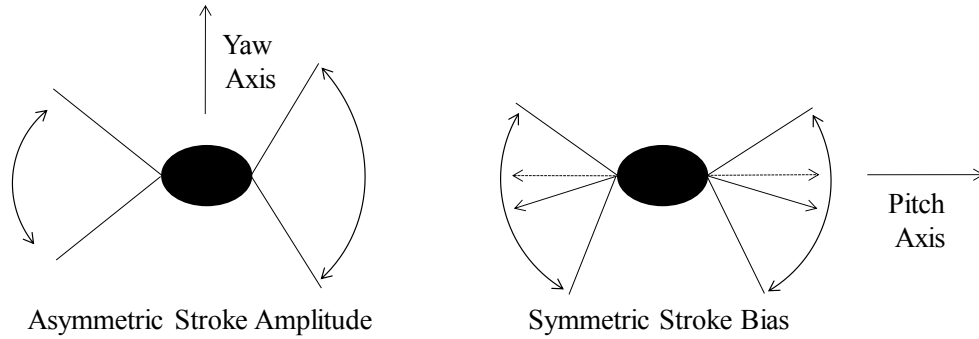


Figure 2.8. Kinematic variants for controlling the Harvard Robofly (adopted from [37]).

The three actuator design was analyzed, built and tested, representing the first flapping flight control hardware yet tested. They found that it was possible to change a wing's stroke amplitude using the shoulder actuator, but they were not able to significantly change the wing stroke bias, which they attributed to manufacturing defects in their prototype [36]. The hybrid actuator design produced similar kinematics, and again a prototype was built and tested to demonstrate the desired kinematics [37]. A

biological argument is used to predict the effectiveness of their control technique rather than an analytically derived mapping between wing kinematics and the aerodynamic wrench. Nevertheless, their ability to quickly build at-scale prototypes is impressive and gives them a hard-earned advantage in the race to achieve autonomous flapping flight.

In a related work, Oppenheimer, et al., from the Air Force Research Laboratory performed controllability analysis and simulation of Harvard's 3-actuator design [64]. They used blade element analysis to determine control derivatives which were used to develop control allocation laws for the simulated vehicle. The simulation demonstrated that, given certain assumptions, such a vehicle could track a virtual waypoint course, though the uncontrolled roll moments tended to drift. Another finding was that the yaw moment created by the asymmetric stroke amplitudes was mostly caused by the change in moment arm from the wing center of pressure to the vehicle COM, not the differing wing stroke amplitudes. This suggests that COM movement relative to the stroke plane could be used to create yaw and pitching moments.

The second control technique that requires only one actively controlled degree of freedom per wing was proposed by Doman, Oppenheimer, Bolender, and Siggthorssen in 2009 [27-31, 63]. Their initial concept involved modulating only wing stroke angle while moving a bobweight within the vehicle to attain 5-DOF control of the vehicle [29]. In the latest iteration, the requirement for the bobweight was eliminated by adding a bias to the wing stroke angle, essentially changing the mean stroke angle as proposed by Dickson, et al., and noted above [31].

In their first paper, Doman et al. present a simple control law for regulating altitude by modulating wing-beat frequency that utilizes the quasi-static assumption [27]. Their straightforward conclusion is that given cycle-averaged control inputs, altitude cannot be regulated to a finite point, rather it will oscillate with the wing-beat frequency about an equilibrium. Their second and third papers present their integrated control concept for the full rigid body dynamics, using a new technique they call Split-Cycle Constant Period Frequency Modulation (SCCPFM) which seeks to alter the wing stroke angular velocity from one beat to the next while maintaining a constant flapping frequency. Meanwhile, flapping frequency is also modulated to control thrust and altitude.

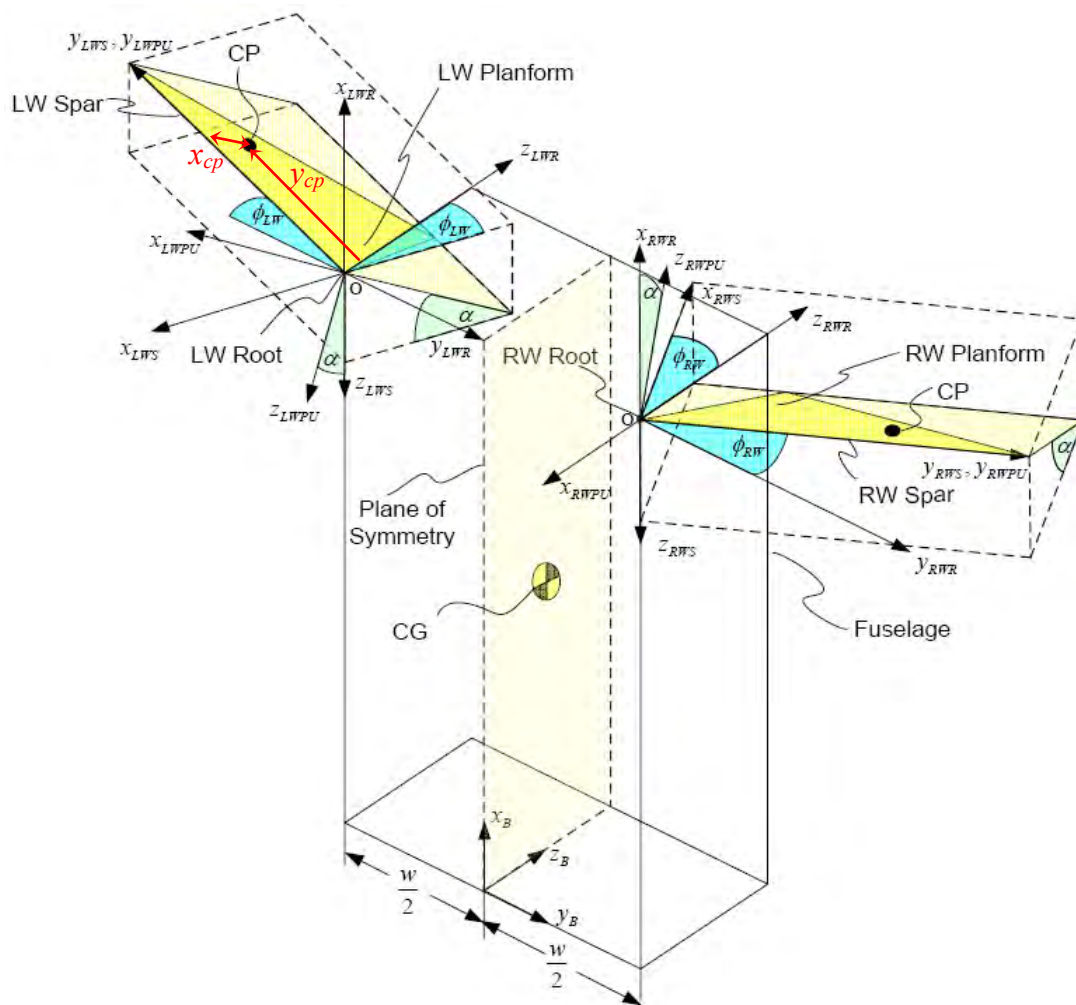


Figure 2.9. Coordinate frame definitions from [28]

Doman et al. use the coordinate frame definitions shown in Figure 2.9 which will be used in the following review. Further properties and coordinate transformations can be found in [28]. They use a quasi-steady model for predicting the aerodynamic wrench that is based on a simple blade element analysis identical to that presented in equations 2.5 and 2.6. For the aerodynamic force coefficients, C_L and C_D , they use an empirical formula obtained by testing on the Harvard Robofly wing model and published by Sane

and Dickinson [71]. These equations were determined for a wing modeled after a fruit fly, and would not be applicable unless the MAV had identical wings. Their quasi-steady model also uses a static location of the center of pressure whereas other models allowed this value to vary as a function of angle of attack. This simplification will likely decrease the accuracy of the aerodynamic moment calculations, but the significance of this cannot be determined without hardware testing.

Doman et al. propose altering the wing kinematics by increasing (decreasing) the frequency of the downstroke and decreasing (increasing) the frequency of the upstroke by an equivalent amount such that the total wing-beat period is left unchanged. Thus, the angular velocity is increased (decreased) on the downstroke and decreased (increased) on the upstroke. Such an asymmetry in the stroke angle profile can change the resulting cycle-averaged aerodynamic wrench produced by that wing, and by flapping the wings asymmetrically with respect to each other, the total aerodynamic wrench on the body can be controlled. The “split-cycle parameter”, δ , defines the stroke angle function as follows:

$$\phi_U(t) = \cos[(\omega - \delta)t] \quad \text{for} \quad 0 \leq t \leq \frac{\pi}{\omega - \delta} \quad (2.22)$$

$$\phi_D(t) = \cos[(\omega + \sigma)t + \xi] \quad \text{for} \quad \frac{\pi}{\omega - \delta} \leq t \leq \frac{2\pi}{\omega} \quad (2.23)$$

where:

$$\sigma = \frac{\delta\omega}{\omega - 2\delta} \quad \text{and} \quad \xi = \frac{-2\pi\delta}{\omega - 2\delta} \quad (2.24)$$

Define $\Delta = \delta/\omega$, then the shape of the waveform with frequency, ω , is governed completely by the split-cycle parameter, Δ . Figure 2.10 gives an example of a cosine

waveform advanced by a negative value of Δ .

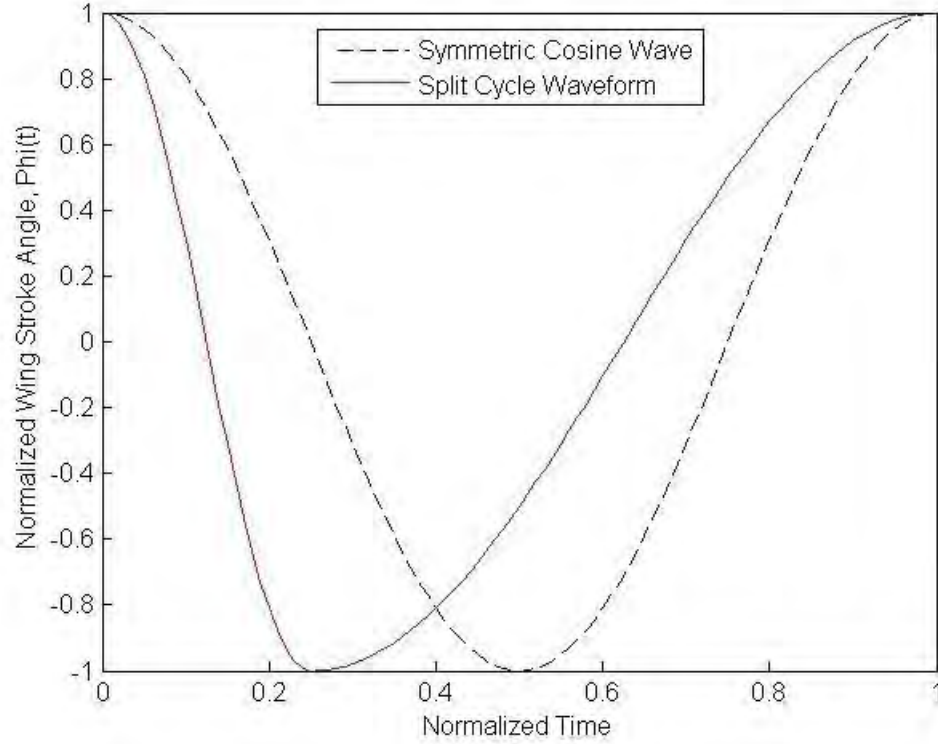


Figure 2.10. Split-cycle constant period frequency modulated waveform.

Recall, the purpose of the split-cycle waveform is to alter the angular velocity of the wing, which can be calculated by taking the derivative of the angular position and is:

$$\dot{\phi}_U(t) = -(\omega - \delta) \sin[(\omega - \delta)t] \quad \text{for} \quad 0 \leq t \leq \frac{\pi}{\omega - \delta} \quad (2.25)$$

$$\dot{\phi}_D(t) = -(\omega + \sigma) \sin[(\omega + \sigma)t + \xi] \quad \text{for} \quad \frac{\pi}{\omega - \delta} \leq t \leq \frac{2\pi}{\omega} \quad (2.26)$$

The angular velocity and acceleration of such a waveform are plotted in Figure 2.11 which clearly shows the increase in velocity on the upstroke compared to the downstroke. Figure 2.11 also highlights the piecewise discontinuous nature of the SCCPFM waveform which complicates its implementation.

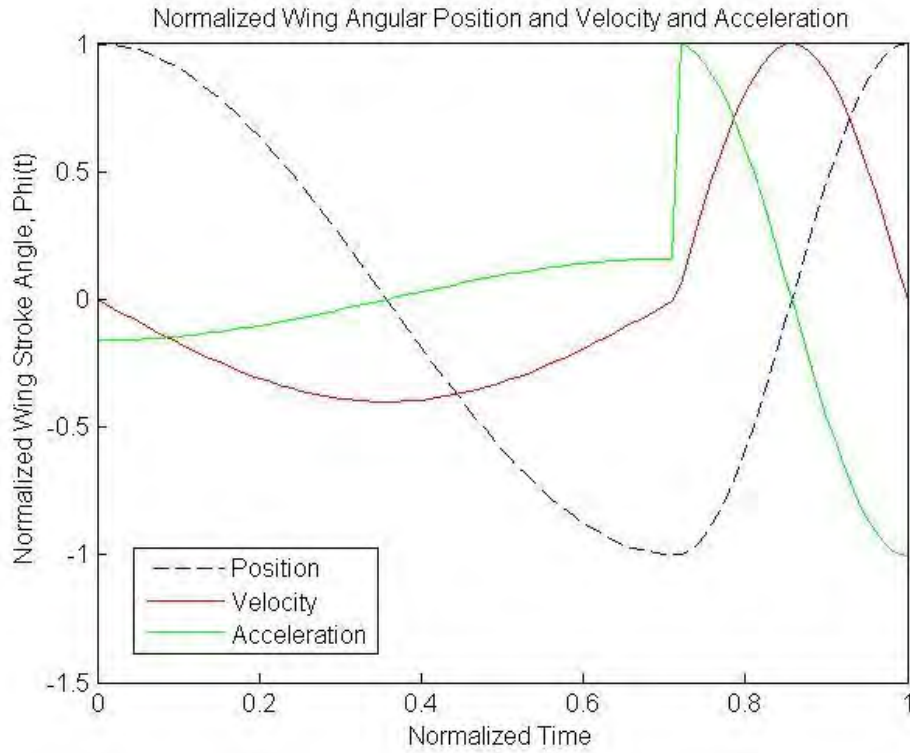


Figure 2.11. Normalized angular position, velocity and acceleration resulting from a split-cycle waveform

As shown by the quasi-steady aerodynamic equations, the aerodynamic wrench is directly proportional to the square of the wing angular velocity. Thus, by modulating the split-cycle parameter, δ , the relative angular velocity of the wing between the upstroke and downstroke can be modulated, and the aerodynamic wrench can be modulated.

The relationship between the control parameters, δ and ω , and the aerodynamic wrench is derived as follows. Let $G(t)$ represent a generalized force or moment aligned with a principal body axis resulting from a wing-beat. The cycle-averaged force is computed by integrating over the wing-beat period:

$$\bar{G} = \frac{\omega}{2\pi} \int_0^{\frac{2\pi}{\omega}} G(t) dt = \frac{\omega}{2\pi} \left[\int_0^{\frac{\pi}{\omega-\delta}} G(\phi_U(t)) dt + \int_{\frac{\pi}{\omega-\delta}}^{\frac{\omega}{\omega-\delta}} G(\phi_D(t)) dt \right] \quad (2.27)$$

Given the cycle-averaged generalized forces and moments, the control derivatives are then calculated relating the control parameters, δ_l , δ_r , ω_l and ω_r to the six generalized forces and moments:

$$\bar{G}_{\delta_l} = \left. \frac{\partial \bar{G}}{\partial \delta_l} \right|_{\delta_l=0, \omega_l=\omega_0} \quad (2.28)$$

$$\bar{G}_{\delta_r} = \left. \frac{\partial \bar{G}}{\partial \delta_r} \right|_{\delta_r=0, \omega_r=\omega_0} \quad (2.29)$$

$$\bar{G}_{\Delta\omega_l} = \left. \frac{\partial \bar{G}}{\partial \omega_l} \right|_{\delta_l=0, \omega_l=\omega_0} \quad (2.30)$$

$$\bar{G}_{\Delta\omega_r} = \left. \frac{\partial \bar{G}}{\partial \omega_r} \right|_{\delta_r=0, \omega_r=\omega_0} \quad (2.31)$$

These are linearized perturbation derivatives taken about the neutral hover positions. The control derivatives calculated by Doman et al., set their flight control design apart from others because they were able to derive closed-form derivatives. The other works cited resorted to biomimetic inspiration and experiments to measure the control derivatives [24, 26]. On the other hand, Doman et al. are using a simpler quasi-steady aerodynamic model that would simplify the derivation of control derivatives, though the derivation is still quite involved.

Taking into account the coordinate transformations from the wing local frame to the vehicle body frame, the six generalized body forces and moments resulting from the right and left wing individually are calculated resulting in 12 generalized force to wing relationships. These are summarized in Table 2.2. The control derivatives are then computed by taking the partial derivatives of the terms in Table 2.2 with respect to the four control parameters, δ_l , δ_r , ω_l and ω_r . The resulting control derivatives are given in Table 2.3. The control coupling can be determined by examining the table. The large number of zero terms means that the system is highly decoupled, and except for the Y axial direction (lateral), control about all DOF can be achieved with single DOF wings. This lateral motion can be achieved indirectly by rolling about the X axis and translating. Finally, Doman et al. successfully performed MATLAB simulations to demonstrate their control strategy, but since the simulation uses the same quasi-steady aerodynamic equations as their derivations, hardware testing is still needed to verify the utility of the design.

The works published in the literature to date on flapping wing control of MAVs represents an initial exploration of the topic, but they do not conclusively demonstrate the feasibility of the proposed methods. All of the research performed so far relies on unproven quasi-steady blade-element analysis to show the effectiveness of the proposed techniques. Furthermore, significant questions remain about the practical implementation of many of the proposed schemes including whether or not a mechanism design exists that is capable of creating the necessary wing kinematics and the ability of the wing flapping system to generate non-sinusoidal wing trajectories at or near resonance. Therefore, a novel control technique will be developed that accounts for feasibility of implementation, and this technique will be tested on hardware to demonstrate its feasibility.

Table 2.2. Generalized Forces and Moments from [28]

	Left Wing	Right Wing
X-Force	$\bar{X}_{LW}^B = \frac{k_L \omega_{LW}}{4} (2\omega_{LW} - \delta_{LW} + \sigma_{LW})$	$\bar{X}_{RW}^B = \frac{k_L \omega_{RW}}{4} (2\omega_{RW} - \delta_{RW} + \sigma_{RW})$
Y-Force	$\bar{Y}_{LW}^B = 0$	$\bar{Y}_{RW}^B = 0$
Z-Force	$\bar{Z}_{LW}^B = \frac{-k_D J_1(1) \omega_{LW}}{2} (\delta_{LW} + \sigma_{LW})$	$\bar{Z}_{RW}^B = \frac{-k_D J_1(1) \omega_{RW}}{2} (\delta_{RW} + \sigma_{RW})$
X Moment (Roll)	$\bar{M}_{x_{LW}}^B = \frac{k_D \omega_{LW} (\delta_{LW} + \sigma_{LW})}{4} (y_{cp}^{WP} + \omega J_1(1))$	$\bar{M}_{x_{RW}}^B = -\frac{k_D \omega_{RW} (\delta_{RW} + \sigma_{RW})}{4} (y_{cp}^{WP} + \omega J_1(1))$
Y Moment (Pitch) - Left Wing	$\bar{M}_{y_{LW}}^B = \frac{k_L \omega_{LW}}{2} \left[x_{cp}^{WP} J_1(1) \cos \alpha (\delta_{LW} + \sigma_{LW}) + \frac{\Delta z_L^B}{2} (2\omega_{LW} + \sigma_{LW} - \delta_{LW}) \right] + \frac{k_D J_1(1) \omega_{LW}}{2} \{ (\delta_{LW} + \sigma_{LW}) [x_{cp}^{WP} \sin \alpha + \Delta x_L^B] \}$	
Y Moment (Pitch) - Right Wing		$\bar{M}_{y_{RW}}^B = \frac{k_L \omega_{RW}}{2} \left[x_{cp}^{WP} J_1(1) \cos \alpha (\delta_{RW} + \sigma_{RW}) + \frac{\Delta z_L^B}{2} (2\omega_{RW} + \sigma_{RW} - \delta_{RW}) \right] + \frac{k_D J_1(1) \omega_{RW}}{2} \{ (\delta_{RW} + \sigma_{RW}) [x_{cp}^{WP} \sin \alpha + \Delta x_R^B] \}$
Z Moment (Yaw)	$\bar{M}_{z_{LW}}^B = \frac{k_L \omega_{LW}}{2} \left[\left(y_{cp}^{WP} J_1(1) + \frac{\omega}{4} \right) (2\omega_{LW} - \delta_{LW} + \sigma_{LW}) \right]$	$\bar{M}_{z_{RW}}^B = \frac{-k_L \omega_{RW}}{2} \left[\left(y_{cp}^{WP} J_1(1) + \frac{\omega}{4} \right) (2\omega_{RW} - \delta_{RW} + \sigma_{RW}) \right]$

Table 2.3. Control Derivatives from [29]

	δ_{LW}	δ_{RW}	ω_{LW}	ω_{RW}
X	$\frac{\partial \bar{F}_{x_{LW}}^B}{\partial \delta_{LW}} = 0$	$\frac{\partial \bar{F}_{x_{RW}}^B}{\partial \delta_{RW}} = 0$	$\frac{\partial \bar{F}_{x_{LW}}^B}{\partial \omega_{LW}} = k_L \omega_0$	$\frac{\partial \bar{F}_{x_{RW}}^B}{\partial \omega_{RW}} = k_L \omega_0$
Y	0	0	0	0
Z	$\frac{\partial \bar{F}_{z_{LW}}^B}{\partial \delta_{LW}} = -k_D J_1(1) \omega_0$	$\frac{\partial \bar{F}_{z_{RW}}^B}{\partial \delta_{RW}} = -k_D J_1(1) \omega_0$	$\frac{\partial \bar{F}_{z_{LW}}^B}{\partial \omega_{LW}} = 0$	$\frac{\partial \bar{F}_{z_{RW}}^B}{\partial \omega_{RW}} = 0$
M _x	$\frac{\partial \bar{M}_{x_{LW}}^B}{\partial \delta_{LW}} = \frac{1}{2} k_D \omega_0 (y_{cp}^{WP} + \omega J_1(1))$	$\frac{\partial \bar{M}_{x_{RW}}^B}{\partial \delta_{RW}} = -\frac{1}{2} k_D \omega_0 (y_{cp}^{WP} + \omega J_1(1))$	$\frac{\partial \bar{M}_{x_{LW}}^B}{\partial \omega_{LW}} = 0$	$\frac{\partial \bar{M}_{x_{RW}}^B}{\partial \omega_{RW}} = 0$
M _y	$\frac{\partial \bar{M}_{y_{LW}}^B}{\partial \delta_{LW}} = J_1(1) \omega_0 [k_L x_{cp}^{WP} \cos \alpha + k_D (x_{cp}^{WP} \sin \alpha + \Delta x_L^B)]$	$\frac{\partial \bar{M}_{y_{RW}}^B}{\partial \delta_{RW}} = J_1(1) \omega_0 [k_L x_{cp}^{WP} \cos \alpha + k_D (x_{cp}^{WP} \sin \alpha + \Delta x_R^B)]$	$\frac{\partial \bar{M}_{y_{LW}}^B}{\partial \omega_{LW}} = k_L \Delta z_L^B \omega_0$	$\frac{\partial \bar{M}_{y_{RW}}^B}{\partial \omega_{RW}} = k_L \Delta z_R^B \omega_0$
M _z	$\frac{\partial \bar{M}_{z_{LW}}^B}{\partial \delta_{LW}} = 0$	$\frac{\partial \bar{M}_{z_{RW}}^B}{\partial \delta_{RW}} = 0$	$\frac{\partial \bar{M}_{z_{LW}}^B}{\partial \omega_{LW}} = 2k_L \omega_0 \left[y_{cp}^{WP} J_1(1) + \frac{\omega}{4} \right]$	$\frac{\partial \bar{M}_{z_{RW}}^B}{\partial \omega_{RW}} = -2k_L \omega_0 \left[y_{cp}^{WP} J_1(1) + \frac{\omega}{4} \right]$

3. A Novel Technique for Flapping Wing Control of MAVs

The simplest control technique that provides adequate controllability should be the first choice of the MAV designer. The 6-DOF control provided by Doman et al.'s concept is certainly adequate, so it holds the most immediate promise. However, many challenges to implementing this control strategy still exist. First, their analysis is based on the simplest quasi-steady aerodynamic model. Second, the angle of attack of the wings is assumed constant throughout the wing-beat, and wing-wing and wing-fuselage interactions are ignored. Finally, they avoided resonant flapping because they were unable to drive a piezo actuator to track the split-cycle waveform near resonance. This would be a disadvantage of this technique, if there is a benefit to resonant flapping as argued previously in Chapter 2. However, it might be possible to flap the wings with a similar, but simpler waveform. For example, a trajectory that contained only the lower harmonics of the split-cycle waveform would be easier to implement because it would be continuous, rather than piece-wise, so it wouldn't excite the higher modes of the wing – actuator system. Though any number of harmonics could be used, there is an increasing energetic cost for the higher harmonics as the higher frequencies are increasingly attenuated by the flapping system. The simplest waveform that exhibits split-cycle behavior is a two-harmonic waveform, therefore, a new control technique should be considered that is similar to the split-cycle technique, but that utilizes a continuous two-harmonic waveform and a fixed resonant flapping frequency.

3.1 Split-cycle, Constant Period, Amplitude Modulation

On the way to developing such a continuous wing flapping trajectory, a piecewise waveform will be considered first that is analogous to the final, continuous waveform. Consider a split-cycle, constant period wing trajectory that uses amplitude modulation instead of frequency:

$$\phi_U(t) = A \cos[\omega(1-\Delta)t] + \eta \quad \text{for} \quad 0 \leq t \leq \frac{\pi}{\omega(1-\Delta)} \quad (3.1)$$

$$\phi_D(t) = A \cos[\omega(1+\Sigma)t + \xi] + \eta \quad \text{for} \quad \frac{\pi}{\omega(1-\Delta)} \leq t \leq \frac{2\pi}{\omega} \quad (3.2)$$

where $\Sigma = \sigma/\omega$. The parameters A , η , and δ for each wing will be the six variable control parameters. Note that for a piezo-actuated flapping mechanism, amplitude, A , can be easily modulated [3]. For the purposes of this derivation, the parameters are held fixed during a wing-beat cycle, though when implemented, they may be allowed to change within a wing-beat. The assumption is that such changes would be “small” and “slow” relative to the nominal wing trajectory and flapping frequency. Therefore, the corresponding wing angular velocity for a given wing-beat is:

$$\dot{\phi}_U(t) = -A\omega(1-\Delta)\sin[\omega(1-\Delta)t] \quad \text{for} \quad 0 \leq t \leq \frac{\pi}{\omega(1-\Delta)} \quad (3.3)$$

$$\dot{\phi}_D(t) = -A\omega(1+\Sigma)\sin[\omega(1+\Sigma)t + \xi] \quad \text{for} \quad \frac{\pi}{\omega(1-\Delta)} \leq t \leq \frac{2\pi}{\omega} \quad (3.4)$$

The instantaneous aerodynamic forces on each wing can be estimated with a simple blade element calculation. The instantaneous lift and drag values for a differential strip of wing are:

$$dL = \frac{1}{2} \rho C_L(\alpha(t)) \dot{\phi}^2(t) y^2 c(y) dy \quad (3.5)$$

$$dD = \frac{1}{2} \rho C_D(\alpha(t)) \dot{\phi}^2(t) y^2 c(y) dy \quad (3.6)$$

where the wing geometry is defined in Figure 2.2. Integrating these over the length of the wing, the instantaneous lift and drag can be obtained for an entire wing:

$$L = \int_0^R dL = \frac{1}{2} \rho C_L(\alpha(t)) \dot{\phi}^2(t) I_A \quad (3.7)$$

$$D = \int_0^R dD = \frac{1}{2} \rho C_D(\alpha(t)) \dot{\phi}^2(t) I_A \quad (3.8)$$

Similar to the Harvard Robofly, and the vehicle proposed by Doman, et al., the wing rotation is passive, but limited by wing rotation stops. Therefore, the wing angle of attack is assumed to be constant throughout each half-stroke. This assumption simplifies the instantaneous lift and drag equations to:

$$L_U = k_L \dot{\phi}_U^2 \quad (3.9)$$

$$L_D = k_L \dot{\phi}_D^2 \quad (3.10)$$

$$D_U = k_D \dot{\phi}_U^2 \quad (3.11)$$

$$D_D = k_D \dot{\phi}_D^2 \quad (3.12)$$

where:

$$k_L = \frac{1}{2} \rho C_L I_A \quad (3.13)$$

$$k_D = \frac{1}{2} \rho C_D I_A \quad (3.14)$$

To understand how these contribute to the aerodynamic wrench, it is necessary to perform coordinate transformations. Consider the coordinate frame definitions given in Figure 2.9 where x_B, y_B, z_B represent the body-fixed coordinate frame. The right and left wings flap about the body-fixed X_{RWR} (right wing root) and X_{LWR} axes, respectively. The right wing velocity is in the direction of the rotating X_{RWS} (right wing spar) axis, and positive or negative, depending on whether it is the up-stroke or down-stroke. The left wing is similar. The wings' instantaneous aerodynamic forces in the rotating spar frames are then:

$$\vec{F}_R^{RWS} = \begin{bmatrix} -k_D \dot{\phi}_R^2 & k_D \phi_R |\dot{\phi}_R| \\ 0 & 0 \\ -k_L \phi_R^2 & k_L \phi_R^2 \end{bmatrix} \quad \vec{F}_L^{LWS} = \begin{bmatrix} k_D \phi_L |\dot{\phi}_L| & 0 \\ 0 & 0 \\ k_L \phi_L^2 & 0 \end{bmatrix} \quad (3.15)$$

The transformations from the spar frames to the body frame depend on the wing stroke angle, and are:

$$R_{RWS}^B = \begin{bmatrix} 0 & 0 & -1 \\ -\sin \phi_R & \cos \phi_R & 0 \\ \cos \phi_R & \sin \phi_R & 0 \end{bmatrix} \quad R_{LWS}^B = \begin{bmatrix} 0 & 0 & -1 \\ -\sin \phi_L & -\cos \phi_L & 0 \\ -\cos \phi_L & \sin \phi_L & 0 \end{bmatrix} \quad (3.16)$$

Therefore, the instantaneous forces on the MAV body resulting from the right and left wings are:

$$X_R^B = k_L \dot{\phi}_R^2 \quad (3.17)$$

$$X_L^B = k_L \dot{\phi}_L^2 \quad (3.18)$$

$$Y_R^B = k_D \dot{\phi}_R \left| \dot{\phi}_R \right| \sin \phi_R \quad (3.19)$$

$$Y_L^B = -k_D \dot{\phi}_L \left| \dot{\phi}_L \right| \sin \phi_L \quad (3.20)$$

$$Z_R^B = -k_D \dot{\phi}_R \left| \dot{\phi}_R \right| \cos \phi_R \quad (3.21)$$

$$Z_L^B = -k_D \dot{\phi}_L \left| \dot{\phi}_L \right| \cos \phi_L \quad (3.22)$$

In addition to these body forces, moments are also applied to the body by the wings.

These depend on the wing aerodynamic forces and the location of the centers of pressure of the wings. In the body frame, these are:

$$\vec{r}_{cp,R}^B = \begin{bmatrix} x_{cp} \sin \alpha + \Delta x \\ -\text{sgn}(\dot{\phi}) x_{cp} \sin \phi_R \cos \alpha + y_{cp} \cos \phi_R + \frac{w}{2} \\ \text{sgn}(\dot{\phi}) x_{cp} \cos \phi_R \cos \alpha + y_{cp} \sin \phi_R + \Delta z \end{bmatrix} \quad (3.23)$$

$$\vec{r}_{cp,L}^B = \begin{bmatrix} x_{cp} \sin \alpha + \Delta x \\ \text{sgn}(\dot{\phi}) x_{cp} \sin \phi_L \cos \alpha - y_{cp} \cos \phi_L - \frac{w}{2} \\ \text{sgn}(\dot{\phi}) x_{cp} \cos \phi_L \cos \alpha + y_{cp} \sin \phi_L + \Delta z \end{bmatrix} \quad (3.24)$$

The instantaneous moments on the body then result from the cross product

$\vec{M}^B = \vec{r}_{cp}^B \times \vec{F}^B$, they are:

$$M_{XR}^B = -k_D \dot{\phi}_R |\dot{\phi}_R| \left[y_{CP} + \frac{w}{2} \cos \phi_R + \Delta z \sin \phi_R \right] \quad (3.25)$$

$$M_{XL}^B = k_D \dot{\phi}_L |\dot{\phi}_L| \left[y_{CP} + \frac{w}{2} \cos \phi_L + \Delta z \sin \phi_L \right] \quad (3.26)$$

$$M_{YR}^B = k_L \dot{\phi}_R^2 \left[\text{sgn}(\dot{\phi}_R) x_{cp} \cos \phi_R \cos \alpha + y_{cp} \sin \phi_R + \Delta z \right] + k_D \dot{\phi}_R |\dot{\phi}_R| \left[x_{cp} \cos \phi_R \sin \alpha + \Delta x \cos \phi_R \right] \quad (3.27)$$

$$M_{YL}^B = k_L \dot{\phi}_L^2 \left[\text{sgn}(\dot{\phi}_L) x_{cp} \cos \phi_L \cos \alpha + y_{cp} \sin \phi_L + \Delta z \right] + k_D \dot{\phi}_L |\dot{\phi}_L| \left[x_{cp} \cos \phi_L \sin \alpha + \Delta x \cos \phi_L \right] \quad (3.28)$$

$$M_{ZR}^B = k_L \dot{\phi}_R^2 \left[\text{sgn}(\dot{\phi}_R) x_{cp} \sin \phi_R \cos \alpha - y_{cp} \cos \phi_R - \frac{w}{2} \right] + k_D \dot{\phi}_R |\dot{\phi}_R| \left[x_{cp} \sin \phi_R \sin \alpha + \Delta x \sin \phi_R \right] \quad (3.29)$$

$$M_{ZL}^B = -k_L \dot{\phi}_L^2 \left[\text{sgn}(\dot{\phi}_L) x_{cp} \sin \phi_L \cos \alpha - y_{cp} \cos \phi_L - \frac{w}{2} \right] - k_D \dot{\phi}_L |\dot{\phi}_L| \left[x_{cp} \sin \phi_L \sin \alpha + \Delta x \sin \phi_L \right] \quad (3.30)$$

These instantaneous body forces and moments are then separated into up- and down-stroke portions and summed over the wing-beat period, giving cycle-averaged body forces and moments:

$$\bar{X}_R^B = \frac{\omega}{2\pi} \int_0^{T_D} L_{RU} dt + \frac{\omega}{2\pi} \int_{T_D}^T L_{RD} dt \quad (3.31)$$

$$\bar{X}_L^B = \frac{\omega}{2\pi} \int_0^{T_D} L_{LU} dt + \frac{\omega}{2\pi} \int_{T_D}^T L_{LD} dt \quad (3.32)$$

$$\bar{Y}_R^B = \frac{\omega}{2\pi} \int_0^{T_D} -D_{RU} \sin \phi_{RU}(t) dt + \frac{\omega}{2\pi} \int_{T_D}^T D_{RD} \sin \phi_{RD}(t) dt \quad (3.33)$$

$$\bar{Y}_L^B = \frac{\omega}{2\pi} \int_0^{T_D} D_{LU} \sin \phi_{LU}(t) dt - \frac{\omega}{2\pi} \int_{T_D}^T D_{LD} \sin \phi_{LD}(t) dt \quad (3.34)$$

$$\bar{Z}_R^B = \frac{\omega}{2\pi} \int_0^{T_D} D_{RU} \cos \phi_{RU}(t) dt - \frac{\omega}{2\pi} \int_{T_D}^T D_{RD} \cos \phi_{RD}(t) dt \quad (3.35)$$

$$\bar{Z}_L^B = \frac{\omega}{2\pi} \int_0^{T_D} D_{LU} \cos \phi_{LU}(t) dt - \frac{\omega}{2\pi} \int_{T_D}^T D_{LD} \cos \phi_{LD}(t) dt \quad (3.36)$$

$$\begin{aligned} \bar{M}_{XR}^B = \frac{\omega}{2\pi} \left\{ \int_0^{T_D} D_{RU} \left[y_{cp} + \frac{w}{2} \cos(\phi_{RU}) + \Delta z \sin(\phi_{RU}) \right] dt - \right. \\ \left. \int_{T_D}^T D_{RD} \left[y_{cp} + \frac{w}{2} \cos(\phi_{RD}) + \Delta z \sin(\phi_{RD}) \right] dt \right\} \end{aligned} \quad (3.37)$$

$$\begin{aligned} \bar{M}_{XL}^B = -\frac{\omega}{2\pi} \left\{ \int_0^{T_D} D_{LU} \left[y_{cp} + \frac{w}{2} \cos(\phi_{LU}) + \Delta z \sin(\phi_{LU}) \right] dt - \right. \\ \left. \int_{T_D}^T D_{LD} \left[y_{cp} + \frac{w}{2} \cos(\phi_{LD}) + \Delta z \sin(\phi_{LD}) \right] dt \right\} \end{aligned} \quad (3.38)$$

$$\begin{aligned}
\bar{M}_{YR}^B = \frac{\omega}{2\pi} & \left\{ \int_0^{T_D} L_{RU} \left[-x_{cp} \cos(\phi_{RU}) \cos(\alpha) + y_{cp} \sin(\phi_{RU}) + \Delta z \right] - \right. \\
& D_{RU} \left[\Delta x \cos(\phi_{RU}) + x_{cp} \cos(\phi_{RU}) \sin(\alpha) \right] dt + \\
& \int_{T_D}^T L_{RD} \left[x_{cp} \cos(\phi_{RD}) \cos(\alpha) + y_{cp} \sin(\phi_{RD}) + \Delta z \right] + \\
& \left. D_{RD} \left[\Delta x \cos(\phi_{RD}) + x_{cp} \cos(\phi_{RD}) \sin(\alpha) \right] dt \right\}
\end{aligned} \tag{3.39}$$

$$\begin{aligned}
\bar{M}_{YL}^B = \frac{\omega}{2\pi} & \left\{ \int_0^{T_D} L_{LU} \left[-x_{cp} \cos(\phi_{LU}) \cos(\alpha) + y_{cp} \sin(\phi_{LU}) + \Delta z \right] - \right. \\
& D_{LU} \left[\Delta x \cos(\phi_{LU}) + x_{cp} \cos(\phi_{LU}) \sin(\alpha) \right] dt + \\
& \int_{T_D}^T L_{LD} \left[x_{cp} \cos(\phi_{LD}) \cos(\alpha) + y_{cp} \sin(\phi_{LD}) + \Delta z \right] + \\
& \left. D_{LD} \left[\Delta x \cos(\phi_{LD}) + x_{cp} \cos(\phi_{LD}) \sin(\alpha) \right] dt \right\}
\end{aligned} \tag{3.40}$$

$$\begin{aligned}
\bar{M}_{ZR}^B = \frac{\omega}{2\pi} & \left\{ \int_0^{T_D} -L_{RU} \left[x_{cp} \sin(\phi_{RU}) \cos(\alpha) + y_{cp} \cos(\phi_{RU}) + \frac{w}{2} \right] - \right. \\
& D_{RU} \left[\Delta x \sin(\phi_{RU}) + x_{cp} \sin(\phi_{RU}) \sin(\alpha) \right] dt + \\
& \int_{T_D}^T L_{RD} \left[x_{cp} \sin(\phi_{RD}) \cos(\alpha) - y_{cp} \cos(\phi_{RD}) - \frac{w}{2} \right] + \\
& \left. D_{RD} \left[\Delta x \sin(\phi_{RD}) + x_{cp} \sin(\phi_{RD}) \sin(\alpha) \right] dt \right\}
\end{aligned} \tag{3.41}$$

$$\begin{aligned}
\bar{M}_{ZL}^B = \frac{\omega}{2\pi} & \left\{ \int_0^{T_D} L_{LU} \left[x_{cp} \sin(\phi_{LU}) \cos(\alpha) + y_{cp} \cos(\phi_{LU}) + \frac{w}{2} \right] + \right. \\
& D_{LU} \left[\Delta x \sin(\phi_{LU}) + x_{cp} \sin(\phi_{LU}) \sin(\alpha) \right] dt + \\
& \int_{T_D}^T -L_{LD} \left[x_{cp} \sin(\phi_{LD}) \cos(\alpha) - y_{cp} \cos(\phi_{LD}) - \frac{w}{2} \right] - \\
& \left. D_{LD} \left[\Delta x \sin(\phi_{LD}) + x_{cp} \sin(\phi_{LD}) \sin(\alpha) \right] dt \right\}
\end{aligned} \tag{3.42}$$

where $T_D = \frac{\pi}{\omega(1-\Delta)}$, and $T = \frac{2\pi}{\omega}$. Substituting Eqs. 3.1-3.4 and 3.9-3.12 into Eqs.

3.31-3.42, and performing the integration, the resulting cycle-averaged forces and moments are:

$$\bar{X} = \frac{\omega^2 k_L A_R^2}{4} (2 - \Delta_R + \Sigma_R) + \frac{\omega^2 k_L A_L^2}{4} (2 - \Delta_L + \Sigma_L) \quad (3.43)$$

$$\bar{Y} = \frac{\omega^2 k_D A_R}{2} \sin(\eta_R) J_1(A_R) (\Delta_R + \Sigma_R) + \frac{\omega^2 k_D A_L}{2} \sin(\eta_L) J_1(A_L) (\Delta_L + \Sigma_L) \quad (3.44)$$

$$\bar{Z} = -\frac{\omega^2 k_D A_R}{2} \cos(\eta_R) J_1(A_R) (\Delta_R + \Sigma_R) - \frac{\omega^2 k_D A_L}{2} \cos(\eta_L) J_1(A_L) (\Delta_L + \Sigma_L) \quad (3.45)$$

$$\begin{aligned} \bar{M}_X = & -\frac{\omega^2 k_D A_R}{4} [y_{cp} A_R + w \cos(\eta_R) J_1(A_R) + 2\Delta z \sin(\eta_R) J_1(A_R)] (\Delta_R + \Sigma_R) + \\ & \frac{\omega^2 k_D A_L}{4} [y_{cp} A_L + w \cos(\eta_L) J_1(A_L) + 2\Delta z \sin(\eta_L) J_1(A_L)] (\Delta_L + \Sigma_L) \end{aligned} \quad (3.46)$$

$$\begin{aligned} \bar{M}_Y = & \frac{\omega^2 k_L}{2} \left\{ A_R [x_{cp} \cos(\alpha) \cos(\eta_R) J_1(A_R)] (\Delta_R + \Sigma_R) + \right. \\ & + A_L [x_{cp} \cos(\alpha) \cos(\eta_L) J_1(A_L)] (\Delta_L + \Sigma_L) + \\ & A_R \left[y_{cp} \sin(\eta_R) J_1(A_R) + \frac{\Delta z}{2} A_R \right] (2 - \Delta_R + \Sigma_R) + \\ & \left. A_L \left[y_{cp} \sin(\eta_L) J_1(A_L) + \frac{\Delta z}{2} A_L \right] (2 - \Delta_L + \Sigma_L) \right\} + \\ & \frac{\omega^2 k_D}{2} \left\{ A_R [\Delta x \cos(\eta_R) J_1(A_R) + x_{cp} \sin(\alpha) \cos(\eta_R) J_1(A_R)] (\Delta_R + \Sigma_R) + \right. \\ & \left. A_L [\Delta x \cos(\eta_L) J_1(A_L) + x_{cp} \sin(\alpha) \cos(\eta_L) J_1(A_L)] (\Delta_L + \Sigma_L) \right\} \end{aligned} \quad (3.47)$$

$$\begin{aligned}
\bar{M}_z = & \frac{\omega^2 k_L}{2} \left\{ A_R \left[x_{cp} \cos(\alpha) \sin(\eta_R) J_1(A_R) \right] (\Delta_R + \Sigma_R) - \right. \\
& - A_L \left[x_{cp} \cos(\alpha) \sin(\eta_L) J_1(A_L) \right] (\Delta_L + \Sigma_L) - \\
& A_R \left[y_{cp} \cos(\eta_R) J_1(A_R) + \frac{w}{4} A_R \right] (2 - \Delta_R + \Sigma_R) + \\
& \left. A_L \left[y_{cp} \cos(\eta_L) J_1(A_L) + \frac{w}{4} A_L \right] (2 - \Delta_L + \Sigma_L) \right\} + \\
& \frac{\omega^2 k_D}{2} \left\{ A_R \left[\Delta x \sin(\eta_R) J_1(A_R) + x_{cp} \sin(\alpha) \sin(\eta_R) J_1(A_R) \right] (\Delta_R + \Sigma_R) - \right. \\
& \left. A_L \left[\Delta x \sin(\eta_L) J_1(A_L) + x_{cp} \sin(\alpha) \sin(\eta_L) J_1(A_L) \right] (\Delta_L + \Sigma_L) \right\}
\end{aligned} \tag{3.48}$$

where $J_1(A)$ represents a Bessel function of the first kind. To determine how the six control parameters (A_R , A_L , Δ_R , Δ_L , η_R , and η_L) contribute to the aerodynamic wrench, partial derivatives are taken of each cycle-averaged force and moment with respect to each control parameter. These are then linearized about the hover condition ($A = A_0$, $\Delta = 0$, and $\eta = 0$). The resulting derivatives form the control effectiveness matrix given below. Note, it is defined that $\Delta z = 0$, as recommended by previous researchers [28] and which reduces the control parameters to five at a cost of losing controllability of sideforce, \bar{Y}^B , which was negligible at best.

$$\begin{bmatrix} \bar{X}^B \\ \bar{Y}^B \\ \bar{Z}^B \\ \bar{M}_X^B \\ \bar{M}_Y^B \\ \bar{M}_Z^B \end{bmatrix}_{\substack{A=A_0 \\ \Delta=0 \\ \eta=0}} = \omega^2 A_0 \quad (3.49)$$

$$\begin{bmatrix} k_L & k_L & 0 & 0 & 0 \\ 0 & 0 & 0 & 0 & 0 \\ 0 & 0 & -k_D J_1(A_0) & -k_D J_1(A_0) & 0 \\ 0 & 0 & -\frac{k_D}{2} \{A_0 y_{cp} + w J_1(A_0)\} & \frac{k_D}{2} \{A_0 y_{cp} + w J_1(A_0)\} & 0 \\ 0 & 0 & B_{53} & B_{54} & 2k_L y_{cp} J_1(A_0) \\ B_{61} & B_{62} & 0 & 0 & 0 \end{bmatrix} \begin{bmatrix} \Delta A_R \\ \Delta A_L \\ \Delta_R \\ \Delta_L \\ \eta \end{bmatrix}$$

where ΔA_R and ΔA_L denote the change in amplitude from the nominal condition (A_0)

and:

$$B_{53} = B_{54} = J_1(A_0) \{k_D (\Delta x + x_{cp} \sin \alpha) + k_L x_{cp} \cos \alpha\} \quad (3.50)$$

$$B_{61} = -B_{62} = -k_L \left\{ \frac{w}{2} + \frac{y_{cp}}{A_0} J_1(A_0) + \frac{y_{cp}}{2} (J_0(A_0) - J_2(A_0)) \right\} \quad (3.51)$$

3.2 Bi-harmonic Amplitude and Bias Modulation

The piecewise wing trajectory waveform described by Eqs. 3.1 and 3.2 cannot be tracked by a piezo actuator near resonance because the higher frequency elements of the waveform are attenuated by the wing flapper system dynamics, and the resulting wing motion at resonance is only simple harmonic motion. This behavior will be investigated

further in Chapter 5. To avoid this problem, it is desirable to limit the desired wing trajectory to a continuous waveform, containing only lower frequency content, and then compensate for the actuator dynamics to ensure that the actual wing motion matches the desired trajectory. Instead of a piecewise waveform, consider a sum of two continuous harmonic waveforms, also shown in Figure 3.1:

$$\phi(t) = A \{ M_1(\Delta) \cos[\omega t + \beta(\Delta)] - M_2(\Delta) \sin[2\omega t + 2\beta(\Delta)] \} + \eta \quad (3.52)$$

The terms M_1 , M_2 and β are functions of Δ and were developed through a Fourier series approximation of the piece-wise split-cycle waveform, which will be described in detail in Chapter 5. Such a waveform is sufficiently non-harmonic to create the desired cycle-averaged forces for control and it can be easily preconditioned at each harmonic frequency to compensate for the flapping system dynamics, and thus be tracked by an at-scale wing flapping mechanism [3, 4].

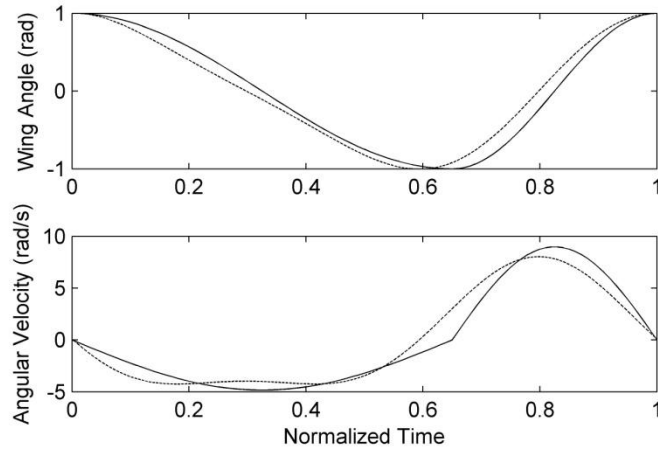


Figure 3.1. Comparison of the bi-harmonic waveform (Eq. 3.52, dashed) to the piecewise version (Eqs. 3.1 and 3.2).

This waveform is defined as the Bi-harmonic Amplitude and Bias Modulation control technique. How does this bi-harmonic approximation compare to the desired trajectory in terms of its ability to generate an adequate aerodynamic wrench for MAV control? This could be determined by performing a similar derivation as that described in Section 3.1 above, but it quickly becomes intractable. The integrands used to calculate cycle-averaged forces and moments shown in Eq. 3.43 - 3.48 have the form of a lift or drag force multiplied by a sine or cosine of the wing trajectory. In the piecewise case, these integrations are separated into up- and down-strokes, so the argument of the sine or cosine is a single trigonometric function. In this continuous case, the argument would be the entire expression of Eq. 3.52, which is three terms. Furthermore, by separating the up and down-stroke, the sense of the drag force is always clearly known, whereas in the continuous case, the sense of the drag force depends on the sense of the velocity. For

example, the expression for the cycle-averaged Z body force resulting from the right wing would be:

$$\begin{aligned}\bar{Z}_R^B &= \frac{\omega}{2\pi} \int_0^T D_R \cos \phi_R(t) dt = \\ &\frac{\omega}{2\pi} \int_0^T k_D \dot{\phi}_R |\dot{\phi}_R| \cos[AM_1 \cos(\omega t + \beta) - AM_2 \sin(2\omega t + 2\beta) + \eta] dt\end{aligned}\quad (3.53)$$

Compare this with the relatively simple expression given by Eq. 3.35. This integration does not have a closed-form solution.

A closed-form solution does exist for the X body force because it does not contain any drag terms or trigonometric terms resulting from a coordinate transformation:

$$\bar{X}_R^B = \frac{\omega}{2\pi} \int_0^T L_R(t) dt = \frac{\omega}{2\pi} \int_0^T k_L \dot{\phi}_R^2 dt \quad (3.54)$$

Substituting $\dot{\phi}(t)$:

$$\begin{aligned}\bar{X}_R^B &= \frac{k_L \omega^3 A_R^2}{2\pi} \int_0^T M_{1R}^2 \sin^2(\omega t + \beta_R) + 4M_{2R}^2 \cos^2(2\omega t + 2\beta_R) + \\ &4M_{1R}M_{2R} \sin(\omega t + \beta_R) \cos(2\omega t + 2\beta_R) dt\end{aligned}\quad (3.55)$$

$$\bar{X}_R^B = \frac{k_L \omega^3 A_R^2}{2\pi} \left[\frac{\pi}{\omega} (M_1^2(\Delta_R) + 4M_2^2(\Delta_R)) \right] = \frac{k_L \omega^2 A_R^2}{2} [M_1^2(\Delta_R) + 4M_2^2(\Delta_R)] \quad (3.56)$$

The derivation for \bar{X}_L^B is similar, the result is:

$$\bar{X}_L^B = \frac{k_L \omega^2 A_L^2}{2} [M_1^2(\Delta_L) + 4M_2^2(\Delta_L)] \quad (3.57)$$

From this cycle-averaged force, the linearized control derivatives can be calculated.

They are:

$$\left. \frac{\partial \bar{X}}{\partial A_R} \right|_{\substack{A_R=A_0 \\ \Delta_R=0 \\ \eta_R=0}} = k_L \omega^2 A_0 (M_{1R}^2 + 4M_{2R}^2) \quad (3.58)$$

$$\left. \frac{\partial \bar{X}}{\partial A_L} \right|_{\substack{A_L=A_0 \\ \Delta_L=0 \\ \eta_L=0}} = k_L \omega^2 A_0 (M_{1L}^2 + 4M_{2L}^2) \quad (3.59)$$

$$\left. \frac{\partial \bar{X}}{\partial \Delta_R} \right|_{\substack{A_R=A_0 \\ \Delta_R=0 \\ \eta_R=0}} = \left. \frac{\partial \bar{X}}{\partial \Delta_L} \right|_{\substack{A_L=A_0 \\ \Delta_L=0 \\ \eta_L=0}} = \left. \frac{\partial \bar{X}}{\partial \eta_R} \right|_{\substack{A_R=A_0 \\ \Delta_R=0 \\ \eta_R=0}} = \left. \frac{\partial \bar{X}}{\partial \eta_L} \right|_{\substack{A_L=A_0 \\ \Delta_L=0 \\ \eta_L=0}} = 0 \quad (3.60)$$

The remaining control derivatives cannot be found analytically because closed-form expressions for the cycle-averaged forces cannot be obtained. However, they can be computed numerically for a range of control inputs, and the derivatives can be observed graphically and compared to the closed-form derivatives that were obtained for the piece-wise approximation. If these are representative of the control effectiveness of the continuous Bi-harmonic version, the closed-form derivatives can be used instead.

The expressions for the remaining 5 instantaneous forces and moments are:

$$Y_R^B = k_D \dot{\phi}_R \left| \dot{\phi}_R \right| \sin \phi_R \quad (3.61)$$

$$Y_L^B = -k_D \dot{\phi}_L \left| \dot{\phi}_L \right| \sin \phi_L \quad (3.62)$$

$$Z_R^B = -k_D \dot{\phi}_R \left| \dot{\phi}_R \right| \cos \phi_R \quad (3.63)$$

$$Z_L^B = -k_D \dot{\phi}_L |\dot{\phi}_L| \cos \phi_L \quad (3.64)$$

$$M_{XL}^B = k_D \dot{\phi}_L |\dot{\phi}_L| \left[y_{cp} + \frac{w}{2} \cos \phi_L + \Delta z \sin \phi_L \right] \quad (3.65)$$

$$M_{YR}^B = k_L \dot{\phi}_R^2 \left[\text{sgn}(\dot{\phi}_R) x_{cp} \cos \phi_R \cos \alpha + y_{cp} \sin \phi_R + \Delta z \right] + k_D \phi_R |\phi_R| \left[x_{cp} \cos \phi_R \sin \alpha + \Delta x \cos \phi_R \right] \quad (3.66)$$

$$M_{YL}^B = k_L \dot{\phi}_L^2 \left[\text{sgn}(\dot{\phi}_L) x_{cp} \cos \phi_L \cos \alpha + y_{cp} \sin \phi_L + \Delta z \right] + k_D \phi_L |\phi_L| \left[x_{cp} \cos \phi_L \sin \alpha + \Delta x \cos \phi_L \right] \quad (3.67)$$

$$M_{ZR}^B = k_L \dot{\phi}_R^2 \left[\text{sgn}(\dot{\phi}_R) x_{cp} \sin \phi_R \cos \alpha - y_{cp} \cos \phi_R - \frac{w}{2} \right] + k_D \phi_R |\phi_R| \left[x_{cp} \sin \phi_R \sin \alpha + \Delta x \sin \phi_R \right] \quad (3.68)$$

$$M_{ZL}^B = -k_L \dot{\phi}_L^2 \left[\text{sgn}(\dot{\phi}_L) x_{cp} \sin \phi_L \cos \alpha - y_{cp} \cos \phi_L - \frac{w}{2} \right] - k_D \phi_L |\phi_L| \left[x_{cp} \sin \phi_L \sin \alpha + \Delta x \sin \phi_L \right] \quad (3.69)$$

These expressions are numerically integrated over the wing-beat period to obtain cycle-averaged forces and plotted for a range of possible values of the five control parameters. The slopes of the resulting plots at the origin represent the linearized control derivative for that force/control parameter pair (compare to the control effectiveness matrix, Eq. 3.49). Similarly, Eqs. 3.43-3.48, the closed-form approximations of the cycle-averaged forces, are then evaluated over the same range of control parameters and plotted alongside, presenting a comparison of the approximate closed-form derivative to the exact numeric derivative. The results are shown in Figure 3.2 for the right wing only; the

left wing is similar. Forces are in milli-Newtons, moments are in $mN\cdot mm$, Δ is non-dimensional. Note that at the hover condition all forces and moments should be zero except the X-body force and the moment about the Z-axis (which would be countered by the left wing.)

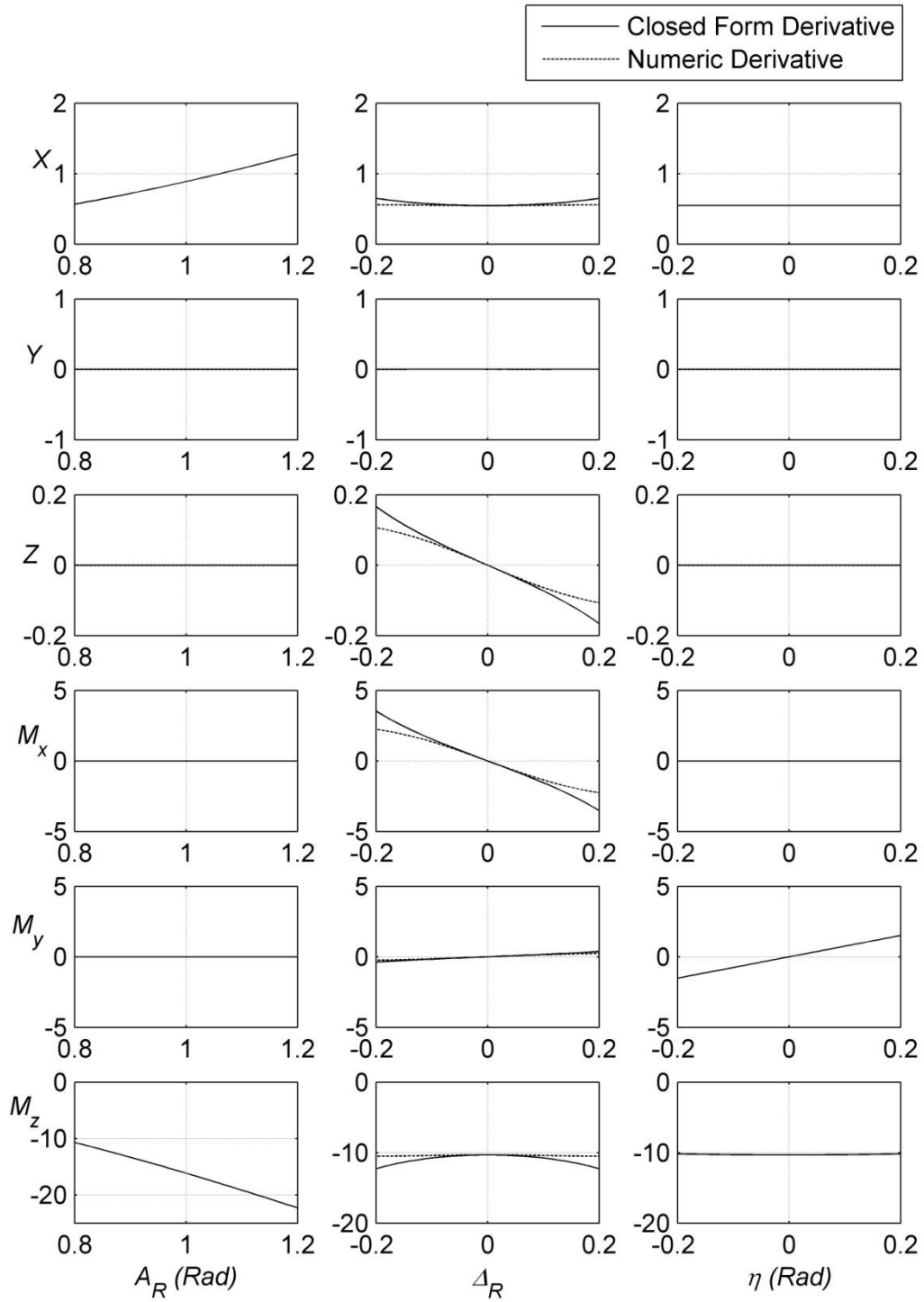


Figure 3.2. Comparison of approximate closed-form derivatives to exact numerical derivatives.

For amplitude (A_R) and wing stroke bias (η_R), the closed-form approximations (Eqs. 3.43-3.48) match the exact numerical derivative perfectly (columns 1 and 3 of Figure 3.2). This is expected because the Fourier approximation of the split-cycle wing trajectory should not inhibit amplitude and bias from altering the aerodynamic wrench. For the split-cycle parameter (Δ_R , column 2 of Figure 3.2), the slopes of the curves near the origin are identical, indicating that the control derivatives, linearized about the hover condition, are identical. As the split-cycle parameter increases away from the origin, the Fourier approximated bi-harmonic trajectory's ability to generate large contributions to the aerodynamic wrench saturates. This is also expected, as the two-term Fourier approximation has limited ability to track the split-cycle waveform as Δ_R increases, as will be shown in Chapter 5. Nevertheless, Figure 3.2 clearly shows that the closed-form control derivatives given in the control effectiveness matrix (Eq. 3.49) adequately capture the dynamics of the vehicle, and should be suitable for control system design.

The final conclusion of this analysis is that the proposed Bi-harmonic Amplitude and Bias Modulation control technique provides direct influence over 5 vehicle DOF while only requiring two actuators. The proposed MAV wing would have two DOF, but only one would be directly controlled, wing stroke angle, with three parameters of the wing stroke trajectory (amplitude, split-cycle parameter, and wing stroke bias angle) variable for generating contributions to the aerodynamic wrench. Furthermore, such a control scheme should be applicable to resonant wing flapping because it is a continuous waveform, offering a substantial advantage over similar control techniques. A summary of flapping wing control techniques that have been proposed in the literature is given in

Table 3.1. Each technique can be evaluated based on the number of actuators required to obtain the necessary wing kinematics and which vehicle DOF the technique can directly influence. The preferred technique is that which provides influence over the most vehicle DOF with the fewest actuators, while being applicable to resonant flapping. The Berkeley, Harvard and AFIT designs all claim resonant flapping capability, with the AFIT technique promising the greatest influence over vehicle DOF with the fewest actuators.

Table 3.1. Summary of kinematic variations used by various control techniques to impart aerodynamic wrench inputs.

	Insects [35]	Berkeley [24]	Caltech [26]	Harvard 1 [36]	Harvard 2 [37]	AFRL 1 [28]	AFRL 2 [31]	AFIT
Required Actuators	Dozens?	4	6?	3	2	3	2	2
Lift * X	Symmetric Amplitude	Symmetric Amplitude (v_I)	Symmetric Amplitude	Symmetric Amplitude (δ_I)	Symmetric Amplitude (δ_I)	Symmetric Frequency (ω)	Symmetric Frequency (ω)	Symmetric Amplitude (A)
Side Force Y	?	-	-	-	-	-	Asymmetric Stroke Bias (η) [†]	
Thrust * Z	?	-	-	-	-	Symmetric Split-Cycle (δ)	Symmetric Split-Cycle (δ)	Symmetric Bi-harmonic Split-Cycle (A)
Roll, M_x	Asymmetric Stroke Plane Angle & Amplitude	Asymmetric Rotation Timing (v_2)	Asymmetric Stroke Plane Angle	-	-	Asymmetric Split-Cycle (δ)	Asymmetric Split-Cycle (δ)	Asymmetric Bi-harmonic Split-Cycle (A)
Pitch, M_y	?	Symmetric Amplitude & Rotation Timing (v_I, v_2)	Symmetric Stroke Bias	Symmetric Stroke Bias (δ_I)	Symmetric Stroke Bias (δ_I)	Bob weight (V_{BW})	Symmetric Stroke Bias (η)	Symmetric Stroke Bias (η)
Yaw, M_z	Asymmetric Stroke Plane Angle & Amplitude	Asymmetric Amplitude (v_I)	Asymmetric Amplitude	Asymmetric Amplitude (δ_2, δ_3)	Asymmetric Amplitude (δ_2)	Asymmetric Frequency (ω)	Asymmetric Frequency (ω)	Asymmetric Amplitude (A)
Notes * X and Z align with lift and thrust direction only while hovering.	They get the job done	Kinematic mapping is not closed-form, but based on numerical simulation	Mapping based on insect observation, validated through simulation	Some Hardware Testing	Some Hardware Testing	F_z, M_x control not applicable to resonant flapping	F_z, M_x control not applicable to resonant flapping [†] Obtainable sideforce may be negligible	Some Hardware Testing

3.3 Remaining Assumptions

Flapping wing control of MAVs has been perfected by the *Insecta*, while human engineers have only recently begun exploring it. Several works have proposed control techniques along with analysis and/or simulation to demonstrate its feasibility. The ideal control technique would have direct influence over the most vehicle DOF with a simple flapping mechanism while operating at resonance for energy efficiency. Drawing on earlier research, a novel control technique has been proposed, Bi-harmonic Amplitude and Bias Modulation. The preceding analysis demonstrates that the bi-harmonic technique offers highly decoupled influence over five DOF, while only requiring two actuators. Furthermore it is applicable to resonant flapping, so it can be implemented with the least possible energetic cost to the MAV. The next step in developing this control technique is to evaluate it under more realistic conditions by incrementally eliminating the assumptions used to develop it. In fact, this is the next step for the field of flapping wing control, in general.

To date, flapping wing control of a MAV has not been demonstrated, only simulated. These simulations all rely on key assumptions, most notably, that the quasi-steady formulae accurately predict the instantaneous aerodynamic forces. To advance the field, these control techniques must be tested in the presence of unsteady aerodynamics. As no mathematical models yet exist that include such effects, short of time-consuming direct numerical simulation of the Navier-Stokes equations, the logical alternative is hardware testing. Flapping wing controllers should be implemented on prototype MAVs so that their resultant 6-DOF forces and moments can be directly measured. Such experiments

would validate the quasi-steady blade element models and the control derivatives predicted by them. If these predictions are deemed adequate, hardware-in-the-loop simulations could be performed, providing an intermediate step between simulation and autonomous flight, and answering several outstanding questions about flapping wing control, such as: Are quasi-steady predictions of the aerodynamic wrench adequate for control design? Are wing-wing interactions significant? How does a given control technique constrain a vehicle's design or limit its performance?

The remainder of this work will proceed to address these questions. First, it has thus far been assumed that the wings can be driven in a non-harmonic trajectory near resonance, or, more specifically, the bi-harmonic trajectory. Therefore, a flapping mechanism was designed and manufactured to test this assumption. Upon demonstrating that these non-harmonic wing trajectories are possible at resonance, a more complete MAV prototype was built to test the assumptions that the blade-element analysis adequately predicts the aerodynamic wrench used to predict control derivatives. Finally, limited hardware-in-the-loop experiments were performed to validate the Bi-harmonic Amplitude and Bias Modulation control technique.

4. Flapping Wing MAV Design and Fabrication

Along with similar control techniques in the literature, a novel technique has been proposed for controlling a MAV by modulating the forces generated by the flapping wings. This technique consists of prescribing wing stroke velocity as a function of three control parameters, A , Δ , and η that specify the amplitude, shape and bias of the wing flapping. A preliminary blade-element analysis of the cycle-averaged forces and moments generated by this Bi-harmonic Amplitude and Bias Modulated trajectory shows that 5 DOF control of a FWMAV should be possible, if certain assumptions hold true. To further study this proposed control technique, it is necessary to proceed beyond analysis and simulation by performing experiments on hardware.

As no suitable hardware was available for testing, devices were designed and built. The required bench testing does not necessarily require that the devices be capable of flight, but to increase the credibility of the results, efforts were made to come as close to a flight-worthy mechanism as allowed by our manufacturing capability. Therefore, the mechanism was built to full scale and designed as if it were going to be attached to a flight vehicle. Furthermore, recall that the major supposed benefit of the proposed control technique is that it can be used on a vehicle with only one actively controlled degree of freedom per wing. Therefore, the proposed mechanism allows for active control of the wing stroke angle and passive wing rotation, while constraining all other degrees of freedom. This simplifies the design and fabrication, but does limit the versatility of the resulting mechanism.

Because suitable piezoelectric actuators are available off-the-shelf, the prototype development proceeded initially with the most critical component, the wing flapping mechanism, or transmission, which couples the actuator to the flapping wings. Next the wing design and manufacture will be described, which are relatively simple by comparison, though critical to the mechanism performance. These two components coupled with an off-the-shelf actuator are the minimum hardware required to conduct preliminary testing of the aforementioned control techniques. Nevertheless, a vehicle fuselage and custom piezoelectric actuators were also designed and built, and this process will be described in the final section. These additional components allow for the assembly of a complete MAV prototype, which can be used for more extensive and realistic experimentation.

4.1 Flapping Mechanism Design and Fabrication

The flapping mechanism must convert the near linear motion of the piezo actuator tip into a rotary flapping motion of the wing. Various linkage designs for performing this conversion were described in Chapter 2. To simplify the manufacturing process, the simple four-bar mechanism described in Figure 2.6A was used initially. As our manufacturing capability improved, a more complicated linkage, like that of Figure 2.7 was incorporated to rotate the actuators out of the wing stroke plane.

Flapping Mechanism Kinematics

The geometry of the flapping mechanism and the resulting kinematics are chosen based on the expected displacement of the drive actuator and the desired wing motion. The mechanism was designed to have a wing stroke amplitude of $\pm 60^\circ$, for a total wing

stroke amplitude of 120° . The OPT 39.5/2.1/0.6 actuator from Omega Piezo has an advertised stroke of $\pm 1.2\text{mm}$. This was verified in the lab with no load. The design will be based on a maximum stroke of $\pm 1\text{mm}$.

To design the linkage geometry, a function was created in MATLAB to calculate the linkage kinematics from a given geometry, animate the wing trajectory and report the maximum and minimum wing stroke angle. The actuator was treated as a rigid body, rotating link, rather than a flexed cantilever. Figure 4.1 shows a generic four bar linkage with arbitrary geometry.

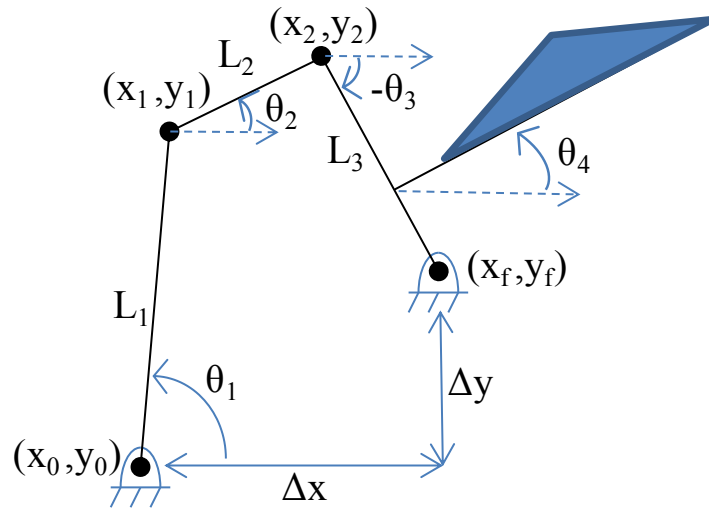


Figure 4.1. Four bar linkage kinematics.

To define the linkage, the link lengths, L_i , and the relative location of the ground points $(\Delta x, \Delta y)$ must be specified. Then, a given actuator deflection, θ_I defines the position of the linkage, which is calculated as follows. Given a specified actuator deflection, the location of point (x_I, y_I) can be calculated. The resulting gap from point (x_I, y_I) to point

(x_f, y_f) , here denoted (x, y) is spanned by what roboticists call a two-link planar manipulator, the solution of which is well documented, and is simply repeated here:

$$\theta_3 = - \left| 2 \tan^{-1} \sqrt{\frac{(L_2 + L_3)^2 - (x^2 + y^2)}{(x^2 + y^2) - (L_2 - L_3)^2}} \right| \quad (4.1)$$

and,

$$\theta_2 = \text{atan2}(y, x) + \text{atan2}(L_3 \sin \theta_3, L_2 + L_3 \cos \theta_3) \quad (4.2)$$

where *atan2* is the four-quadrant arctangent function. The wing stroke angle will equal that of θ_3 plus the bias that is given by its mounting position relative to link 3 (in the figure, it is 90°). Therefore, the position of the wing along link 3 is somewhat arbitrary, especially as $L_3 \rightarrow 0$ which it must in order to amplify the small actuator displacement into a large wing stroke.

The geometry was iterated until the satisfactory kinematics were achieved. The final design is summarized in Table 4.1:

Table 4.1. Proposed linkage geometry.

Links	Length (mm)
L_1	30
L_2	2
L_3	1.1102
Ground Position	
Δx	1.85
Δy	28.9

Figure 4.2 shows the MATLAB animation demonstrating the designed kinematic trajectory.

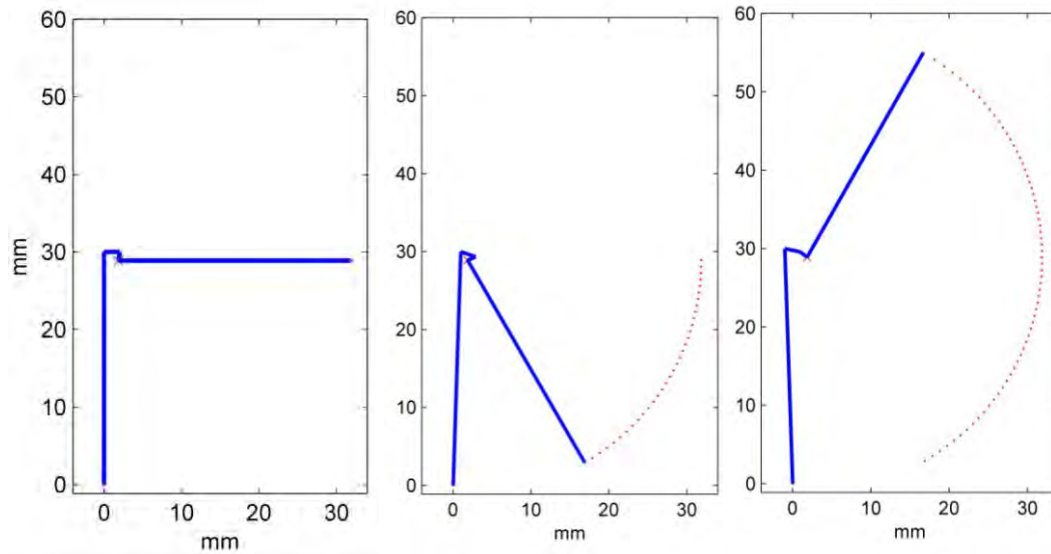


Figure 4.2. Matlab animation of desired wing flap kinematics.

Another important aspect of the wing kinematics is the transmission ratio; that is the relationship between the input actuator tip deflection and the output wing stroke angle. This is shown in Figure 4.3.

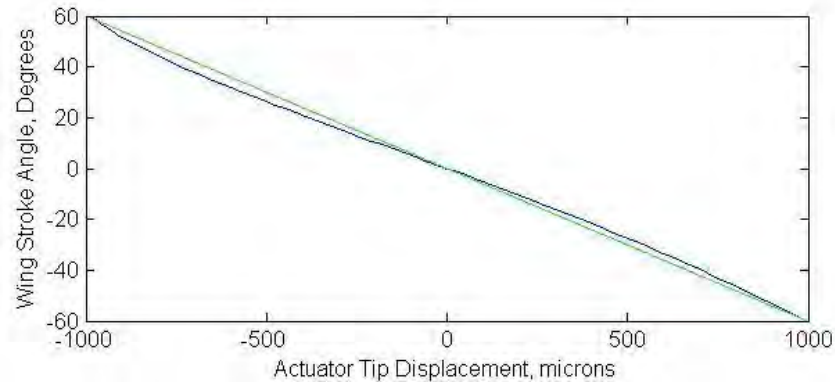


Figure 4.3. Transmission ratio; wing stroke angle vs. actuator tip deflection (blue). The green line is linear and is included for comparison.

Ideally, the transmission ratio would be constant, resulting in a linear plot. If that were the case, then the kinematics of the actuator would be directly proportional to the kinematics of the wings, and the linkage kinematics would not need to be corrected by the actuator input. No four bar linkage can achieve this, and the results shown here are quite good, so the linkage transmission will be assumed linear in the range specified.

The forces on each link can also be calculated quite easily which will be necessary for optimizing the structural design. The maximum force the actuator can apply to the linkage is called the blocking force, and is given for the selected actuator as 0.15N. Assuming the reaction force on the wing was sufficient to bind the linkage (the worst case), the static forces can be calculated with a straightforward free body diagram analysis. These are plotted on the linkage animation in Figure 4.4. The forces plotted as a function of actuator tip deflection are given in Figure 4.5. The forces plotted are the force on link 2, which is a two force member, so the force acts collinearly with the link, the reaction force at the ground pivot location of the wing, and the aerodynamic force

required by the wing to bind the linkage. These three forces make up the critical applied loads that will be necessary to complete the structural design of the links.

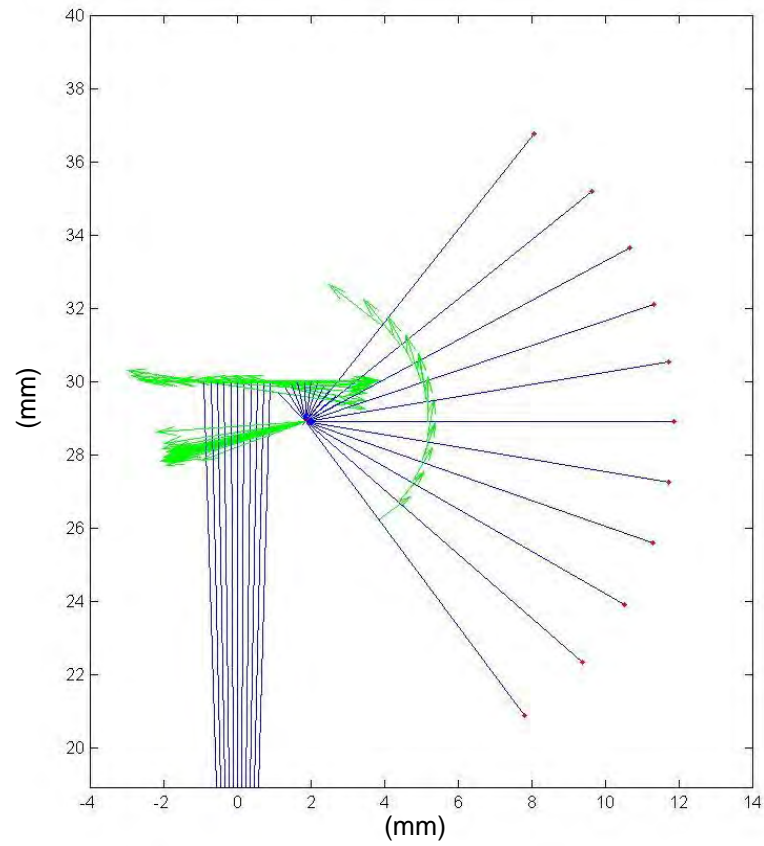


Figure 4.4. Link reaction force vectors (green) as the mechanism completes a stroke.

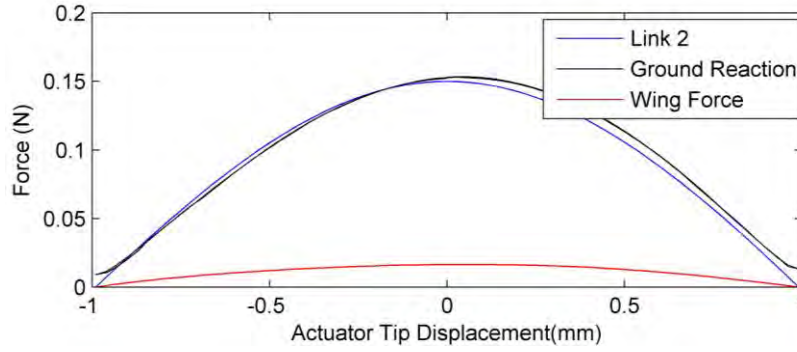


Figure 4.5. Link reaction forces (N) as a function of actuator tip displacement.

Once the link forces are known, it is possible to size the flexures, which can be treated as beams in bending, subject to a tensile or compressive force. Therefore, the flexures must be long enough to allow it to bend elastically through its desired range of motion, without yielding, while being short and/or stiff enough to resist buckling. The maximum stress in a beam with width, w , length, l , thickness, t , and moment of inertia, I loaded by a moment, M :

$$\sigma = \frac{Mt}{2I} = \frac{6M}{wt^2} \quad (4.3)$$

The deflection (rotation angle) of the beam tip with Young's Modulus, E :

$$\frac{dy}{dx} = \Delta\theta = \frac{ML}{EI} = \frac{12ML}{Ewt^3} \quad (4.4)$$

Solving for M and combining the two equations yields:

$$\sigma_{\max} = \frac{\Delta\theta Et}{2L} \quad (4.5)$$

The material properties and the desired flexure rotation angle are then substituted in and the necessary geometry can be determined. The Kapton used at AFIT is available in discrete sizes of $7.5 \mu m$, $12.5 \mu m$, and $25 \mu m$, limiting the thickness parameter. It has an elasticity of $2.5 GPa$ and yield strength of $69 MPa$. For the $12.5 \mu m$ Kapton and a desired elastic rotation of 60° , the flexures need to be greater than $237 \mu m$. The completed prototypes used $250 \mu m$ long flexures, which performed as expected.

In addition to ensuring the flexures don't yield, it might be desirable to keep the flexures as short as possible to maximize their stiffness. This might be beneficial if the flexures contribute to the wing-actuator system stiffness that determines the resonant flapping frequency. The relative contribution of the flexures can be estimated easily. An off-the-shelf actuator resonates at approximately $210 Hz$, so its stiffness can be backed out from the standard cantilever beam vibration equation [40]:

$$\omega_n = 210 Hz = 3.52 \sqrt{\frac{EI}{ml^3}} \quad (4.6)$$

The beam stiffness, K , is then:

$$K \approx \frac{9EI}{l^3} \approx 417.3 \text{ N/m} \quad (4.7)$$

When the beam bends to its maximum deflection of $1mm$, its stored energy is:

$$U = \frac{1}{2} kx^2 \approx 2.08 \times 10^{-4} \text{ Nm} \quad (4.8)$$

On the other hand, the flexures rotate an angle θ as a result of an applied moment, M :

$$\theta = \frac{Ml}{EI} \quad (4.9)$$

Using the relation; $k = M/\theta$, the stiffness of a flexure is, $k = EI/l$. Therefore, a $12.5 \mu m$ thick flexure, that is $4 mm$ wide and $250 \mu m$ long has a rotational stiffness of $6.5 \times 10^{-6} Nm$ and stores $3.5 \times 10^{-6} Nm$ of energy when rotated 60° . This is two orders of magnitude less than what the actuator stores during each flapping cycle, so the flexures as currently designed are not expected to make a significant contribution to the system stiffness.

Flapping Mechanism Fabrication

The manufacturing of insect-sized flapping mechanisms really distinguishes them from their bird-sized analogs. Traditional aircraft manufacturing methods are completely irrelevant, so novel techniques must be developed. Much progress in this area has been made by researchers at UC Berkeley [9-11] and Harvard [92-95] but more participation is needed to increase the pool of ideas to explore. For the size vehicle proposed here, many tools and techniques used for rapid prototyping printed circuit boards (PCBs) can be leveraged to manufacture MAVs. PCBs are essentially two-dimensional, though some small features exist out of plane, and are referred to as “2.5-D”. Though this constrains the design somewhat, these tools can cut parts repeatably and inexpensively with tolerances on the order of 1 micron. For example, one PCB prototyping vendor offers 29” x 29” build-to-print stencils in various materials delivered in days for under \$200. Contrast this with MEMS devices that have better tolerances but cost two orders of magnitude more, and take weeks or months to process. Furthermore, many of these PCB

prototyping tools are relatively inexpensive and can be acquired for in-house prototyping, which is described here.

In our lab at AFIT, flat materials can be quickly and easily cut on an Epilog 30 Watt Fibermark laser which is an Ytterbium air-cooled laser operating at a wavelength of 1062 nm. When available, parts can be cut with ultra-violet or infrared lasers operating with pulsewidths of nano-seconds or pico-seconds at Mound Laser and Photonics Center (MLPC) of Miamisburg, OH. MLPC is a collaborative research partner with the Air Force Institute of Technology and periodically provides laser micro-machining services for this project. The nano-second and pico-second lasers are able to remove less material with each pulse, but do so at a higher rate, resulting in greater precision and less damage to the remaining material. We have found that satisfactory results can be obtained for some parts (such as the fuselage, earlier versions of the transmission, and actuator parts) in the size range that we need with the simpler and cheaper Fibermark laser. As the capabilities of MLPC became available, more intricate parts were possible, and currently the transmissions, wings, and piezoelectric material are cut at MLPC on the pico-second laser.

In designing the assembly procedures, the goal is to increase consistency as much as possible. Two-dimensional shapes are cut automatically with a computer controlled laser then assembled into more complicated 3D shapes. It is essential that the parts be designed for ease of assembly to limit human error.

A functioning flapping linkage must have rigid links joined by efficient rotary joints. A clever technique for creating such a linkage that is very lightweight and

relatively easy to manufacture was developed by Wood, et al. at UC Berkeley [94]. This linkage uses carbon fiber (CF) for the rigid link and a polyimide membrane (Kapton) as a flexure joint. This configuration is shown in Figure 4.6

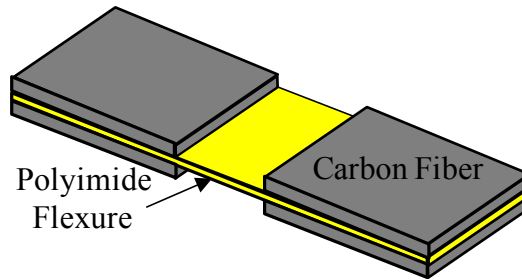


Figure 4.6. Carbon fiber and Kapton linkage.

The rigid links consist of cured unidirectional carbon fiber (CF), approximately 100 μm thick, while the rotary flexure joints are formed when Kapton is sandwiched between two pieces of CF. A precision linkage as described above can be built repeatably by using a three step process developed at AFIT, and shown in Figure 4.7. The process developed by Wood, et al., involved cutting out the pre-preg CF links (before curing) and manually assembling them on top of the Kapton flexure. This was a very tedious process that was prone to human error. Instead, the following process is used at AFIT. First, “pockets” are cut out of two cured pieces of CF where a flexure joint will eventually be. Next, Kapton is bonded between the two CF pieces with two layers of Pyralux² sheet adhesive (also with pockets cut out), creating a 5-layer laminate. Finally, the final perimeter of the desired linkage is cut out with the laser.

² DuPont™Pyralux® FR 1500 Sheet Adhesive
http://www2.dupont.com/Pyralux/en_US/products/adhesives_films/FR/FR_films.html

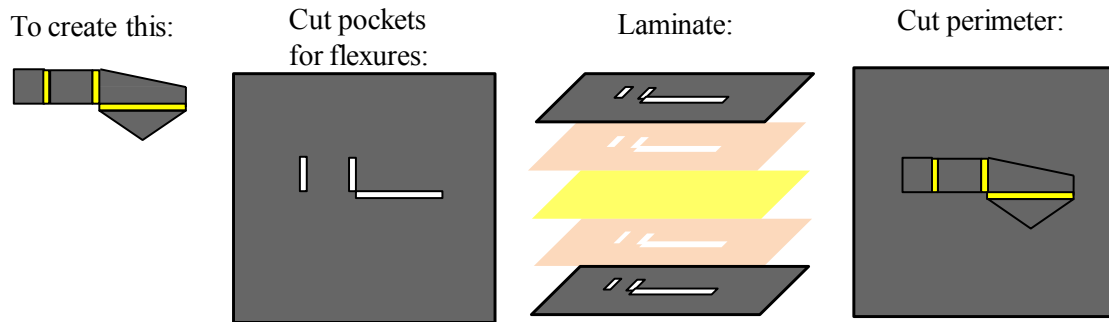


Figure 4.7. Carbon fiber linkage 3-step manufacturing process.

The two linkages that will eventually make up a single flapping mechanism are built with the above 2-D process, then the two laminates are joined and folded into the 3-D shape. This process is depicted in Figure 4.8 as follows: Photo A: Cured, single-ply, unidirectional CF is laser-cut with pockets pre-positioned to create the flexures in two mirror-image square blanks (B & C). D: Flexure material is laminated between the two mirror-image blanks on an alignment jig, and cured under pressure (E). F & G: The final perimeter is laser-cut creating rigid links joined by flexible Kapton membranes.

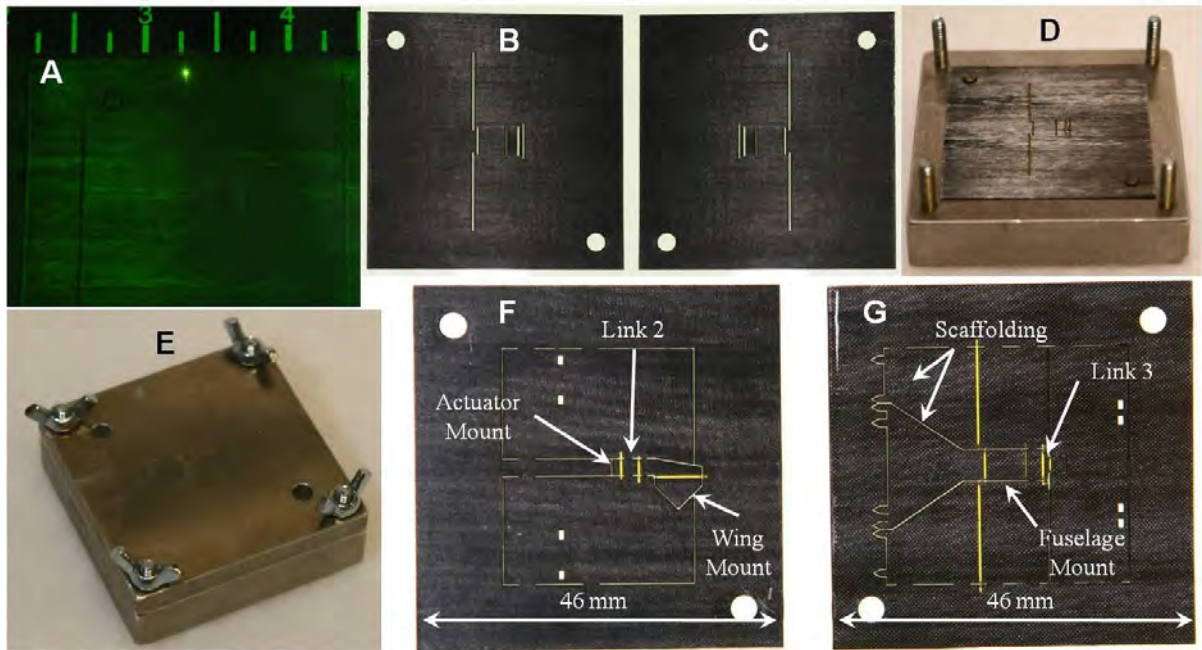


Figure 4.8. Composite laminate assembly.

Again, precision and repeatability are paramount in this process, so a special alignment fixture is used to ensure the flexure pockets align consistently. This fixture contains two precision alignment pins that accept the laser-cut CF link material with alignment holes drilled during the laser-cutting step (Figure 4.8B & C). This allows precision alignment on the order of microns. The final perimeter cut requires re-aligning the laminated structure with the laser, which is another opportunity to introduce human error. To mitigate this, the linkages are designed to tolerate some misalignment in that the flexure pockets are initially oversized, then trimmed during the perimeter cut. Evidence of this can be seen in Figure 4.8F & G. This ensures that the final product will capture the desired flexure geometry. The component shown in Figure 4.8F will make up the actuator attachment point, link 2 and the wing attachment point with the passive wing rotation

joint, while Figure 4.8G contains the fuselage attachment, link 3 and scaffolding to aid in the folding process.

The folding process, depicted in Figure 4.9, is more prone to human error. To make matters worse, the final folded geometry is critical to the final flapping kinematics, so it must be done correctly. Therefore, manufacturing aids such as scaffolding and alignment features are built into the parts which reduce guess work, and make it possible to accomplish the assembly and folding task in about 10 minutes. In addition, specialized tools, such as locking tweezers, micromanipulators and linear stages are used to attenuate hand movements and thus make it easier to align parts and hold them in place while adhesives cure. Figure 4.10 shows these alignment tools being used. On the left, a three-axis micromanipulator fitted with locking tweezers is used to hold a folded joint in place, while a “helping hand” soldering assistive device, also fitted with locking tweezers, and mounted on an X-Y linear stage holds the flapping mechanism.

The folding process, shown in Figure 4.9, proceeds as follows: Photo A: The two laminates are bonded together on the alignment jig with Cyano Acrylate (CA) glue, then the periphery is removed. B: Scaffolding is raised and held in place with alignment tabs to precisely locate the 3rd flexure joint; CA glue is used to fasten the link in position. C: Scaffolding is raised and inserted into alignment holes to precisely locate the fuselage attachment link and bonded with CA glue. D-F: After the CA dries, the scaffolding is carefully removed along the perforations, exposing the final linkage, G.

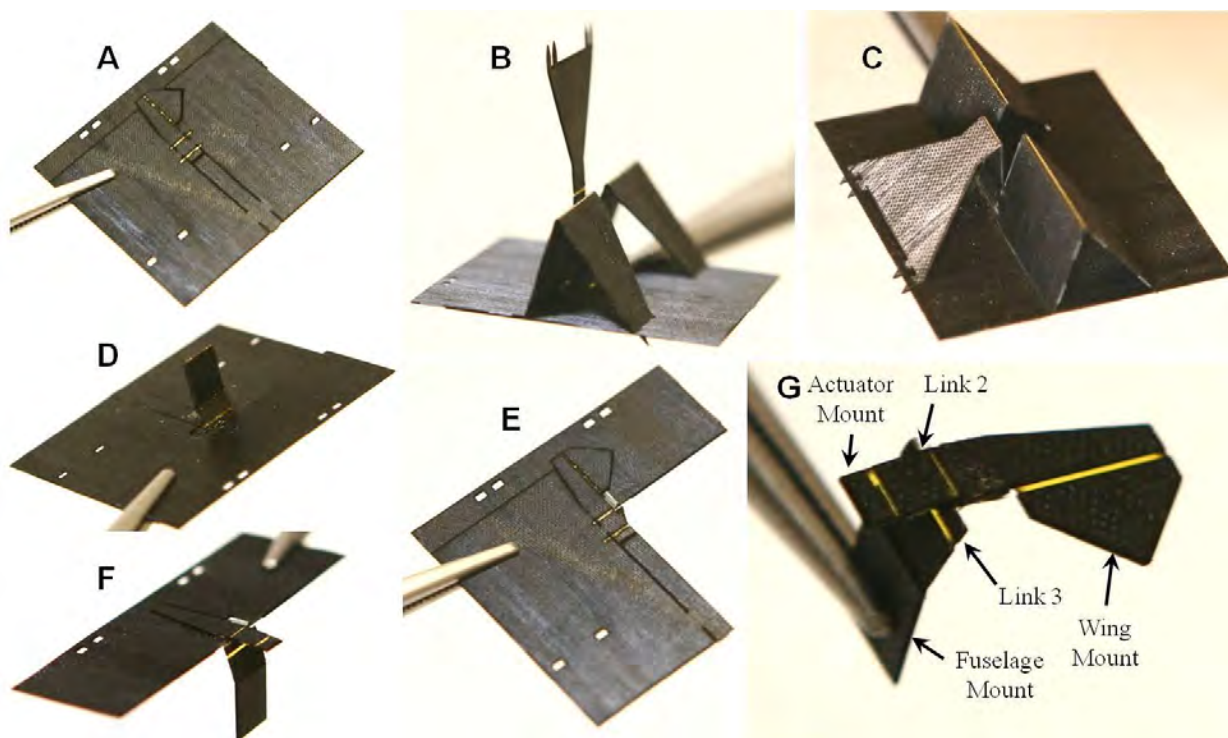


Figure 4.9. Folding of the flapping mechanism.

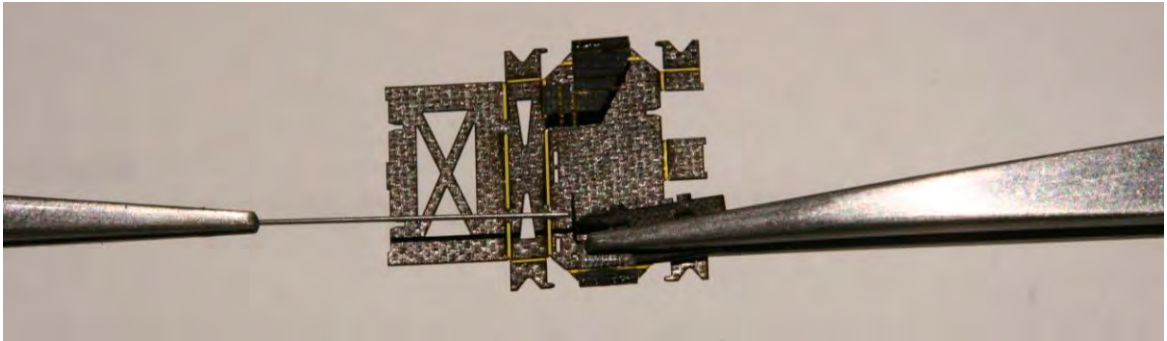


Figure 4.10. Precision alignment tools folding a version 4 flapping mechanism.

The completed mechanism was thoroughly tested. The mechanism can flap the wing with up to an 110° flapping amplitude, (slightly less than the desired 120°) when flapping at the resonant frequency ($\sim 30\text{Hz}$, depending on the attached wing). The resonant frequency of the system is very sensitive to the wing mass properties, and its maximum flapping frequency is limited by this. Flapping far beyond the resonant frequency would be inefficient, and can damage the wing and flapping mechanism. Preliminary lift force measurements (presented in Chapter 6) have recorded lift on the order of 1.5 mN per wing, which is consistent with blade element predictions for the frequency, amplitude and wing size.

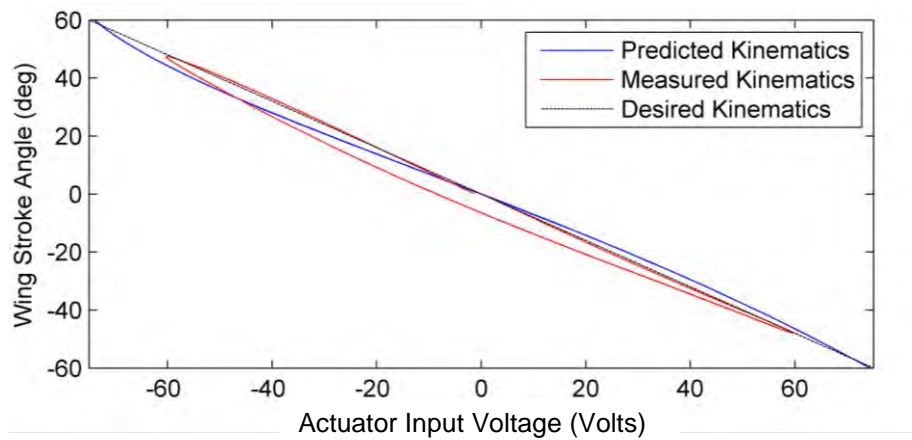


Figure 4.11. Measured wing kinematics compared to predicted and desired kinematics.

Figure 4.11 plots the wing kinematics measured with the laser vibrometer while flapping at 27 Hz . The vibrometer measures linear velocity, so the data was numerically integrated, and the wing assumed to be a rigid body. The hysteresis present in Figure 4.11 is due, in part, to the position drift inherent in the Doppler shift measurement technique, but may also be a result of wing flexibility. Nevertheless, the measured kinematics are excellent. The wing position is very nearly a linear function of the actuator input voltage, which is very desirable for the flight control techniques that will be evaluated with this mechanism.

The flapping mechanism shown in Figure 4.9 was the second prototype version designed and built at AFIT, and the first to be used in preliminary wing trajectory experiments. It was later incorporated in the first double-wing MAV prototype (described below) and eventually used for preliminary aerodynamic force and moment measurements. As noted above, the micro-machining capabilities of MLPC became

available, and more intricate designs were possible. The current version of the wing flapping mechanism at the completion of this manuscript is version 4. It utilizes identical linkage geometry to version 2 (shown in Table 4.1), but includes two additional flexures to allow the flapping actuator to be rotated 90° out of the wing stroke plane. This creates a more flight-worthy arrangement of the parts, placing the actuator in a more aerodynamic position, similar to an insect thorax. Figure 4.12 shows the evolution of the AFIT wing flapping mechanism.



Figure 4.12. Evolution of the AFIT wing flapping mechanism.

The wing flapping mechanisms evolved as follows. Version 1 utilized a C-shaped construction for the critical Link 3 that determines the linkage transmission ratio. This is easier to build, but heavy. Version 2 incorporated a lower-weight angled design for Link 3, and a narrower profile for all links in an attempt to increase flapping frequency. Version 3 was a major redesign, as a result of the increased capability provided by MLPC. For Version 3, two more flexures were added to rotate the actuator out of the wing stroke plane, the C-shaped Link 3 was re-instated because of the improved precision

available at MLPC, and the wing rotation joint was removed from the flapping mechanism and placed on the wing itself to make it easier to remove and replace wings. Version 4 is similar to Version 3, but includes a cover that folds over the actuators to stiffen the flapping mechanism. These are further described in Section 4.3.

4.2 Wing Design and Fabrication

Wing design is an extensive topic with many potential areas of specialization including aerodynamic force production and structural design that are beyond the scope of this research. Wing design for best aerodynamic and structural performance is still a topic of active research with AFIT students and AFRL researchers among those investigating this area [43, 51, 53, 62, 67, 68, 70, 74, 78]. Nevertheless, wings are needed to complete the planned controls experiments. To that end, wings were designed with bio-mimetic inspiration leaning towards manufacturability. Several previous researchers have built and tested insect sized wings, primarily at UC Berkeley [11], Harvard [84, 92] and the University of Florida [98, 99]. A unique approach using MEMS photolithography techniques was used by researchers at UCLA [67] to create insect-sized wings. The manufacturing techniques described in these works were studied extensively and where possible, they were attempted, but in the end a novel technique was developed at AFIT.

Initial attempts at wing fabrication consisted of manually laying pre-preg carbon fiber strands on 7.5 μm Kapton film and curing under 1 atm. These custom made wings were very lightweight and had the benefit of having continuous carbon fibers running parallel to the direction of the wing spars and veins. These wings were suitable for early

testing of the single wing flapping mechanism where it was not necessary to have two identical wings. Because the fibers were cut by hand with a razor blade, they were able to be trimmed very thin, but in an uncontrolled way. Therefore, these wings had low moments of inertia and yielded high flapping frequencies. Unfortunately, the curing process under simple vacuum would often result in the carbon fiber veins delaminating from the wing membrane.

As our experiments continued, it became necessary to have a more repeatable process for manufacturing wings. Two Master's students tackled this task in different ways. Capt Bob Dawson pursued a MEMS photolithography approach to wing manufacturing [22]. This approach had several benefits. First, all of the equipment required was already available in the AFIT clean room, second, the MEMS process requires virtually no manual steps, and is therefore, typically very repeatable. The MEMS technique has drawbacks as well. First, the photolithography process requires materials that react to etchants which limits the materials that can be used. Dawson used titanium for the wing veins, which compared to carbon fiber has a lower stiffness to weight ratio. Furthermore, the process for etching titanium turned out to be less repeatable than silicon etching, especially in the case of the high-aspect ratio features required for wings. Finally, this process requires very volatile chemicals. That said, the MEMS process is probably less costly to develop from scratch than an equivalent laser micromachining capability, which is a major advantage to those without access to expensive lasers. In the end, the titanium wings built with the MEMS technique were heavier than their carbon fiber counterparts, so they were not used. Nevertheless, this

manufacturing process is still very promising, and should be further refined to widen the material choices and improve repeatability.

Second Lieutenant Nate Sladek sought to build wings with carbon fiber spars and veins adhered to a thin film membrane [76]. The crux of his research was to develop a repeatable process for manufacturing the wing veins, either manually or otherwise, and characterize that repeatability. His initial efforts borrowed heavily from the work at the University of Florida in that aluminum molds were used to guide the hand-placing of carbon fiber veins. These wings consisted of a membrane supported by a rigid vein structure (carbon fiber). The wing fabrication process, summarized in Figure 4.13, is as follows. Eighty- μm thick uncured unidirectional prepreg carbon fiber overlaid with 12.5 μm thick Pyralux sheet adhesive is laser cut in the shape of the veins. A 7.5 μm Kapton membrane is also laser cut by placing the film between two glass plates which secure the Kapton and allow the laser energy to pass through. The cut wing components (Figure 4.13A) are then placed into a clamshell mold (Figure 4.13B) that has been treated with a wax mold release, and clamped (Figure 4.13C). The entire mold assembly is then cured under pressure. The result is a high-quality, repeatable wing weighing approximately 10 mg.

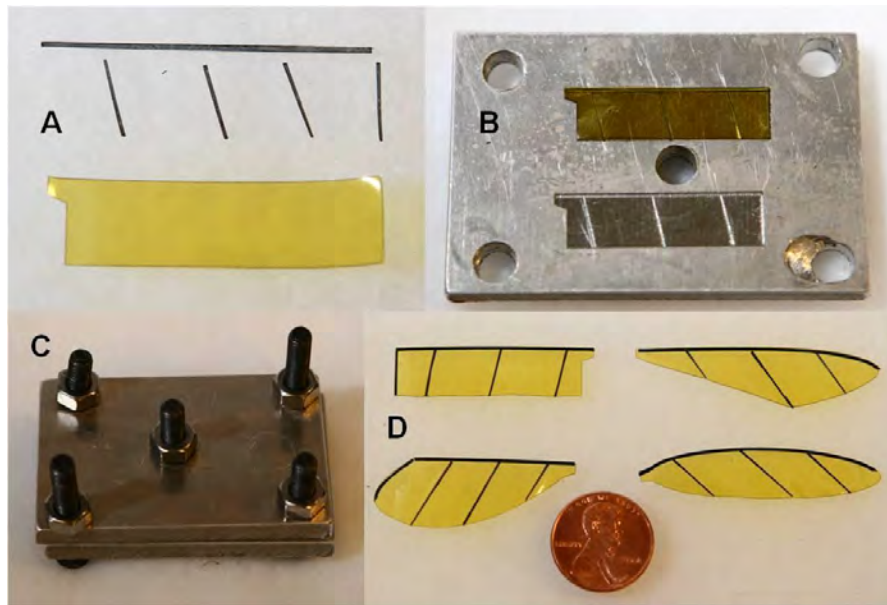


Figure 4.13. Sladek's initial wing manufacturing process.

Sladek characterized these wings according to their mass, aerodynamic force production, and modal frequency response, and the results were favorable. These wings were used in the first AFIT double-wing flapping MAV prototype. One disadvantage of these wings is the unidirectional carbon fiber. As long as the spar and veins are straight, unidirectional carbon fiber is adequate because the fibers can be oriented along the vein. However, if the veins curve at all, as is the case with 3 out of the 4 wing designs Sladek tested, then the curved cuts are cutting through fibers, and there are no continuous fibers running the length of the vein. In addition, the process of hand-placing carbon fiber vein pieces into the mold is very tedious and prone to error. Finally, it was desired to move the wing rotation joint off the flapping mechanism and onto the wing itself to ease the process of removing and replacing wings. Therefore, an improved technique was sought.

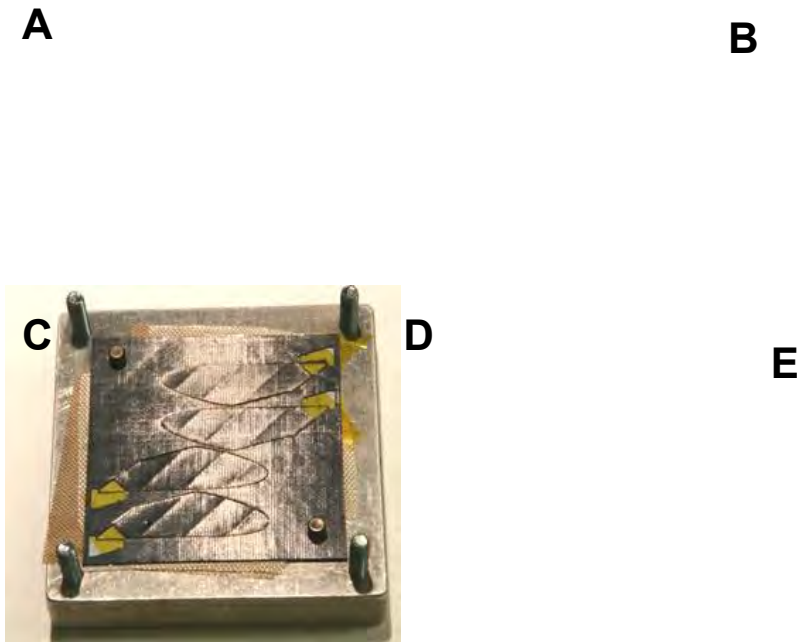


Figure 4.14. Improved wing manufacturing process.

The precise laser machining capabilities of MLPC along with a higher quality pre-preg CF material that is $50\ \mu\text{m}$ thick enabled a new wing manufacturing process. This is summarized in Figure 4.14. First, the CF is laid up in a 3-layer, 0-90-0 weave and cured under 100 psi in a hydraulic press. This compresses the laminate to a thickness of approximately $135\ \mu\text{m}$. This laminate is then covered in Pyralux sheet adhesive that is “tacked” to the CF with a heat gun. This CF-Pyralux laminate is then laser cut with pockets similar to the process described for the transmission in Section 4.1 (Figure 4.14A). A wing assembly consists of two different halves laminated together, with one half containing the wing spar and veins (Figure 4.14A *left*), and the other half without those features (Figure 4.14A *right*). This creates a wing whose mounting structure and rotation joint are 6 layers of CF thick, while the spar and veins are only 3 layers thick.

This reduces the inertia of the wing and increases the resonant flapping frequency. The 6 layer, double-laminate portion is required to properly sandwich the Kapton for the wing rotation joint. This technique makes it possible to create parts with varying thicknesses. These cutouts include two crosshairs which will aid alignment later. The half with the veins is then assembled on the clamp alignment jig with 12.5 μm Kapton placed over the wing rotation joints and 2.5 μm Mylar for the wing membrane (Figure 4.14 B). The other half is then placed over the first, and the CF pieces that were cut out of the second half have their pyralux removed then are placed back over the wings (Figure 4.14 C). These cutouts will apply pressure to the wing membrane during curing. The assembly is then clamped with high pressure (which improves the adhesion of the membrane) and cured, resulting in a complete wing assembly laminate (Figure 4.14

D). This laminate is precisely aligned with a camera and 4-axis linear stage system at MLPC using the aforementioned crosshairs, and the wing perimeter is cut out, yielding four completed wings (Figure 4.14 E). The alignment is absolutely critical, as it determines the thickness of the leading edge wing spar. Figure 4.15 shows an assortment of the various wings that have been designed and built at AFIT. They are arranged in chronological order (2010-2011 timeframe) starting in the upper left corner and proceeding from left to right.

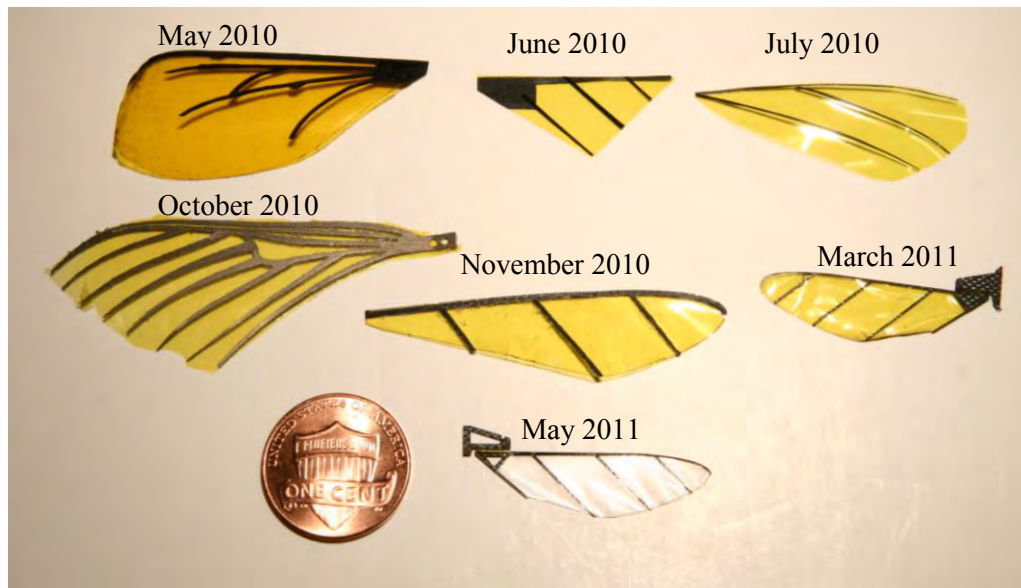


Figure 4.15. Evolution of AFIT wing designs.

4.3 Fuselage and Actuator Design and Fabrication

The flapping mechanisms and wings described above were sufficient for preliminary experiments to demonstrate wing trajectory tracking. As the research progressed to measuring aerodynamic forces and moments, it became necessary to develop a double-wing MAV prototype. The minimum features required are two wings, two flapping mechanisms, two actuators, and a fuselage to join the subsystems. The fuselage is relatively simple, having no moving parts. Its primary function is to provide a suitable boundary condition for the piezoelectric actuators and flapping mechanisms. Therefore, it should be as stiff as possible because the closer the actuator comes to an ideal “fixed” end boundary condition, the stiffer it will be, and the higher bandwidth the wing-actuator system will have.

The fuselage is made of CF using the multi-layered technique described above. The 2D parts are cut on the infrared laser at AFIT and, and folded along Kapton flexures into a 3D shape. The raw CF materials consisted of a 2-layer unidirectional layup, $200\ \mu\text{m}$ thick, so the final assembly was $400\ \mu\text{m}$ thick. The first fuselage design is shown in Figure 4.16. It is used with the version 2 flapping mechanism, which is a single wing flapper. Therefore, two of these mechanisms must be attached to the fuselage. The actuators are off-the-shelf *OPT 39.5/2.1/.7* piezo cantilevers from Omega Piezo. They slide into three bulkheads that provide their fixed end boundary condition and align them for proper insertion into the flapping mechanisms. This design was adequate for preliminary aerodynamic force testing. It was sufficiently stiff and robust enough to withstand the 4+ hours of simulated flight time necessary to collect the desired data.

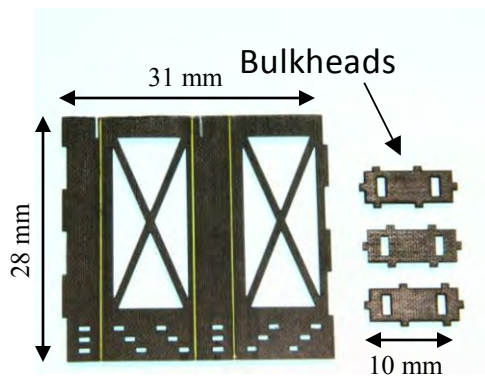


Figure 4.16. Version 2 fuselage, before and after folding.

The next fuselage iteration utilized the improved $50\ \mu\text{m}$ thick CF, assembled in a 3-layer, 0-90-0 weave. This created a final structure that is $300\ \mu\text{m}$ thick, and has bi-directional strength. The design was altered to be able to accept the version 3 flapping mechanism which is a double-wing flapper. The major changes included shortening the

fuselage slightly and including mating slots to precisely align the flapping mechanism on the fuselage.

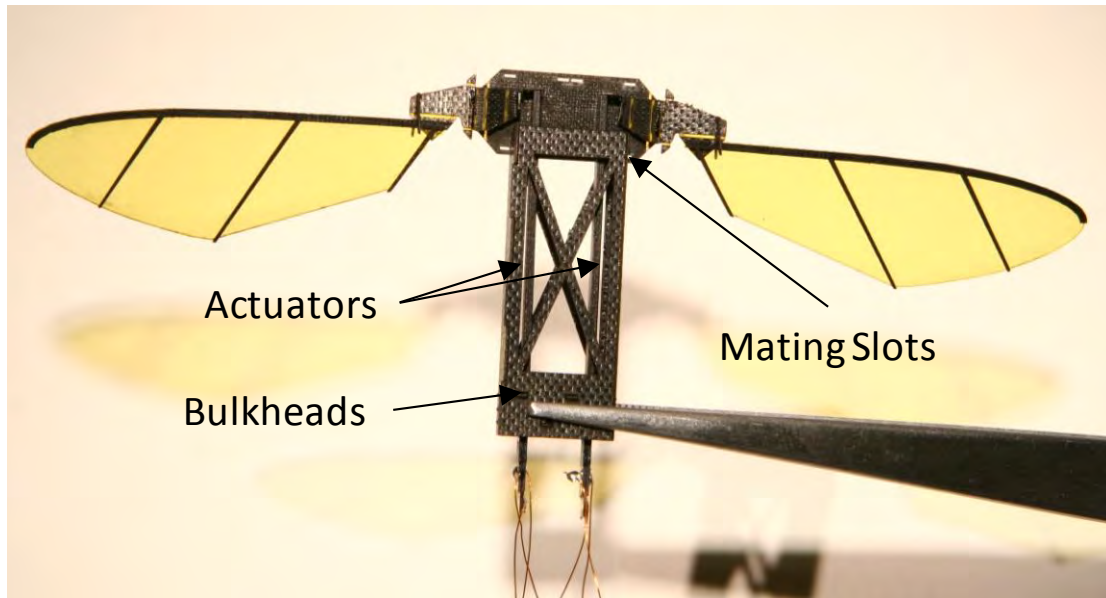


Figure 4.17. Version 3 fuselage.

The current fuselage, version 4, accepts custom-made actuators and the version 4 flapping mechanism. It is, therefore shorter, wider, and has more sophisticated mating features. Greater care was taken to reduce the weight in the hopes that this version would be capable of tethered flight. The assembly of this fuselage is summarized in Figure 4.18. Photo A: The two-part laminate is laser cut and cured. B: the actuators are fastened to the fuselage, and supplemental stiffeners are folded behind them. Care must be taken to ensure proper routing of the actuator leads. C: The walls are folded up into a box and glued in one step. D: The flapping mechanism is fastened to the fuselage with the aid of the mating slots, and wings are attached.

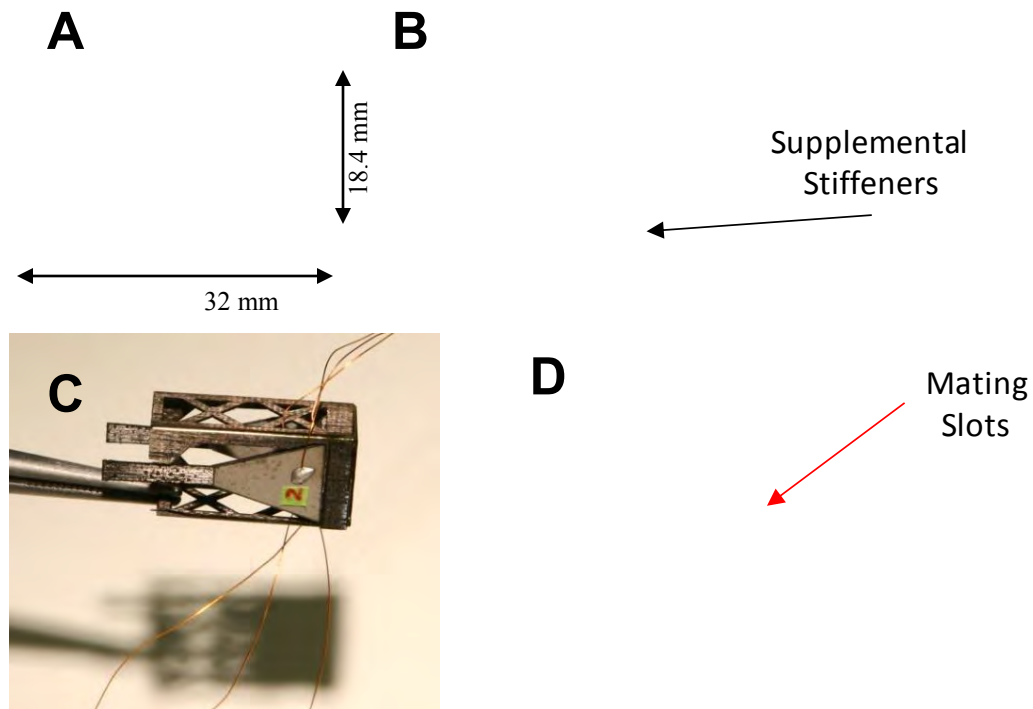


Figure 4.18. Version 4 fuselage assembly.

As our manufacturing capability has improved, it has become possible to build custom piezo-electric cantilever actuators at AFIT, motivated by the potential performance enhancements. Custom fabrication of high power-density piezo cantilever actuators was well described by Wood, et al. [96], and collaboration with students at Harvard enabled us to develop a custom fabrication capability very quickly. In its simplest form, a piezo cantilever actuator consists of a central structural beam with piezo-electric material sandwiched on the top and bottom. The central beam must form an electrical bond with the piezo material. The two piezo layers are then operated in opposition to each other with one side lengthening while the other shortens, and vice versa. Such actuation applies a moment to the beam and the tip deflects. There are

numerous possible variation on this fundamental design, including varying geometries of the constituent layers, poling directions of the piezo materials, and driving techniques.

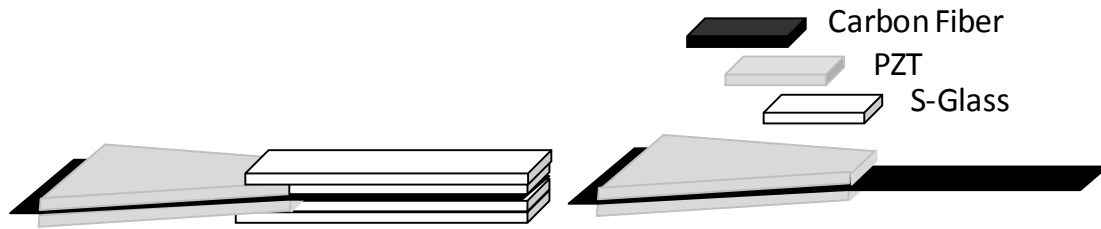


Figure 4.19. Harvard (left) and AFIT (right) actuator designs.

The design described by Wood, and used at Harvard utilizes $127\ \mu\text{m}$ thick PZT-5H piezoelectric material from Piezo Systems, inc. The PZT layers are parallel poled in the same direction. Harvard uses S-glass fiberglass to cover the carbon fiber tip, as shown in Figure 4.19. This acts as an electrical insulator, and stiffens the carbon fiber tip extension. At AFIT, a simpler design, without the S-glass tip extension was tested and compared to the Harvard design. We found that the tip extension does stiffen the actuator, but does not increase its resonant frequency. This is because the additional mass of the S-glass undermines the additional stiffness. Further, the electrical insulation is not needed because the actuator tip will be bonded to the flapping mechanism at link 2, which is separated from the other links by a Kapton flexure. Kapton is an insulator itself, so electrical current will not pass beyond link 2 of the flapping mechanism. This AFIT design is much easier to assemble.

As a powerplant for a potential flight vehicle, it is desirable for the actuator to produce as much power as possible for the lowest mass, referred to as power density.

Wood described several design rules to maximize the power density of a piezoelectric cantilever actuator, which can be summarized by seeking to push 100% of the PZT material to its failure limit when it is at maximum deflection [96]. Geometrically, this is accomplished by the trapezoidal shape shown in Figure 4.19, which provides more material near the root of the actuator, where the bending moment will be highest, and less material near the tip of the PZT. This ensures that all of the PZT material is stressed to its limit, not just the base of the cantilever. The drive technique also does this. PZT can be driven with higher voltage in the direction of poling than it can in the opposite direction. For example, the PZT we use can handle 300 volts in the poled direction, but only 100 volts in the anti-poled direction. Traditionally, such an actuator would be limited to run on ± 100 volts. However, an alternate technique is to apply a 200 volt DC bias across the entire actuator, then the drive signal can vary from -100 volts to +300 volts [96]. This ensures that the PZT is always driven within its limits, and that the material is pushed to the brink of failure. This draws the maximum power out of the actuator.

The actuator geometry has a significant impact on its performance. Mechanics of materials theory can be used to predict the performance of a piezoelectric cantilever actuator, and an excellent summary is provided by Wood, et al. [96]. Table 4.2 summarizes some conservative performance estimates for a range of actuator compositions in the size range required for the AFIT prototypes. In my experience, these estimates are accurate for mass and natural frequency and very conservative for

displacement (especially when the biased drive is used). Blocking force has not been measured at this time.

The width ratio defines the ratio of the base width to the tip width, and the higher the ratio, the greater power density the actuator should have. Width ratio is defined as:

$$w_r = \frac{2w_{base}}{w_{base} + w_{tip}} \quad (4.10)$$

The power density given in the table is calculated as:

$$\text{Power Density} = \frac{\text{Blocking Force} \times \text{Travel} \times \omega_n}{\text{Mass}} \quad (4.11)$$

This is not the true power density because the force produced by the actuator is not constant throughout the stroke, but this calculation allows for a simple comparison between different geometries. By this metric, it is clear from the table that increasing width ratio does increase power density, as does having more central CF layers, up to a point. Other noticeable trends are that blocking force is improved by having a wider base, shorter actuator, and more CF layers, all of which are a result of the ability of the PZT layers to generate a bigger moment about the neutral axis of the beam. Travel (range of motion) trades off against blocking force because it results from the beam having less stiffness, so it can be improved by having fewer CF layers and a longer actuator. A high resonant frequency requires the actuator to be very stiff, but low mass, so it benefits from a short actuator with more CF layers. Of the designs listed in the table, the “3-8-2-20” actuator has the highest power density at 2.1 W/g, so it was chosen for use in the final

MAV prototype. As a benchmark, the off-the-shelf actuator used on earlier prototypes has an estimated power density of only 0.6 W/g, based on its advertised specifications.

Table 4.2. Effects of geometry on predicted actuator performance.

Width Ratio	CF Layers	Base Width (mm)	Tip Width (mm)	PZT Length (mm)	Stiffness (N/m)	Mass (mg)	Blocking Force (mN)	Travel (μm)	ω_n (Hz)	Power Density (W/g)
1.5	3	7.32	2.44	20.4	966	120	232	240	697	2.03
	2	8.16	2.72	22.8	406	143	176	434	415	1.39
	4	8.16	2.72	22.8	1179	155	271	230	679	1.72
1.6	2	8	2	20	541	116	180	334	544	1.77
	3	8	2	20	1030	121	238	231	734	2.10
	4	8	2	22	1182	138	253	214	737	1.82
1.7	3	8	1.4	20	938	114	217	231	737	2.04

The actuators are fabricated in a molding process, as shown in Figure 4.20. The two PZT crystals are cut on a pico-second, UV laser at MLPC. The carbon fiber is uni-directional, with the fibers aligned with the longitudinal axis of the beam. It is cut on the aforementioned AFIT IR laser. A mold is created by cutting the desired shape out of Gel Pak, a compliant packing material that can withstand the curing temperatures. Spacers are cut out of porous Teflon which fills the gaps created by the unequal thickness of the various layers. The spacers are shaped so that they lock into place in the mold and do not move around, which eases assembly. The pieces are then painstakingly placed by hand into the Gel Pak mold, then clamped with light pressure and cured according to the requirements of the CF. When cured, leads are attached to the two PZT layers and the CF layer using silver oxide conductive epoxy which is easier to apply than solder.

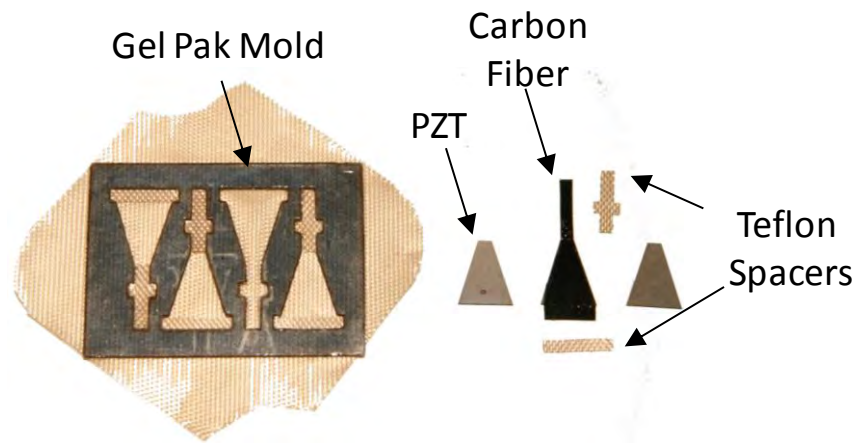


Figure 4.20. Actuator fabrication.

The measured resonant frequency of four actuator designs is given in Table 4.3. In each case, three or four actuators were built in a batch of the same design and tested. The designs are listed chronologically from left to right, and the standard deviation decreased as more fabrication experience was gained. The mean values compare reasonably well with the predictions given in Table 4.2. There can be wide variability in measured actuator resonance as a result of the boundary condition, or clamping mechanism, which is to be expected. For the data shown below, all actuators were fixed similarly by adhering with CA glue to a piece of $\frac{3}{16}'' \times \frac{1}{16}''$ balsa wood, which was then clamped in a vice.

Table 4.3. Actuator resonance measurements.

Actuator Geometry:	2-8-2.7-22.8	3-8-2.7-22.8	4-8-2.7-22.8	3-7.3-2.4-20.4
Specimen 1	418	469	580	603
Specimen 2	490	508	613	631
Specimen 3	459	490	576	654
Specimen 4	526		653	664
MEAN:	473	489	605	638
STD DEV:	45.7	19.4	35.9	27.4
Std Dev %:	9.7	4.0	5.9	4.3

The fully assembled version 4 prototype weighs 750 mg including six wires (three for each actuator). The subsystem mass breakdown is given in Table 4.4. Excluding the wires, which would be absent in a free-flying vehicle, the prototype weighs approximately 560 mg. It is expected that significant weight could be reduced in the fuselage and flapping mechanism, if their designs were structurally optimized. As it is, these subsystems were deliberately over designed to improve robustness of the experimental prototype. Currently, the vehicle powerplant (the actuators) makes up approximately 45% of the vehicle mass, which is in the 20-50% range estimate that insects budget for flight muscle [35:245], though this prototype has no energy source, sensors, payload, or processor. Hopefully, future weight savings in the fuselage and flapping mechanism structure will create room for these components.

Table 4.4. Subsystem mass breakdown.

	Fuselage	Flapping Mechanism	Actuators	Wings	Wires	Total
Mass (mg):	157	125	260	20	188	750

Significant progress has been made in establishing a manufacturing capability at AFIT for insect-sized robotic devices, but clearly some work remains before a prototype is able to lift its own weight. Nevertheless, the devices developed so far are adequate for hardware-in-the-loop bench testing of flapping wing flight control techniques, which will be described in the following chapters. Again, the first step is to verify that such flight-weight structures can be driven with a non-harmonic flapping trajectory near resonance. Chapter 5 will explore this question by describing the efforts to do so. Finally, the complete BABM control technique will be applied to the prototypes in Chapter 6, and the resulting forces and moments measured. The availability of realistic prototypes such as these allow for such hardware testing, which is the most convincing way to demonstrate feasibility of a flapping wing control technique.

5. Open Loop Flapping Wing Trajectory Control

As argued in Chapter 2, the crux of the control problem is coupling a control strategy with a wing flapping mechanism such that the most possible vehicle DOF can be controlled by the simplest possible wing flapping mechanism. In Chapter 4, the design and fabrication of a MAV prototype was described that has a very simple wing flapping mechanism. This mechanism actively controls only one DOF of the wing, wing stroke angle, while allowing for a second passive DOF, wing rotation. The advantage of such a simple mechanism is that it is lighter, more efficient, more durable and more reliable than other, over-actuated systems. The potential disadvantage is that it would inadequately control the vehicle.

At least two control techniques in the literature, those of Deng, et al. and Doman, et al., as well as the BABM technique proposed in Chapter 3 suggest using non-harmonic wing flapping trajectories rather than additional DOF of the wings in order to achieve controllability [23, 24, 28, 29]. The accompanying analysis and simulations have demonstrated that given a few key assumptions, flapping wing control can be achieved by a simple, one or two DOF wing flapping mechanism. The next logical step is to test the assumptions, the first being that flexible MAV wings can be driven in non-harmonic trajectories near resonance.

Deng, et al. addressed this issue by arguing that the MAV's wing flapping system should be designed to have a low quality factor (3 or less), thus reducing the significance of flapping near resonance [23]. Such a design would simplify the problem of non-harmonic flapping near resonance, but would not eliminate it as long as some resonant

behavior was present. Furthermore, for best efficiency, it may be desirable to design the vehicle to have a higher quality factor, as discussed in Chapter 2.

So-called Quasistatic Inertial Piezo Motors use a prismatic piezoelectric device to turn a shaft by following a sawtooth trajectory well below the actuator's resonant frequency [77]. Recently, researchers have demonstrated that a sawtooth-like trajectory can be achieved at resonance by tuning the resonant modes of the actuator to the frequency content of the sawtooth waveform [14]. If similar techniques could be developed for cantilever piezo actuators, then non-harmonic wing flapping near resonance may be possible. The desired non-harmonic trajectory is composed of discrete frequency components. Typically, a resonant system will amplify certain frequency components and attenuate others. For these quasistatic inertial piezo motors, the devices are customized in order to amplify the desired frequency content. For flapping wing trajectories, it would be desirable to do something similar; amplify or otherwise feature the important frequency content in the desired trajectory.

5.1 Frequency Response of MAV Drive Actuator to Non-Harmonic Forcing

Based on the criteria discussed in Chapter 3, the Bi-harmonic Amplitude and Bias Modulation technique is currently the most promising strategy for the control of FWMAVs, assuming a MAV's wings can be forced to flap in the split-cycle fashion. The goal of this chapter is to evaluate this assumption and propose techniques for ensuring the wings track the desired trajectory. Specifically, the frequency response of the wing system to a split-cycle control scheme, which is of critical interest to the MAV design engineer. Clearly, at frequencies well below resonance, the wing flapping mechanism

should track the input well. However, without some compensation, as the drive frequency approaches resonance one would expect the wing to flap in a harmonic motion, or possibly excite higher modes of the structure as a result of the high frequency content in the split-cycle waveform.

This response near resonance is critical if the energetic benefits of resonant flapping discussed in Chapter 2 are to be realized. The motivation for restricting the split-cycle waveform to a constant period is to maintain the wing-beat at a constant frequency so that resonant flapping could be utilized. If, however, the wing system will not track the split-cycle waveform near resonance, then the engineer must either avoid the natural frequency or seek a different control strategy. Considering the already razor thin energy budget for insect-sized MAVs, it would be difficult to argue for avoiding resonant flapping [46]. Therefore, the frequency response of the wing-flapper system to the split-cycle waveform is critical to the utility of the split-cycle control concept.

The experiments consisted of driving a wing flap actuator with the specified split-cycle wing trajectory while measuring the actuator's response. Though the frequency response of the wing will contribute to the total frequency response of the system, the actuator is the most critical because its motion will be amplified through the transmission. Tests were conducted for various combinations of flapping frequency and split-cycle parameter. The split-cycle trajectory was created using a Simulink model. The frequency, frequency shift, and propagation time step was specified by the user. The time step was chosen carefully to be as small as possible so the discrete signal approached a continuous signal yet large enough that the input signal could be generated

in real time. This in effect limited the highest flapping frequency that could be tested.

The system uses a zero-order hold scheme through logical operators so that the frequency and frequency shift do not change within a given wing-beat period. If the operator directs a change within a wing-beat, it will be executed at the start of the next beat. This will also be a requirement of the control scheme.

The Simulink system is converted through Real Time Workshop so that it can be executed by a dSpace system in real time. A GUI created in Control Desk enables adjusting the wing trajectory parameters while the experiment is running. Therefore, the frequency and frequency shift can be changed by the operator in real time just as a control system would. The discrete Simulink output is converted through a digital-analog converter to an analog signal that is amplified to run a bimorph piezo-bender actuator.

The wing motion is measured by a single axis Polytec laser vibrometer which measures the velocity at a point on the wing or actuator, which relates to wing position. For standard sinusoidal forcing, measuring the velocity would be comparable to measuring position, but with the non-sinusoidal forcing used here, position and velocity are not analogous. The velocity function was derived in Chapter 2 and is given in Eqs. 2.25 and 2.26. The differing frequencies for the up and down strokes create a scaling that varies with the frequency shift, δ . This was clearly shown in Figure 2.11. The discontinuity in the acceleration profile suggests that high frequency content will be present in the input that will likely excite the modes of the wing flapping mechanism. The output signal from the laser vibrometer is filtered with a 5kHz low pass filter. The data is captured by Signal

Calc software on a Windows PC. The test rig is shown in Figure 5.1 and a summary of the test equipment is detailed in Table 5.1.

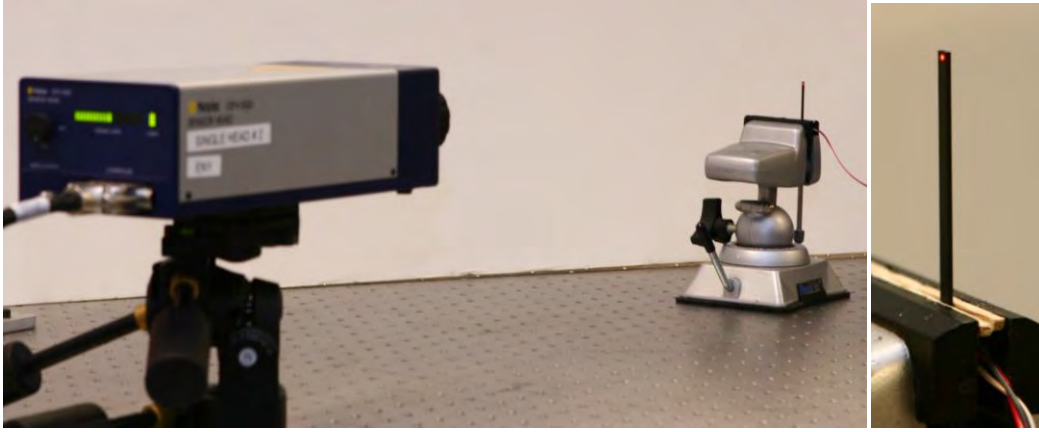


Figure 5.1. Test rigging (only a single piezo actuator is shown for clarity).

Table 5.1. Details of Test Equipment.

Description	Manufacturer	Model	Notes
Signal Generator	D Space	PX10	
Controller Board (D to A converter)	D Space	CP1103	
Quickpack Power Amplifier	Active Control Experts	EL 1224	30x amplification to +/- 30 Volts
Piezo Actuator	Omega Piezo	OPT 39.5/2.1/0.6	Bimorph Cantilever
Laser Vibrometer Sensor Head	Polytec	OFV-505	
Laser Vibrometer Controller	Polytec	OFV-5000/VD-09	Low Pass Filter (5kHz)

Before the split-cycle waveform was tested, system identification of the actuator was performed. The bimorph actuator's first bending mode was at 215 Hz. Data was then collected at frequencies representing a fraction of the first mode (ω_r). The testing program is detailed in Table 5.2 where each independent variable and its range of allowable values are presented. All possible combinations of the various independent variables were tested. Simulation of the split-cycle control scheme by Doman, et al.

showed that adequate control would be possible by limiting the split-cycle parameter to; $-.75 \leq \Delta \leq 0.3$. The response of negative values of the split-cycle parameter exactly mirror the response of positive values, so only the positive values are presented here.

Table 5.2. Testing program.

Frequency	1% ω_r	2.5% ω_r	5% ω_r	10% ω_r	20% ω_r	40% ω_r	80% ω_r	ω_r
Frequency Shifts	0	0.1	0.2	0.3				

Figure 5.2 shows the flapping actuator's response to a split-cycle waveform. At all frequencies, the first mode of 215 Hz is present in the actuator's response. This is likely excited by the piecewise discontinuous nature of the split-cycle waveform. Up to 20% of resonance, the actuator is able to track the general shape of the split-cycle waveform. Beyond that, the first mode begins to dominate as it is more heavily excited. The addition of a wing will add considerable damping that will likely reduce these oscillations, nevertheless, better performance is required if the split-cycle control strategy is to be considered practical. A fourth order Butterworth filter was added to the split-cycle input in the hopes of reducing this oscillation. Results of these tests are shown in Figure 5.3 and Figure 5.4.

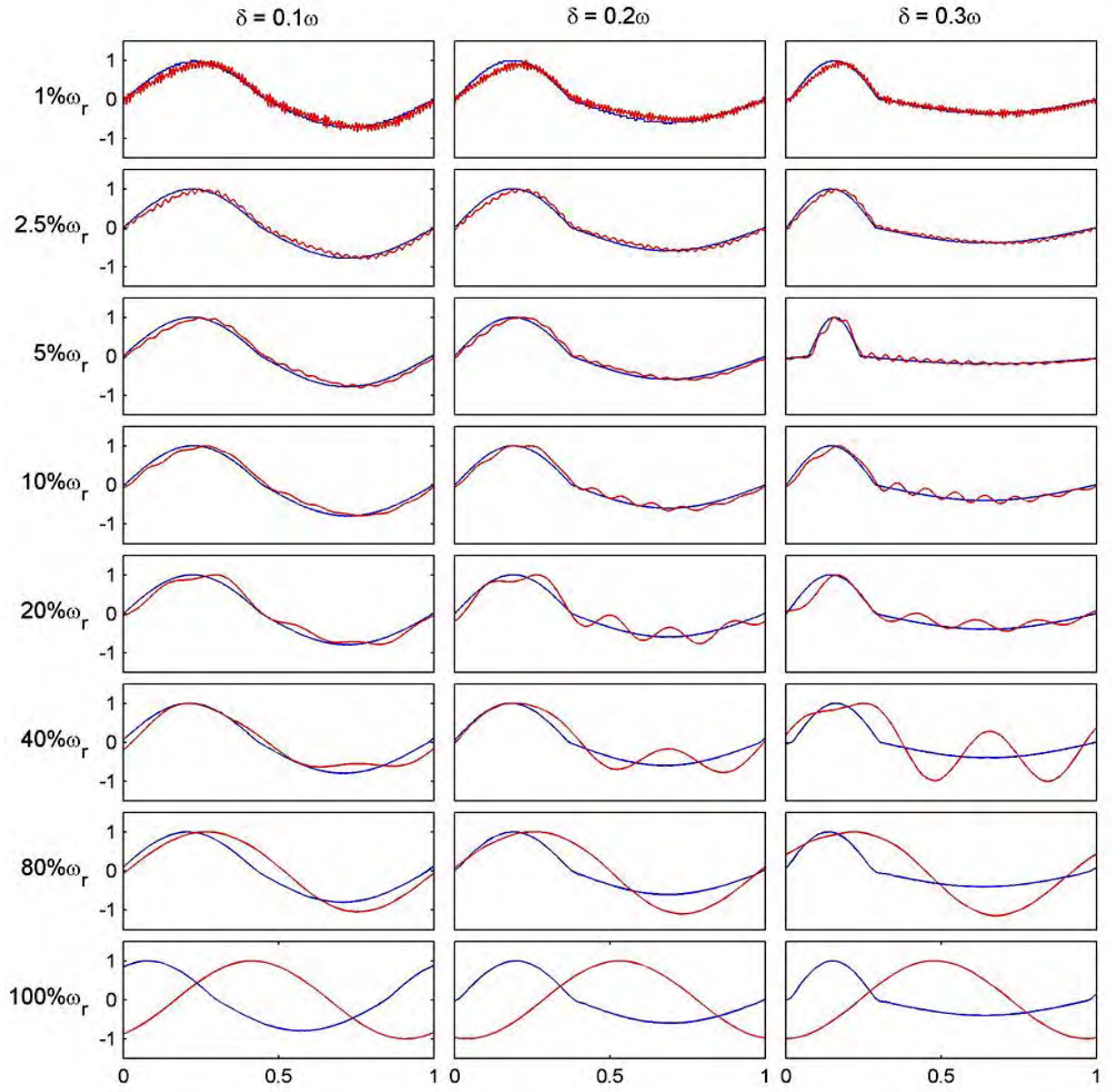


Figure 5.2. Normalized actuator response to split-cycle input; measured velocity is in red, the desired velocity is in blue.

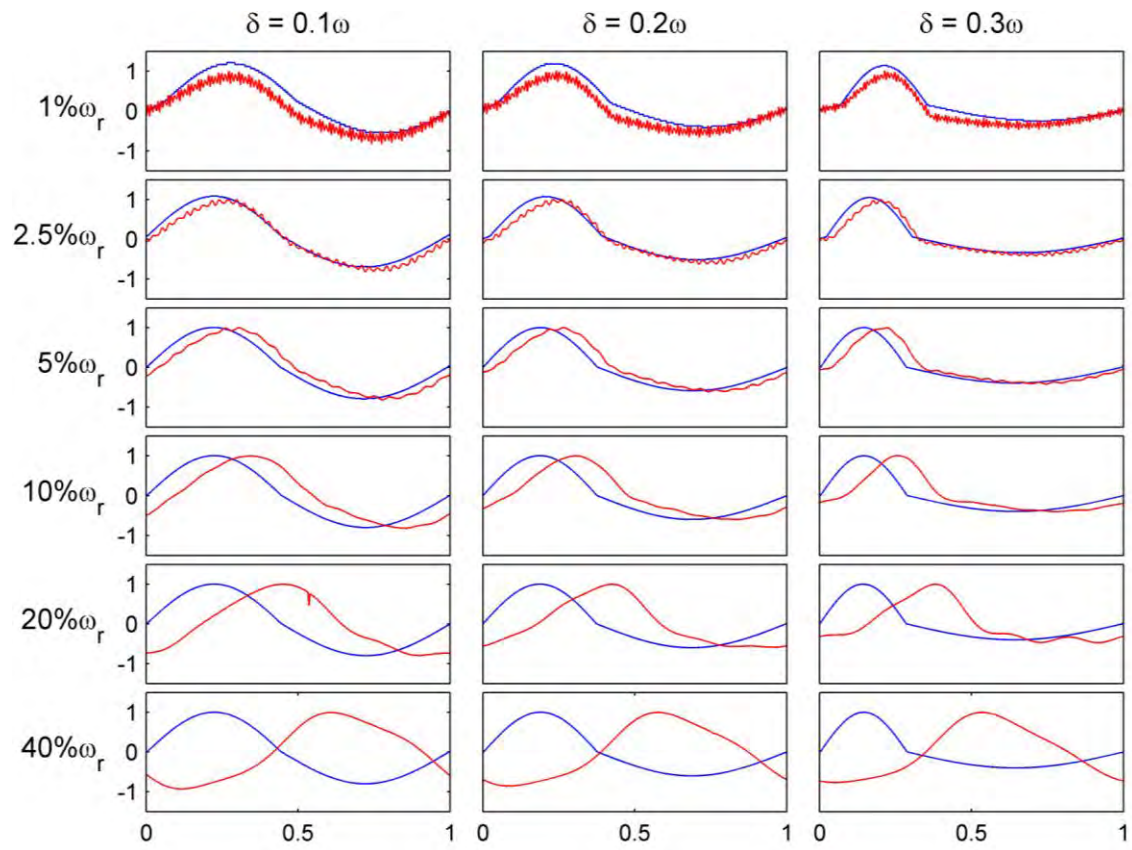


Figure 5.3. Actuator's response to filtered split-cycle input with 100 Hz cutoff frequency.

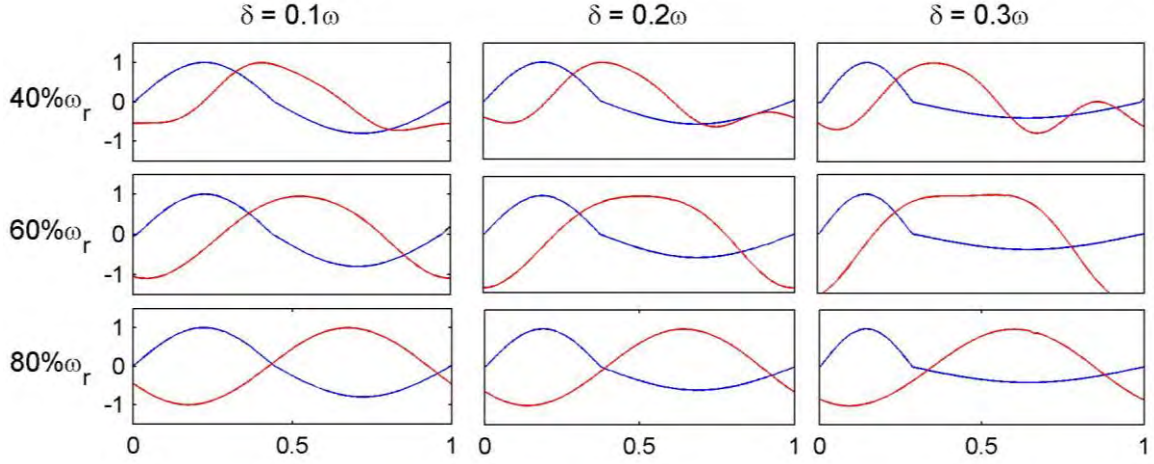


Figure 5.4. Actuator's response to filtered input with 200 Hz cutoff frequency.

The 100 Hz low pass filter reduced the 1st mode oscillations especially at 5%, 10% and 20% of ω_r (corresponding to 10 Hz, 21 Hz and 42 Hz). At 40% ω_r , the filter is attenuating the high frequency content that creates the split-cycle waveform, so the response does not resemble the desired trajectory. A higher cutoff frequency of 200 Hz is shown in Figure 5.4. Again, though the 1st mode oscillations are reduced by the filter, the split-cycle shape is not passed to the actuator. Filtering slightly improved the actuator's ability to track the non-harmonic flapping trajectory as it approached resonance, but the frequency response is still undesirable.

5.2 Discrete Harmonic Plant Compensation

To better understand the actuator's response, a frequency response function (FRF) was created for the actuator. This is shown in Figure 5.5. The data was collected by Signal Calc, which is a virtual signal analyzer on a PC. The measured data is shown alongside a mathematical 4th-order model matched to the data with an Eigenstructure

Realization Algorithm (ERA) [97].

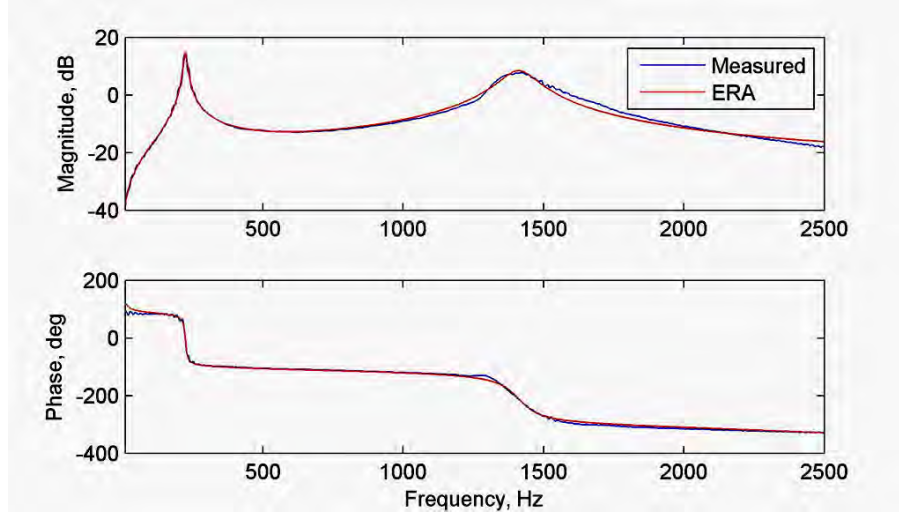


Figure 5.5. Velocity frequency response function of the wing flap actuator.

Because the laser vibrometer measures linear velocity of a point on the actuator, this transfer function represents the ratio of measured velocity to commanded position. To obtain a transfer function relating measured position to commanded position, an integration is performed during the ERA process. The resulting 4th order transfer function is:

$$\frac{x(s)}{V(s)} = \frac{0.0026(s - 1.41 \times 10^5)(s + 4.55 \times 10^4)(s + 4031)(s - 3706)}{(s^2 + 64s + 2 \times 10^6)(s^2 + 726s + 7.9 \times 10^7)} \quad (5.1)$$

The FRF has a standard lightly damped response. The first mode has a high quality factor, so flapping at this frequency would yield a large displacement relative to the energy expenditure. This explains why the first mode is evident in all the results shown in Figure 5.2, as any excitation at that frequency is amplified by at least an order

of magnitude. However, when a wing and linkage are added to the system, aerodynamic drag is expected to damp this response significantly while reducing the first mode frequency. This should reduce the energetic benefits of flapping at resonance while reducing the challenge of non-harmonic wing flapping. Nevertheless, some resonant behavior is expected to survive the addition of wings, as was the case with the Berkeley MFI, so techniques for non-harmonic wing flapping near resonance will still be necessary [11].

In addition to the actuator frequency response, it is necessary to understand the frequency content of the split-cycle waveform. This can be determined through the well known Fourier series approximation:

$$F(t) = \frac{a_0}{2} + \sum_{n=1}^{\infty} a_n \cos \omega n t + b_n \sin \omega n t \quad (5.2)$$

where $F(t)$ is any periodic function and,

$$a_0 = \frac{1}{T} \int_0^T f(t) dt \quad a_n = \frac{2}{T} \int_0^T f(t) \cos \omega n t dt \quad b_n = \frac{2}{T} \int_0^T f(t) \sin \omega n t dt \quad (5.3)$$

These terms can be derived by splitting the wing-beat period into upstroke and down-stroke pieces. Beginning with a_0 and considering ω in Hz:

$$a_0 = \frac{\omega}{2\pi} \left\{ \int_0^{\frac{\pi}{\omega-\delta}} \varphi_u(t) dt + \int_{\frac{\pi}{\omega-\delta}}^{\frac{2\pi}{\omega}} \varphi_d(t) dt \right\} \quad (5.4)$$

$$a_0 = \frac{\omega}{2\pi} \left\{ \int_0^{\frac{\pi}{\omega-\delta}} \cos[(\omega-\delta)t] dt + \int_{\frac{\pi}{\omega-\delta}}^{\frac{2\pi}{\omega}} \cos[(\omega+\sigma)t + \xi] dt \right\} \quad (5.5)$$

$$a_0 = \frac{\omega}{2\pi} \left\{ \left[\frac{1}{\omega-\delta} \sin[(\omega-\delta)t] \right]_0^{\frac{\pi}{\omega-\delta}} + \left[\frac{1}{\omega+\sigma} \sin[(\omega+\sigma)t + \xi] \right]_{\frac{\pi}{\omega-\delta}}^{\frac{2\pi}{\omega}} \right\} = 0 \quad (5.6)$$

Let $N = \omega n$, then the a_n coefficients are:

$$a_n = \frac{\omega}{\pi} \int_0^{\frac{\pi}{\omega-\delta}} \varphi_u(t) \cos Nt dt + \int_{\frac{\pi}{\omega-\delta}}^{\frac{2\pi}{\omega}} \varphi_d(t) \cos Nt dt \quad (5.7)$$

$$a_n = \frac{\omega}{\pi} \int_0^{\frac{\pi}{\omega-\delta}} \cos(\omega-\delta)t \cos Nt dt + \int_{\frac{\pi}{\omega-\delta}}^{\frac{2\pi}{\omega}} \cos[(\omega+\sigma)t + \xi] \cos Nt dt \quad (5.8)$$

Note the identity:

$$\int \cos mx \cos nx dx = \frac{\sin(m-n)x}{2(m-n)} + \frac{\sin(m+n)x}{2(m+n)} \quad (5.9)$$

Continuing with a_n :

$$a_n = \frac{\omega}{\pi} \left[\left[\frac{\sin(\omega-\delta-N)t}{2(\omega-\delta-N)} + \frac{\sin(\omega-\delta+N)t}{2(\omega-\delta+N)} \right]_0^{\frac{\pi}{\omega-\delta}} + \left[\frac{\sin[(\omega+\sigma)t + \xi - Nt]}{2(\omega+\sigma-N)} + \frac{\sin[(\omega+\sigma)t + \xi + Nt]}{2(\omega+\sigma+N)} \right]_{\frac{\pi}{\omega-\delta}}^{\frac{2\pi}{\omega}} \right] \quad (5.10)$$

Substituting the limits of integration:

$$\begin{aligned}
a_n = \frac{\omega}{2\pi} & \left[\frac{\sin\left(\frac{\pi(\omega - \delta - N)}{\omega - \delta}\right)}{\omega - \delta - N} + \frac{\sin\left(\frac{\pi(\omega - \delta + N)}{\omega - \delta}\right)}{\omega - \delta + N} + \right. \\
& \frac{\sin\left(\frac{2\pi(\omega + \sigma - N)}{\omega} + \xi\right)}{\omega + \sigma - N} + \frac{\sin\left(\frac{2\pi(\omega + \sigma + N)}{\omega} + \xi\right)}{\omega + \sigma + N} - \\
& \left. \frac{\sin\left(\frac{\pi(\omega + \sigma - N)}{\omega - \delta} + \xi\right)}{\omega + \sigma - N} - \frac{\sin\left(\frac{\pi(\omega + \sigma + N)}{\omega - \delta} + \xi\right)}{\omega + \sigma + N} \right] \quad (5.11)
\end{aligned}$$

The two middle terms evaluate to zero, giving:

$$\begin{aligned}
a_n = \frac{\omega}{2\pi} & \left[\frac{\sin\left(\frac{\pi(\omega - \delta - N)}{\omega - \delta}\right)}{\omega - \delta - N} + \frac{\sin\left(\frac{\pi(\omega - \delta + N)}{\omega - \delta}\right)}{\omega - \delta + N} - \right. \\
& \left. \frac{\sin\left(\frac{\pi(\omega + \sigma - N)}{\omega - \delta} + \xi\right)}{\omega + \sigma - N} - \frac{\sin\left(\frac{\pi(\omega + \sigma + N)}{\omega - \delta} + \xi\right)}{\omega + \sigma + N} \right] \quad (5.12)
\end{aligned}$$

The derivation for b_n is similar, the result is:

$$b_n = \frac{\omega}{2\pi} \left[\frac{\cos\left(\frac{\pi(\omega - \delta - N)}{\omega - \delta}\right) - 1}{\omega - \delta - N} - \frac{\cos\left(\frac{\pi(\omega - \delta + N)}{\omega - \delta}\right) - 1}{\omega - \delta + N} - \frac{\cos\left(\frac{\pi(\omega + \sigma - N)}{\omega - \delta} + \xi\right) - 1}{\omega + \sigma - N} + \frac{\cos\left(\frac{\pi(\omega + \sigma + N)}{\omega - \delta} + \xi\right) - 1}{\omega + \sigma + N} \right] \quad (5.13)$$

where $N = \omega_n$. Recalling Eq. 2.24 and substituting $\Delta = \delta/\omega$ and $\Sigma = \sigma/\omega$, then,

$\sigma = \frac{\delta\omega}{\omega - 2\delta} = \omega \frac{\Delta}{1 - 2\Delta}$, and $\xi = -\frac{2\pi\delta}{\omega - 2\delta} = -\frac{2\pi\Delta}{1 - 2\Delta}$, then:

$$a_n = \frac{1}{2\pi} \left[\frac{\sin\left(\frac{\pi(1 - \Delta - n)}{1 - \Delta}\right)}{1 - \Delta - n} + \frac{\sin\left(\frac{\pi(1 - \Delta + n)}{1 - \Delta}\right)}{1 - \Delta + n} - \frac{\sin\left(\frac{\pi(1 + \Sigma - n)}{1 - \Delta} + \xi\right)}{1 + \Sigma - n} - \frac{\sin\left(\frac{\pi(1 + \Sigma + n)}{1 - \Delta} + \xi\right)}{1 + \Sigma + n} \right] \quad (5.14)$$

$$b_n = \frac{1}{2\pi} \left[\frac{\cos\left(\frac{\pi(1 - \Delta - n)}{1 - \Delta}\right) - 1}{1 - \Delta - n} - \frac{\cos\left(\frac{\pi(1 - \Delta + n)}{1 - \Delta}\right) - 1}{1 - \Delta + n} - \frac{\cos\left(\frac{\pi(1 + \Sigma - n)}{1 - \Delta} + \xi\right) - 1}{1 + \Sigma - n} + \frac{\cos\left(\frac{\pi(1 + \Sigma + n)}{1 - \Delta} + \xi\right) - 1}{1 + \Sigma + n} \right] \quad (5.15)$$

It is clear that the split-cycle waveform shape is purely a function of Δ , the split-cycle parameter as a fraction of frequency. Note that these terms are singular when any one of the denominators equal zero, which occurs for certain combinations of Δ and n , specifically when:

$$\Delta = 1 - n, \quad \Delta = 1 + n, \quad \Delta = \frac{n-1}{2n-1}, \quad \text{or} \quad \Delta = \frac{n+1}{2n+1}$$

The first case occurs when $\Delta = 0, -1, -2$, etc. The second case is not possible given the limitation that $\Delta < 0.5$. The third case occurs when $\Delta = 1/3, 2/5, 3/7$, etc, and the fourth case occurs when $\Delta = 2/3, 3/5, 4/7$, approaching $1/2$ as $n \rightarrow \infty$. As noted previously, adequate control may be possible by limiting Δ to: $-0.75 < \Delta < 0.3$. If that is the case, then the only singularity occurs for $\Delta = 0$, which is a standard cosine trajectory.

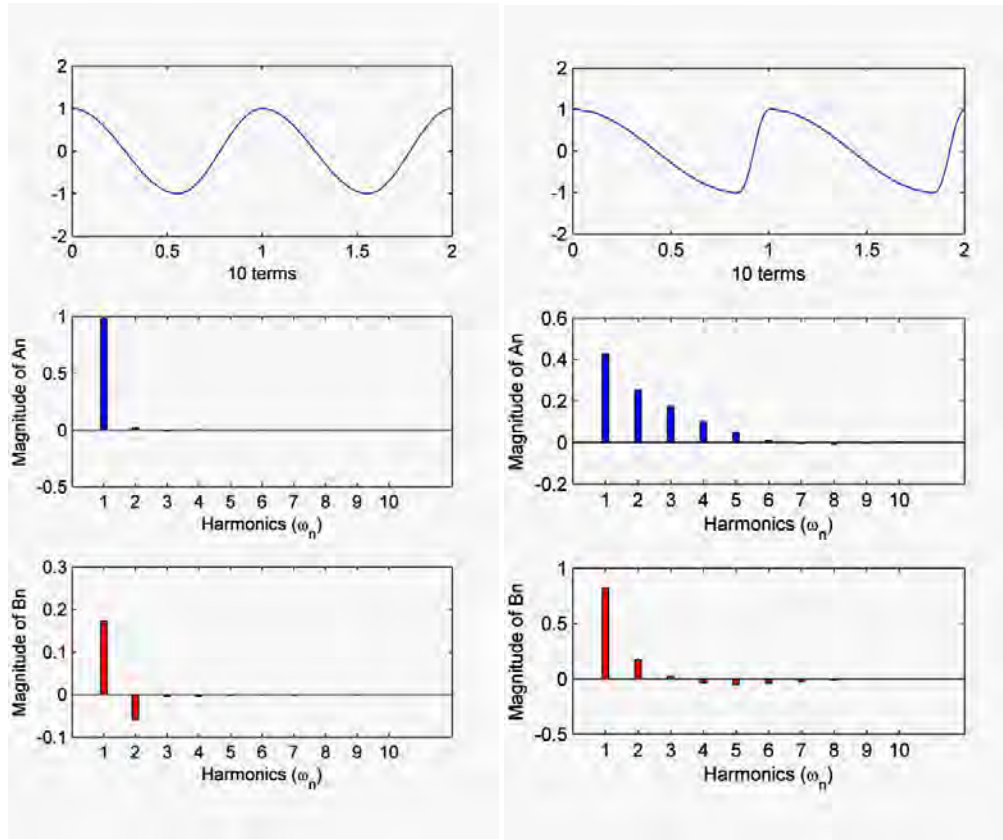


Figure 5.6. Truncated Fourier series representation of the split-cycle waveform. On the left,

$\Delta = 0.1$, on the right $\Delta = 0.4$.

The frequency content can now be inspected, as shown in Figure 5.6. Two split-cycle waveforms are approximated with a 10-term truncated Fourier series shown with their frequency spectrums. As expected, the greater the split-cycle parameter, Δ , the greater the magnitudes of the higher harmonics. The exact relationship between Fourier coefficients and split-cycle parameter for a range of values is shown in Figure 5.7. As noted above, the split-cycle parameter may be limited to; $-0.75 \leq \Delta \leq 0.3$. Where the split-cycle parameter of 0.3 creates a mirror image waveform to that created with a split-cycle parameter of -0.75, though this is not clear in the form of the split-cycle parameter.

Instead of plotting the coefficients against the split-cycle parameter, which would create an asymmetric and confusing plot, they are plotted against the deviation from the nominal period, which is:

$$\tau = \frac{\Delta}{2(1-\Delta)} \quad (5.16)$$

This represents the fraction of the total period $\left(\frac{2\pi}{\omega}\right)$ that the upstroke deviates from zero.

Additionally, a plot showing the phasor form magnitude and phase shifts is given in

Figure 5.8.

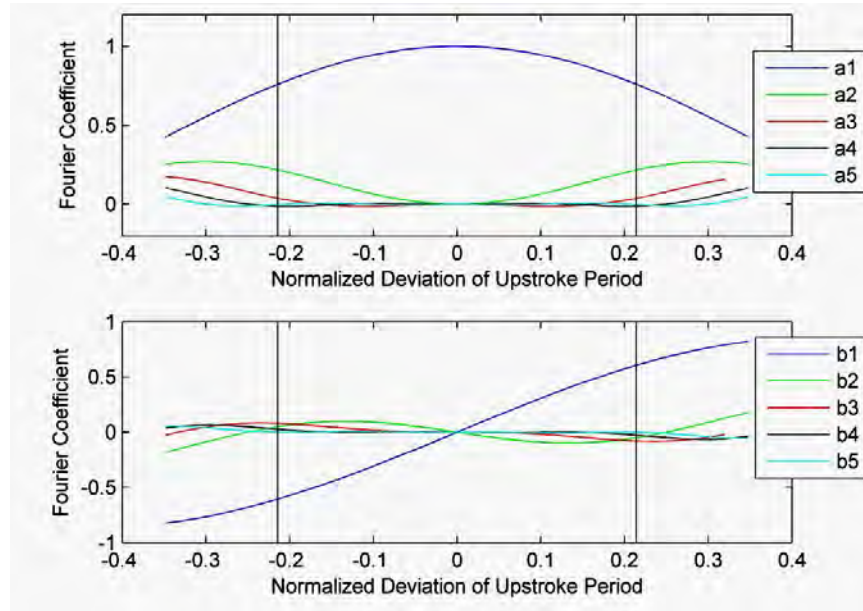


Figure 5.7. Fourier coefficients as a function of split-cycle parameter, Δ . The vertical lines (± 0.21) represent the proposed bounds on Δ .

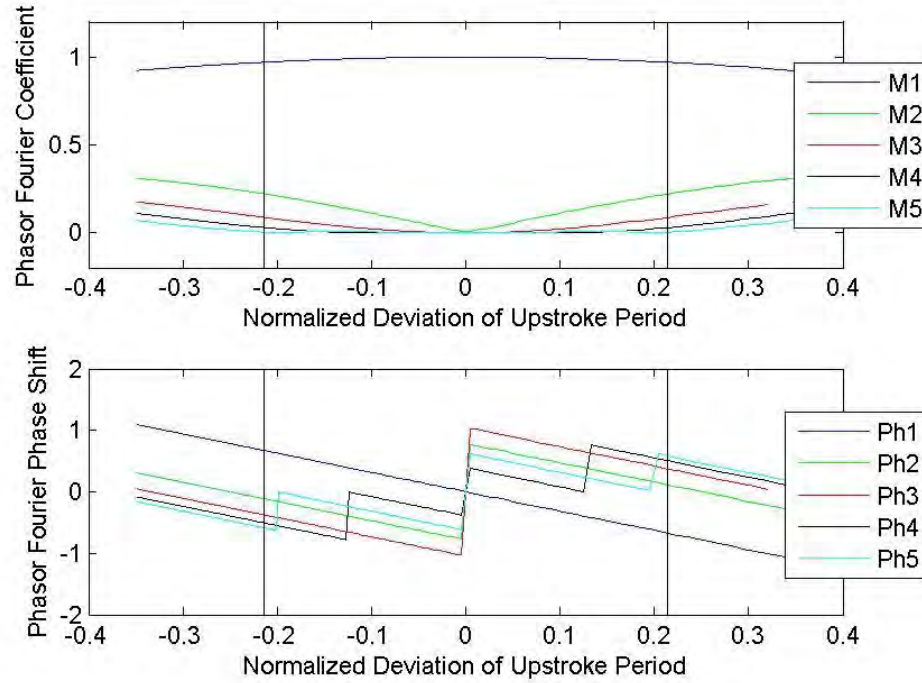


Figure 5.8. Phasor form Fourier coefficients as a function of split-cycle parameter, Δ .

Note, each phase term has been normalized to the frequency of the 1st harmonic by dividing it by its harmonic number.

Inspection of Figure 5.7 and Figure 5.8 reveals that for values of Δ within the proposed bounds, the 5th, 4th, and even 3rd Fourier coefficients are of little significance. This suggests that a two or three term truncated Fourier sum might adequately represent the split-cycle waveform. Figure 5.9 compares various n -term Fourier sum representations of the split-cycle waveform for $\Delta = 0.3$, the maximum proposed waveform shift. The two- and three-term sums closely replicated the split-cycle waveform.

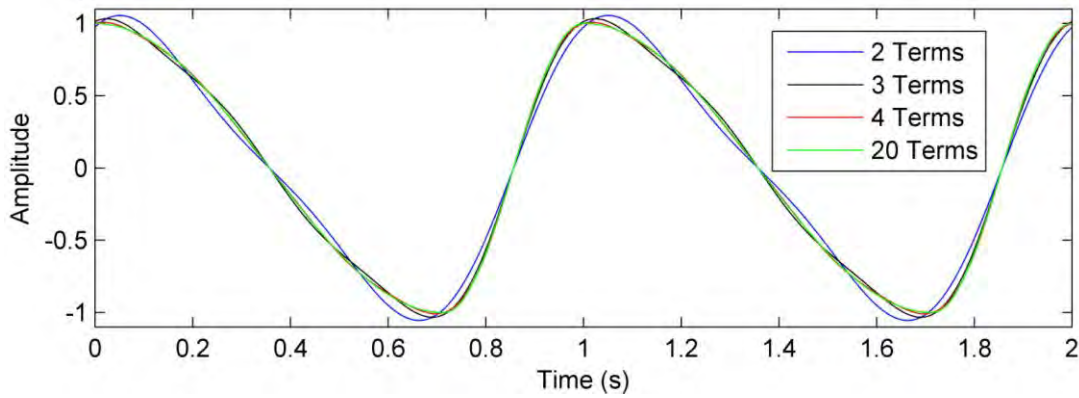


Figure 5.9. Comparison of truncated Fourier sum representations of a split-cycle waveform for $\Delta = 0.3$.

Given the analytic actuator model from the ERA procedure (such as Eq. 5.1), it might be possible to compensate for the actuator dynamics and generate the desired wing trajectory. Typically, this would proceed by attempting to invert the plant, or otherwise obscure its dynamics. This would require at least four additional states for the plant inversion, and likely four more for the filters that would be required to stabilize the now unstable plant model. An insect-sized MAV will have a limited weight and energy budget for control. One can assume that processing speed will be very limited, so complex controllers that require fast computations should be avoided. Considering this, another approach is proposed here.

Because the split-cycle waveform can be easily and adequately replicated with only two or three harmonics, compensation for the actuator dynamics (and later the full wing flapping mechanism dynamics) can be accomplished only at the discrete harmonics present in the waveform. Instead of driving the wings with the piece-wise split-cycle

waveform, the wings should be driven with the continuous truncated Fourier sum. Each term of the Fourier sum can be preconditioned to compensate for the actuator's dynamics at its harmonic frequency which is evident from the actuator transfer function. To accomplish this, the sine and cosine terms of the Fourier sum must be recast in the phasor form as a single cosine with a phase shift:

$$F(t) = \sum_{n=1}^{\infty} a_n \cos \omega n t + b_n \sin \omega n t = \sum_{n=1}^{\infty} M_n \cos(\omega n t + \phi_n) \quad (5.17)$$

where,

$$M_n = \sqrt{a_n^2 + b_n^2} \quad \text{and,} \quad \phi_n = -\tan^{-1}\left(\frac{b_n}{a_n}\right) \quad (5.18)$$

For the prescribed flapping frequency, split-cycle parameter and number of harmonics (k), the k phasor coefficients and phase shifts are computed. Then, the actuator transfer function is evaluated at each harmonic, predicting the amplification and phase shift from the actuator for each harmonic. These values are inverted and applied to the corresponding Fourier term to precondition the input. For example, consider the case of flapping at 80% ω_r driving the actuator with a two term Fourier approximation of a $\Delta = 0.3$ split-cycle waveform. The two harmonics are 172 Hz and 344 Hz. The Fourier coefficients, calculated from Eqs. (5.14) and (5.15) are:

$$a_{172} = 0.759 \quad b_{172} = 0.605 \quad a_{344} = 0.216 \quad b_{344} = -0.049$$

and in phasor form (equation 5.17):

$$M_{172} = 0.971 \quad \phi_{172} = -0.673 \quad M_{344} = 0.222 \quad \phi_{344} = 0.224$$

These harmonics must be preconditioned to account for the actuator dynamics, so the actuator transfer function (Eq. 5.1) is evaluated at 172 Hz and 344 Hz (for this example), yielding:

$$M_{172,act} = 4.24 \quad \phi_{172,act} = -0.100 \quad M_{344,act} = 1.64 \quad \phi_{344,act} = -3.12$$

The preconditioned terms are found by:

$$M_{PC} = \frac{M_{\omega_n}}{M_{\omega_n,act}} = \frac{M_{172}}{M_{172,act}} = \frac{0.971}{4.24} = 0.229 = M_{172,PC} \quad (5.19)$$

$$\phi_{PC} = \phi_{\omega_n} - \phi_{\omega_n,act} = -0.673 - (-0.100) = -0.573 = \phi_{172,PC} \quad (5.20)$$

The input is then created per Eq. 5.18:

$$F(t) = M_{172,PC} \cos[172(2\pi)t + \phi_{172,PC}] + M_{344,PC} \cos[344(2\pi)t + \phi_{344,PC}] \quad (5.21)$$

This open-loop, feed-forward control technique is called Discrete Harmonic Plant Compensation (DHPC) because it amplifies or attenuates the key frequency components of the desired trajectory as needed to compensate for the system dynamics. A Simulink model was created to implement this control in real time with a time step of 0.0001. This technique vastly improved the actuator's ability to track the non-harmonic wing flapping trajectory, as shown in Figure 5.10 and Figure 5.11. In fact, with this technique, it is possible to achieve a non-harmonic wing flapping trajectory while flapping at resonance, which is the desired result.

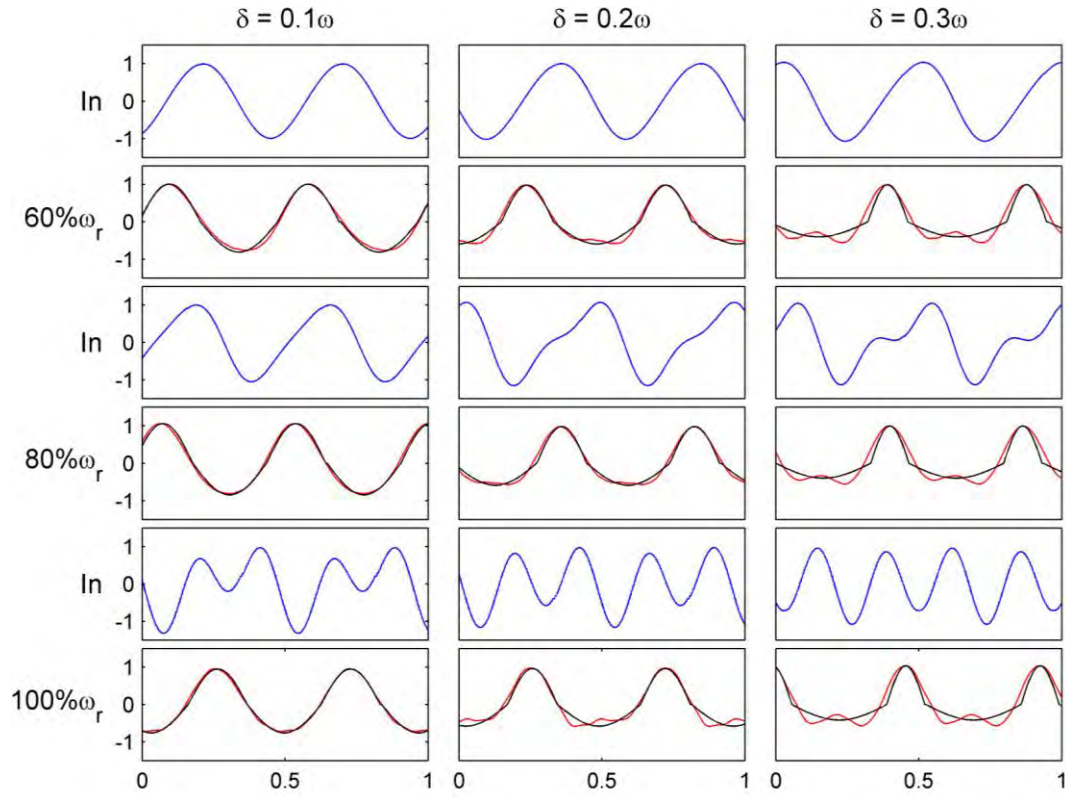


Figure 5.10. Actuator's response to the preconditioned 2-term Fourier waveform. The blue plots represent the preconditioned drive signal, the red lines are the measured actuator trajectory, the black lines represent the “desired” split-cycle trajectory.

As implemented, this waveform generator was barely able to perform the computations in real time. In fact, when the three-term Fourier sum was implemented, the additional computational requirement of the third term forced a doubling of the simulation time step. This is evident in the 100% ω_r plots of Figure 5.11 where digitization of the drive signal is visible. The computations can be streamlined by replacing the exact equations for the Fourier coefficients with low-order curve fits or

look-up tables.

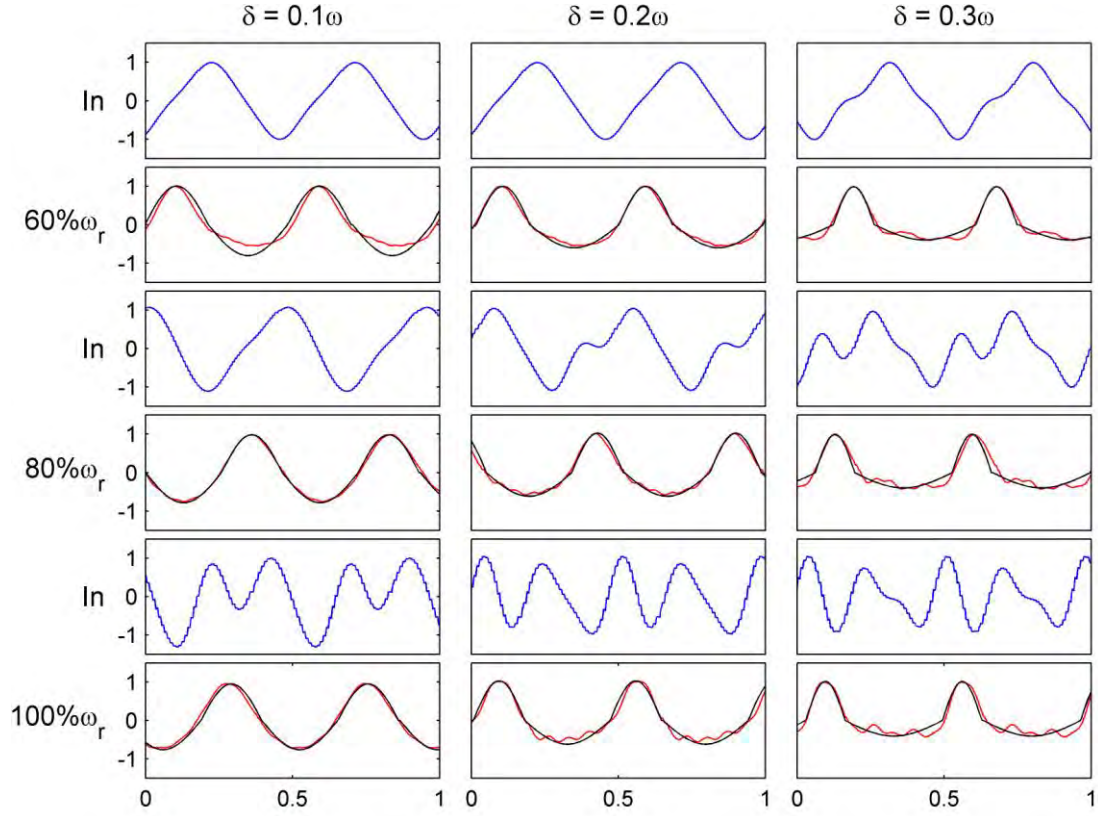


Figure 5.11. Actuator's response to the preconditioned 3-term Fourier waveform.

The following curve fits were chosen to represent the phasor coefficients for the BABM trajectory:

$$M_1(\tau) = \cos(2\tau) \quad (5.22)$$

$$M_2(\tau) = 0.34 \sin(3.3\tau) \quad (5.23)$$

$$\beta_1(\tau) = -2\tau \quad (5.24)$$

$$\beta_2(\tau) = -4\tau + \frac{\pi}{2} \quad (5.25)$$

where τ is defined in Eq. 5.16. Note the second phase term, β_2 , is simply twice β_1 with a phase shift. Therefore, the phasor form Fourier sum (Eq. 5.17), can be simplified slightly by substituting β_1 for β_2 :

$$F(t) = M_1 \cos[\omega t + \beta_1] + M_2 \cos\left[2\omega t + 2\beta_1 + \frac{\pi}{2}\right] = \quad (5.26)$$

$$M_1 \cos[\omega t + \beta_1] - M_2 \sin[2\omega t + 2\beta_1]$$

This is the core of the BABM trajectory. The complete trajectory (Eq. 3.52) is wrapped with a total amplitude term (A) and has a bias added (η). This wing trajectory is ideal for implementation on a flight weight MAV because it is continuous, and it uses simple arithmetic. The harmonic coefficients are simple linear and trigonometric functions which will be easier to handle with the limited processing power expected to be available on such a vehicle.

5.3 Resonant Non-harmonic Wing Flapping

Based on the above results, it is clear that a bimorph PZT actuator can be driven to flap in the desired non-harmonic fashion near resonance. The next step is to demonstrate that an entire wing flapping mechanism can do the same. As no suitable mechanisms are available for testing, one was designed and built, as detailed in Chapter 4. The planned bench testing does not require that the mechanism be capable of flight, but to increase the credibility of the results, efforts were made to come as close to a

flight-worthy mechanism as allowed by our manufacturing capability. The mechanism was built to full scale and designed as if it were going to be attached to a flight vehicle.

The completed system was characterized with the laser vibrometer, and its FRF is shown in Figure 5.12. The 1st mode occurs in the desired range at 27 Hz, and is damped significantly compared to the bare actuator. In general, this will improve its response to non-harmonic forcing because the amplifications or attenuations occurring at each harmonic are relatively similar. However, there is an anti-resonance at 75 Hz that must be avoided.

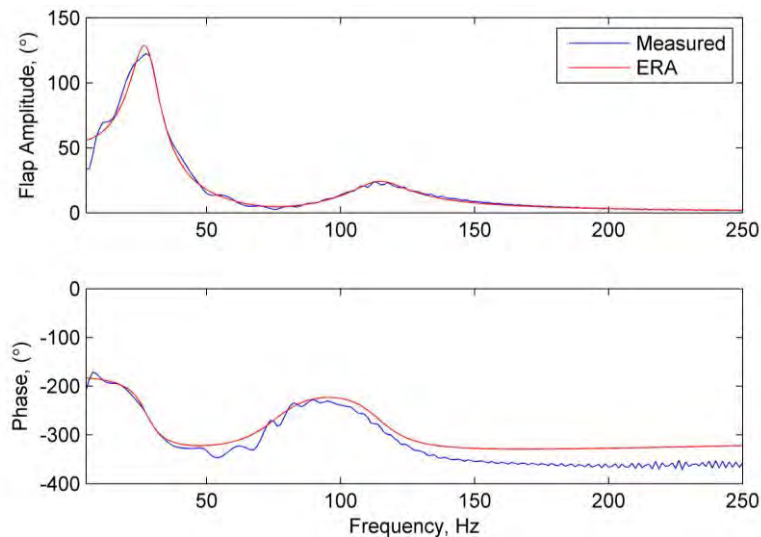


Figure 5.12. Frequency Response Function of the complete wing flapping mechanism.

A system transfer function was obtained using the ERA as described for the bare actuator. A four-state approximation of the wing flapping mechanism is:

$$\frac{x(s)}{V(s)} = \frac{-8.32e^{-3}(s^2 + 155s + 2.4e^5)(s^2 + 7964s + 1.99e^7)}{(s^2 + 66s + 3.1e^4)(s^2 + 137s + 5.2e^5)} \quad (5.27)$$

This transfer function predicts the linear displacement measured by the laser at a point on the wing for a given actuator voltage. This point is along the leading edge, 4mm from the wing root, and the wing is assumed to be a rigid body. This assumption was verified by observing the wing flapping with a strobe to stop the wing motion. A photograph of this is shown in Figure 5.13.

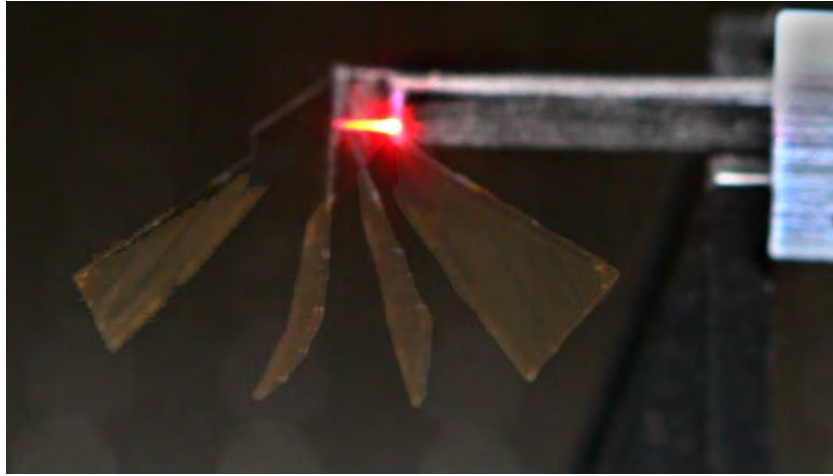


Figure 5.13. Rigid body wing motion, visualized with a strobe lamp.

Given the system model from the ERA procedure, the DHPC open-loop control was implemented in the Simulink code, and the wing flapping mechanism was driven with a variety of bi-harmonic waveforms with varying split-cycle parameter and flapping amplitude. The results are plotted in Figure 5.14. The open-loop voltage applied to the actuator is plotted in blue, the desired split-cycle trajectory is plotted in black and the measured wing velocity is in red. The plots are arranged in three columns of increasing

flapping amplitude (% of maximum) and four rows of increasing split-cycle parameter. The wing motion was captured by the laser vibrometer measuring the linear motion of a point on the leading edge 4mm from the wing root. The angular velocity of the wing in rad/s is extrapolated by assuming rigid body motion of the wing.

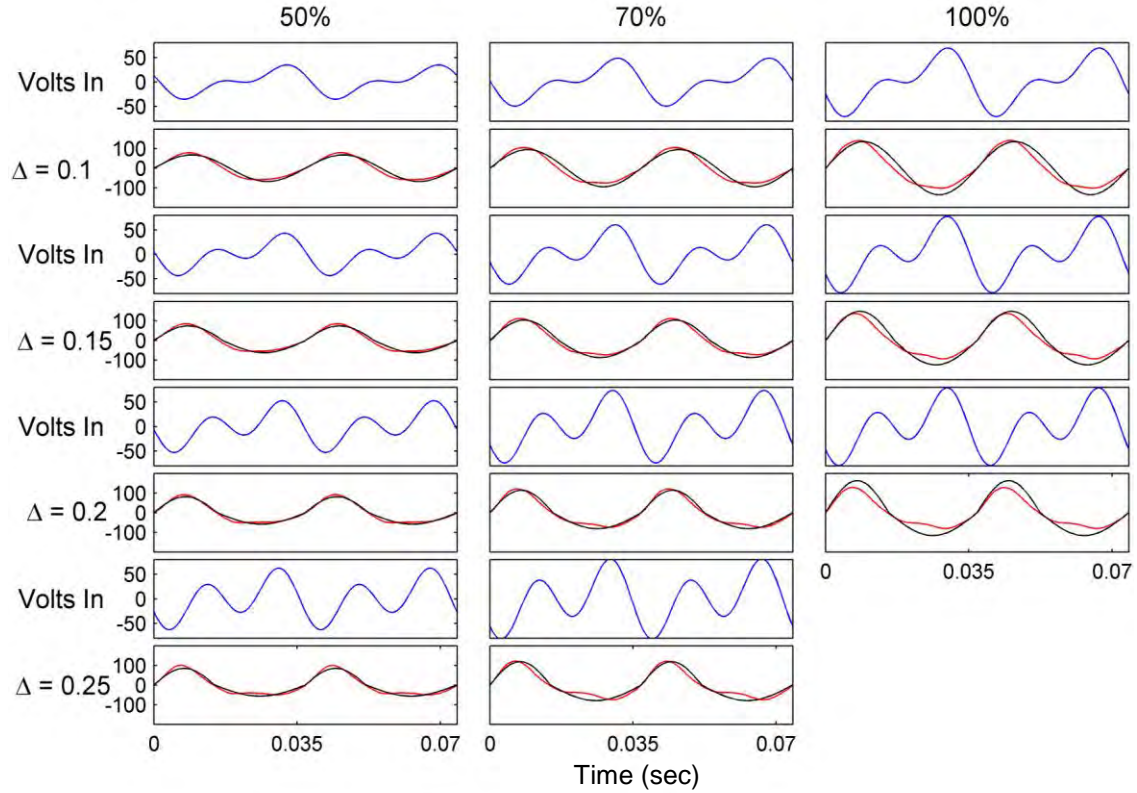


Figure 5.14. Wing response to the bi-harmonic waveform with DHPC.

In general, the wing successfully demonstrated the desired split-cycle behavior, as well as amplitude and bias modulation, even for large values of the split-cycle parameters up to $\Delta = 0.25$. This performance can be improved however. For several cases, it appears that the phase shift of the bi-harmonic drive signal is slightly off. For

example, in the plot for $\Delta = 0.2$ at 100%, there are two local minima that should be the same level. This can be traced to the transfer function given in Figure 5.12, where there are several ripples near the second harmonic of 54 Hz that are likely the modes of higher-frequency vibrational modes in the wing. These features are not captured by the four-state ERA model of the system, resulting in a difference in phase up to 50° , which is more than enough to account for the slightly uneven wing response. As manufacturing techniques improve, and extraneous DOF of the wing are eliminated³, the FRF should become smoother, making a better low-order ERA fit possible. On the other hand, only a narrow range of frequencies are expected to be utilized by the MAV, so a continuous system model applicable to any frequency is not entirely necessary. Instead, a look-up table could be used in the future that covers the frequency band of interest and to ensure a better match to the FRF.

Another notable result is the saturation of the split-cycle trajectory as the flapping amplitude and Δ increase. Consider the plots in positions (4,3), (6,3), and (8,2) in Figure 5.14. For these cases, the wing was not able to obtain the desired flapping amplitudes because the voltage limit on the actuator had been reached. The drive actuator is rated to ± 75 volts, so this voltage was not exceeded during testing. As Δ was increased, it was necessary to use a larger drive voltage to obtain the non-harmonic wing trajectory as the higher harmonic needed more amplification. This is the cost of control for this DOF. For a sufficiently large actuator, this may not be a problem, other than the increased energy requirements. For the actuator used in this experiment, it limited the

³ Extraneous DOF are both higher order structural modes and low frequency modes resulting from slip or imprecise mechanical interfaces. Improved manufacturing should eliminate these low frequency modes.

flapping amplitude that could be achieved at the higher values of Δ . This problem may be reduced slightly by improving the aforementioned phase problem. Using the correct phase shift may reduce instances of having both harmonics be at a peak value when they are summed. Nevertheless, these experiments verify a previously assumed requirement of flapping wing control: If the flapping wings are to be used for vehicle control, their actuators will need excess power to generate control forces, and thus must be sized larger than would otherwise be necessary to simply flap with simple harmonic motion.

Recall in Section 3.3, three key assumptions were identified that were used in the analysis to show that 5 DOF control of a FWMAV was possible with only two actuators. They were: The wings can be flapped with non-harmonic trajectories at resonance, the blade-element analysis adequately predicts the aerodynamic wrench on the MAV, and the quasi-static assumption that only the cycle-averaged (not instantaneous) forces and moments effect the vehicle dynamics. The experiments just described demonstrate that the first assumption holds true. Flight-weight insect-sized MAV wings can be flapped non-harmonically at their resonant frequency, given appropriate control. In this case, a novel open-loop control technique, Discrete Harmonic Plant Compensation, was used to provide this control. This technique is desirable because it requires minimal computing power, and no active sensing of the wing position. Chapter 6 describes efforts to test the second assumption, that blade-element analysis adequately predicts the aerodynamic wrench on the MAV.

6. Evaluation of BABM for Flapping Wing MAV Control

The overarching hypothesis of this research is that a relatively simple, two actuator MAV can produce forces and moments in 5 DOF sufficient to control the vehicles flight. A novel control technique, Bi-harmonic Amplitude and Bias Modulation (BABM), has been proposed and analyzed, demonstrating that this technique can generate the desired forces and moments, given key assumptions [5]. The first is that the thin, flexible wings of a FWMAV can be driven with the desired trajectory, especially non-harmonically. Wing flapping mechanisms and MAV prototypes were built to test this assumption, and an open-loop control technique called Discrete Harmonic Plant Compensation (DHPC) was developed that demonstrated such wing kinematics were achievable for a flight-weight vehicle [3, 7]. The next assumption is that the blade-element equations used to predict the body forces and moments generated by these kinematics are sufficiently accurate to form the foundation of a vehicle controller. This assumption will be evaluated here.

Flapping wing flight is highly unsteady due to the periodic wing motion, and no mathematical model exists to capture these unsteady effects, short of direct numerical simulation of the Navier-Stokes equations. Unsteady aerodynamics contributes to the forces generated by the wings, but how much, and in what sense is not known for all possible flight conditions. Therefore, it is possible that a control technique that is successful in a quasi-steady environment may not be when the full physics are included. To definitively evaluate a proposed control technique, it is necessary to test it in the presence of unsteady effects.

Given the high computational cost of CFD methods, the only viable approach to capturing the full aerodynamics at this time is to perform experiments in air. Unfortunately, power and sensing technology are not currently sufficient to allow for fully autonomous free flight of an insect-sized FWMAV, even if we knew how to control it. However, it is still possible to include the necessary physics by mounting a prototype on a 6 component load cell and measuring the forces and moments that the flapping wings generate as a result of the specified kinematics. It would then be possible to determine if the resulting forces and moments were sufficient to control the vehicle, and the MAV's flight could even be simulated in a hardware-in-the-loop experiment. This would provide an essential intermediate testing step between the current simulations and free flight because it eliminates the most tenuous assumptions of previous FWMAV simulations, replacing them with hardware.

6.1 Experiment Equipment and Procedures

The BABM control technique requires a vehicle with the ability to arbitrarily prescribe the wing stroke angle function so that three parameters of the wing stroke can be modulated. Most FWMAV designs use a DC motor to flap the wings which enforces nearly simple harmonic wing motion with a fixed amplitude. Instead, the vehicle proposed for this control technique, and described in Chapter 4 uses a bimorph cantilever piezo actuator to drive the wings, which has the ability to create more elaborate wing trajectories including the ability to modulate amplitude and bias and flap non-harmonically with adequate compensation using DHPC as described in Chapter 5. Two wing flapping mechanisms are assembled in a fuselage/test stand in a mirror-image

arrangement so that symmetric and asymmetric wing stroke kinematics can be tested. The fuselage is designed to create a rigid boundary condition for the actuators and linkages and faithfully transmit forces and moments to the balance.

The purpose of the experiment is to test the validity of the control effectiveness matrix given in Eq. 3.49. Specifically, to show that the control parameters have influence over the DOF that they were predicted to influence, and that there is limited coupling between the control parameters, which would simplify control implementation.

Therefore, the experiment consists of flapping the MAV prototype with varying wing trajectories corresponding to a range of control parameters while measuring the 6 forces and moments generated by those trajectories. The wing kinematics/control parameter combinations that were tested are symmetric amplitude modulation, asymmetric amplitude modulation, symmetric split-cycle, asymmetric split-cycle and symmetric wing stroke bias.

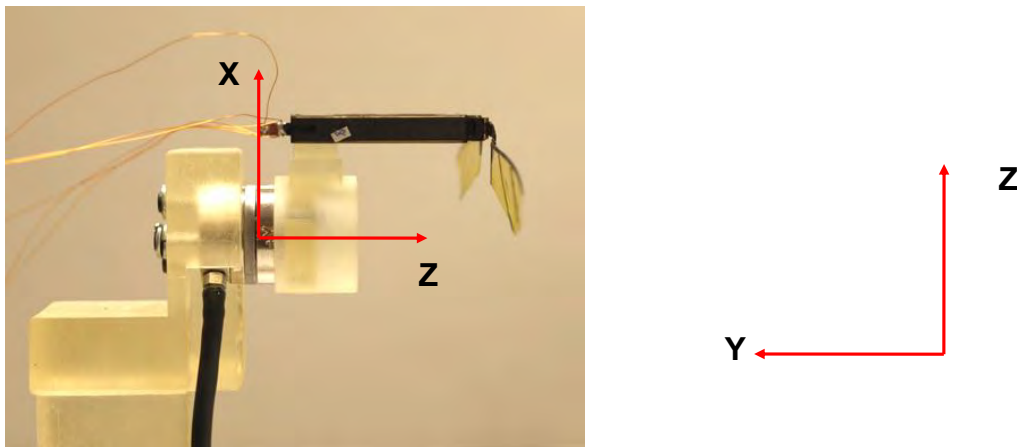


Figure 6.1. Flapping wing MAV prototype and test stand.

The MAV prototype and its mounting arrangement on the force/torque sensor is shown in Figure 6.1. The prototype was tested on an ATI Nano-17 force/torque transducer. This balance has noise on the order of 0.2 mN when unloaded, and is the most sensitive commercially available 6-DOF sensor of which we are aware. The MAV was mounted in a cantilevered position to eliminate wake interaction with the sensor. The data was captured by an ATI “Netbox” and imported into a PC for post-processing. The control parameters are specified to the MAV through a MATLAB Simulink model (Figure 6.2) that constructs the BABM wing trajectory for each wing and applies the appropriate actuator voltages through a dSPACE system. In addition to the standard three control parameters for each wing, an additional gain and DC bias can be applied by this model to compensate for asymmetries between the two wings resulting from manufacturing variability.

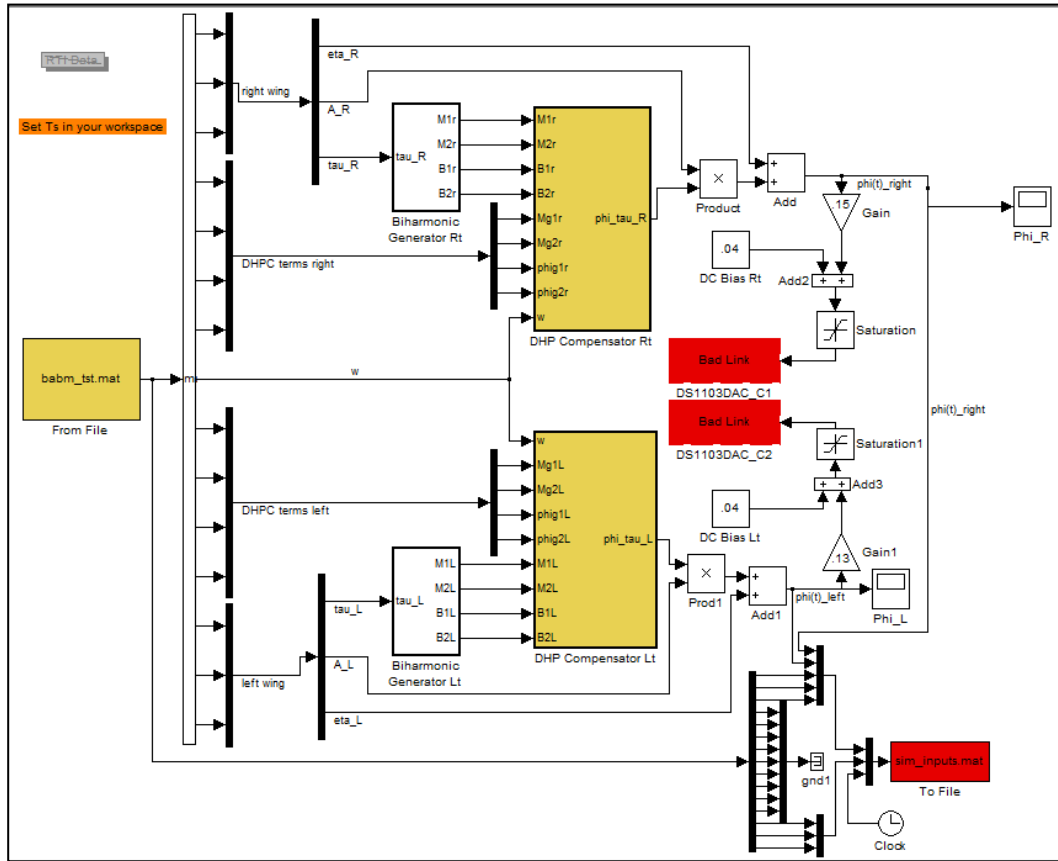


Figure 6.2. Simulink model for generating wing trajectories.

To improve the quality of the data, each parameter was tested individually, with a tare taken between each test point. For example, Figure 6.3 shows the test profile for the asymmetric split-cycle test where data were taken for seven different values of the control parameter, Δ . The top plot gives the commanded wing kinematic parameters (A_R , A_L , Δ_R and Δ_L), the bottom plot is the measured raw data with brackets indicating the range of values used for tares (green) and cycle-averages (red). At each data point the flapping is ramped up from zero to A_0 and the split-cycle parameter is similarly ramped to

the test value. There is a short pause before data is taken to allow transients to settle, then the flapping is ramped back down to zero and another tare is taken before the next test.

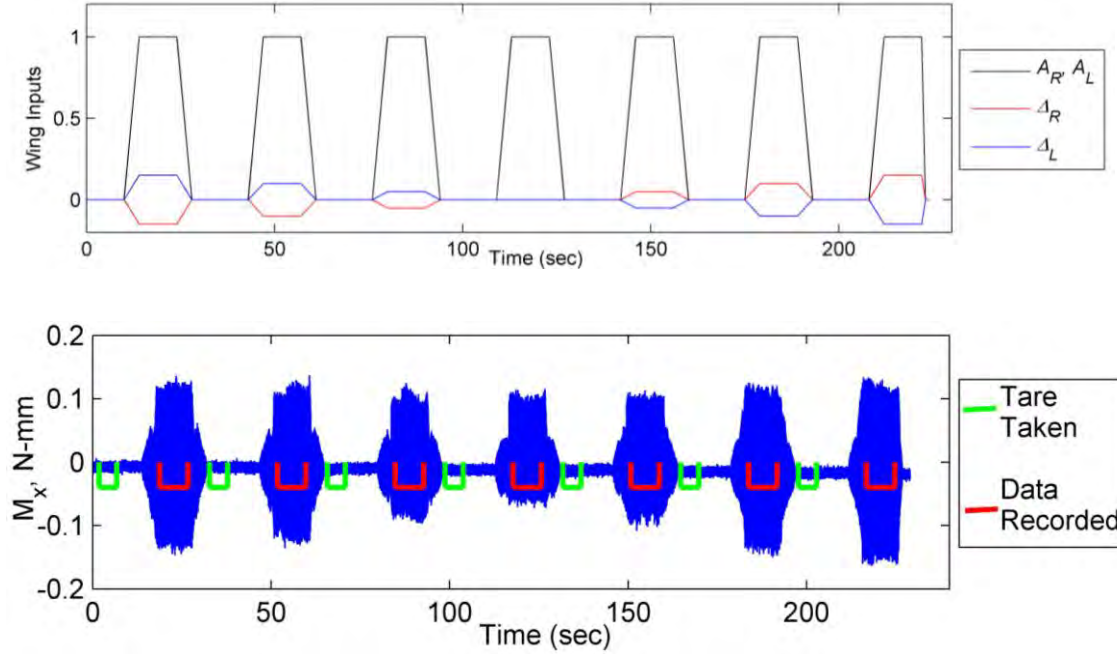


Figure 6.3. Test profile for asymmetric split-cycle test.

The desired time-varying control parameters are specified in an input file that is read by the Simulink model and used to create the wing trajectories. A typical data capture is shown in blue in Figure 6.4, zoomed in to show the time-varying lift. This data was low-pass filtered by the ATI Netbox with a cutoff frequency of 73 Hz, which is one of the available settings. This profile is consistent with similar data in the literature and blade-element predictions indicating lift peaks near mid-stroke and negative lift spikes during wing reversal. Therefore, a four-term harmonic curve fit is overlaid in red. Post-processing consisted of cycle-averaging the force and moment data by averaging the time-varying measured signal over an 8 second period, so for a flapping frequency of 20

Hz, 160 cycles would be averaged to create a single data point. The range of values tested for each kinematic control parameter is given in Table 6.1. A quiescent flow environment was created for the flapping mechanism by encasing the test apparatus in a Plexiglas enclosure.

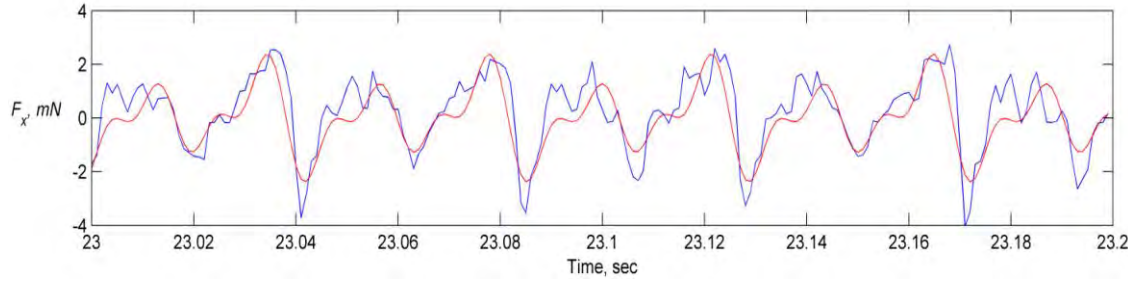


Figure 6.4. Time-varying lift data.

Table 6.1. Kinematic control parameters tested.

Control Parameter	Tested Values						
A	0.85	0.9	0.95	1.0	1.05	1.1	1.15
τ	-0.15	-0.1	-0.05	0	0.05	0.1	0.15

6.2 Preliminary Cycle-Averaged Forces and Moments

The goal of this work is to determine if the control derivatives given in Eq. 3.49 above accurately predict the real physics of a flapping MAV. These were developed from blade element formulas which can predict the instantaneous aerodynamic forces and moments that the flapping wing will generate from a prescribed wing trajectory. However, if these instantaneous predictions were compared to instantaneous measurements, the comparison would be very sensitive to the unsteady effects, which are,

by definition, changing with time, as well as measurement noise. A better approach that mutes the effect of unsteady aerodynamics and noise is to average the instantaneous value across the entire wing beat period, then make a comparison. Cycle-averaging the forces and moments eliminates the time-dependency of the comparison, and previous work has suggested that the cycle-averaged forces and moments are most critical in determining the motion of an insect-sized flapping vehicle [38, 88, 89].

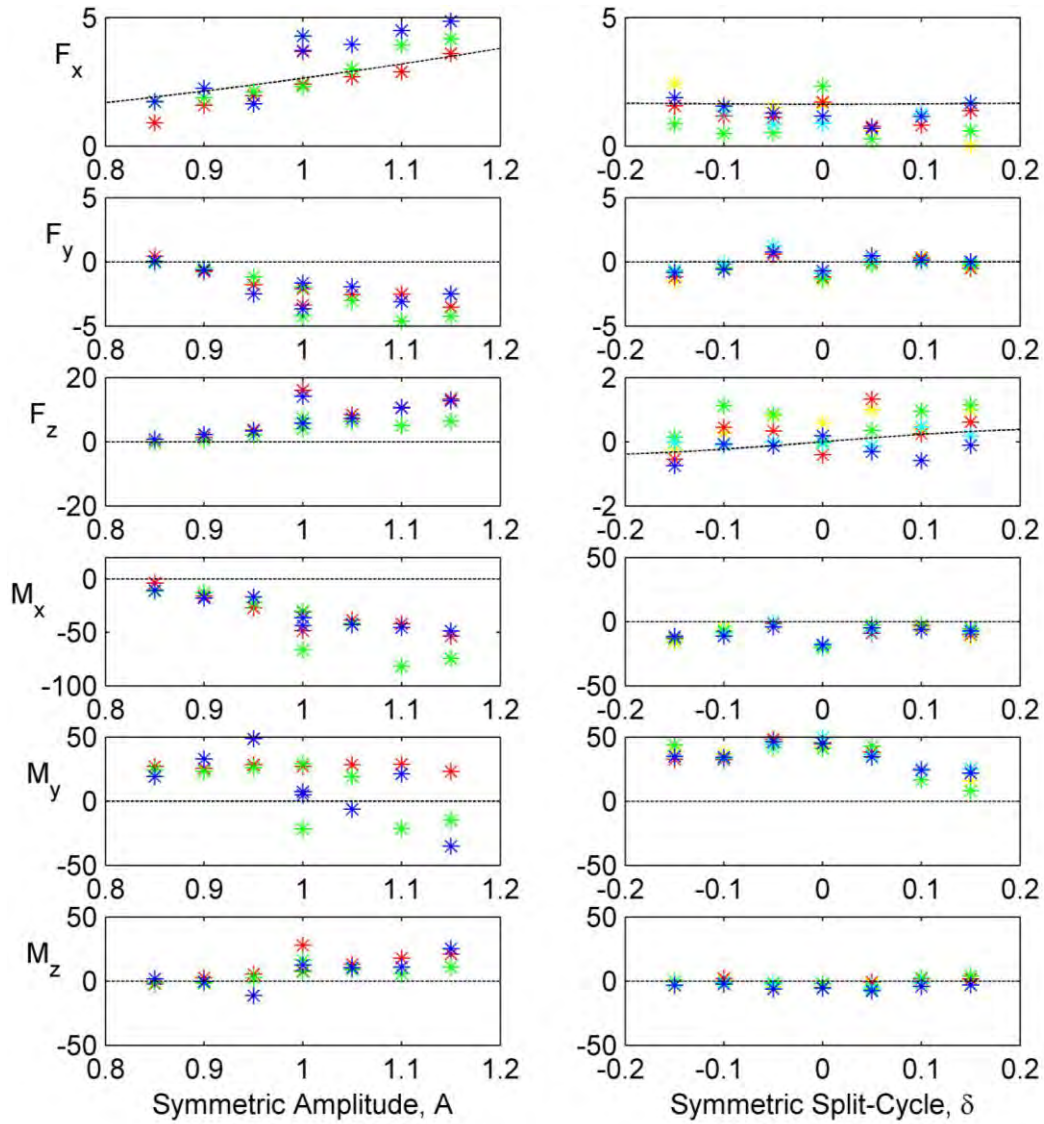


Figure 6.5. Force (mN) and moment ($mN\text{-}mm$) measurements for symmetric flapping, colors represent repeated trials.

These blade-element based predictions of cycle-averaged control forces and moments are plotted versus each control parameter as dashed lines in Figure 6.5 and Figure 6.6. The slope of each curve at the origin represents the control derivative linearized about hover, and matches the control effectiveness matrix given in Eq. 3.49

above. The MAV geometric properties used in the blade element calculations are given in Table 6.2. Plotted on top of these blade-element predictions are the experimentally measured values, cycle-averaged as described above. For each abscissa value, four or five ordinate values are plotted to give an indication of the repeatability of the measurement. The minimum agreement for the BABM control technique to be feasible is that the measured derivatives have the same sense as the prediction for all likely values of the control parameter. Take note that the mounting configuration of the MAV (shown in Figure 6.1) increases the sensitivities of M_y and M_x , and the data was not adjusted to compensate for this.

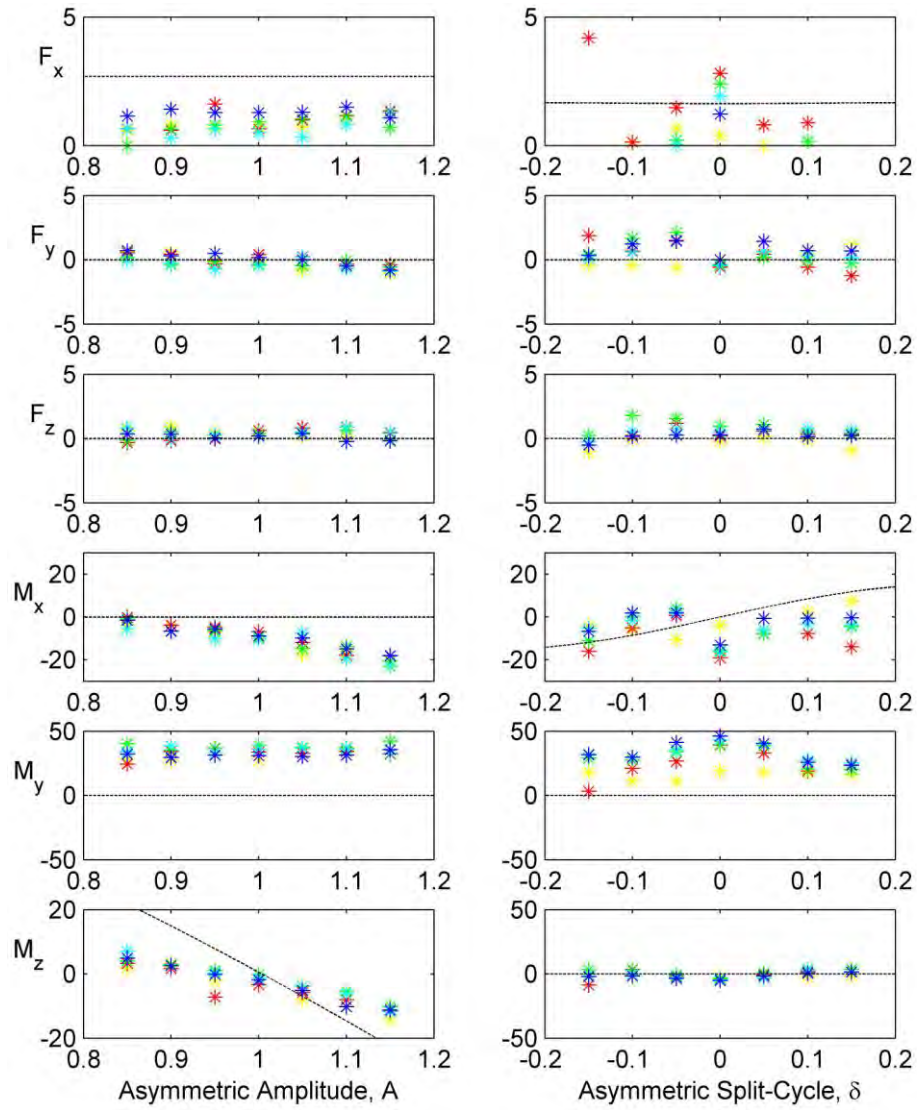


Figure 6.6. Force (mN) and moment ($mN\text{-}mm$) measurements for asymmetric flapping.

Table 6.2. MAV parameters used for blade-element calculation.

Parmeter	ω	A_0	ρ	C_L	C_D	I_A	α	w	Δx	x_{CP}	y_{CP}
Units	Hz	rad	kgm^3	-	-	m^4	deg	m	m	m	m
Value	23	0.8	1.2	1.2	1	1.76e^{-7}	35	0.01	0.0005	0.001	0.03

At first glance, it is clear that there is significant variability in the measured data. Some of this variability can be attributed to measurement noise because the values being measured are very close to the noise floor of the sensor. To mitigate this, multiple data sets were collected at each test point. The sensor itself proved to be very finicky, and some channels measured better than others. For example, the F_z channel had severe drift problems that could not be eliminated. Despite the variability, there are some clear trends in the data, some that were predicted and some that were not. The left column of Figure 6.5 gives results for symmetric amplitude modulation. The analysis predicted that lift should increase with increasing amplitude, and this trend is clearly visible in the data, but it also predicted no relationship between the other DOF, which is not seen. For example, the results show a clear coupling between symmetric amplitude modulation and F_y and F_z . These relationships are likely a result of asymmetric flapping by the MAV, possibly arising from manufacturing variability. For this particular prototype, the left wing is more responsive to actuator voltage, so as the commanded flapping amplitude is increased, the left wing flaps with greater amplitude, generating a net sideforce, F_y . We expect that closed, outer-loop feedback will mitigate these issues in a final design to control position.

The right column of Figure 6.5 gives results for symmetric split-cycle modulation. According to analysis, there should be a relationship between the split-cycle parameter and F_z , which there is, and limited coupling between the other DOF, which is also the case. The expected relationship with F_z is subtle in the measured data, and the blade element analysis predicted this mild coupling. In this case, the predicted values are very close to the noise floor of the sensor, so we should expect difficulty in measuring this

relationship. To compensate for this, additional measurements were taken on a similar prototype with an Ohaus Digital Pro single-DOF scale accurate to tenths of milli-grams. The results, shown in Figure 6.7, plot the mean and one standard deviation error bars over blade element predictions. This plot demonstrates the desired coupling between split-cycle parameter and F_z .

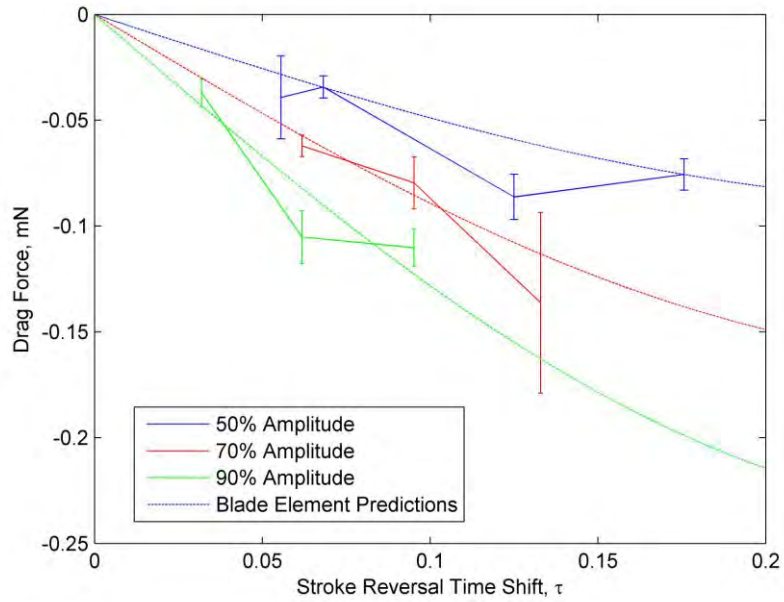


Figure 6.7. Cycle-averaged F_z force resulting from split-cycle wing flapping.

Figure 6.6 gives results for asymmetric modulation of amplitude and split-cycle. The left column plots the measured values against the amplitude of the right wing, so at a given data point, the left wing would be complimentary. For example, when the right wing has an amplitude of 1.15, the left has an amplitude of 0.85. Asymmetric amplitude modulation should correlate to M_z , with limited coupling with the other DOF. The M_z trend is evident, though slightly more subtle than predicted. This may be a result of

saturation of the actuators on the far extremes of their operating range. An interesting finding is the coupling with F_y and M_x , which was not predicted by analysis. Here, span-wise flow (which is ignored by the blade element formulae) on each wing is unbalanced because of the asymmetric amplitudes, resulting in a net side-force, F_y . This side-force is amplified by the cantilever mounting of the MAV to generate the M_x measurements. This coupling could be beneficial because the purpose of asymmetric amplitude modulation is to create yaw torques that would enable translation in the Y-axis, therefore, the additional F_y side-force would contribute to this desired attitude.

Finally, the right column of Figure 6.6 gives the results of asymmetric split-cycle modulation, where analysis predicts a net moment about the vertical axis, or roll (M_x). This trend is very vague if it is present at all, and would be very sensitive to any net side-force (F_y) acting on the cantilever mounting of the MAV. The predicted lack of coupling between other DOF is apparent, though there is a troubling randomness to the lift (F_x) data for this test.

In general, there is significant variability in the data, though several of the more important trends for MAV control were detected. To improve the fidelity of the measurements, a more powerful MAV prototype could be used that would generate measurements with a higher signal to noise ratio. Experiments on an improved prototype will be described below. Alternatively, a more sensitive sensor could be used. To our knowledge, a more sensitive 6-DOF sensor is not available, but one or two-DOF sensors could be acquired or custom-made that would be more sensitive [52]. This would improve the fidelity of the individual channels measured, but the unexpected couplings

that were discovered here would be missed. Notwithstanding the loss of measured DOF, there is a significant challenge in selecting a sensor for this application. Because of the flapping wings, the sensor must have “high” bandwidth, probably at least 4 times the flapping frequency of the vehicle. The three sensors we tested all had bandwidths of approximately 200 Hz which would limit flapping frequency to 50 Hz, maybe less. On the other hand, increased bandwidth usually results in decreased sensitivity, which is possibly even more critical. The fact that aerodynamic surfaces are flapping will make any time-accurate force and moment sensing problematic, and more so as the vehicle scale is reduced.

6.3 Improved Cycle-Averaged Forces and Moments

The experiments described in the previous section yielded promising results, but were inconclusive because the prototype MAV produced insufficient aerodynamic forces that were too close to the noise floor of the sensor. Here, an improved prototype, capable of more conclusive results, was tested. The prototype used was the “Version 3” prototype described in Chapter 4. This prototype was improved over the aforementioned previous design in three primary ways. First, wing inertia was reduced by using a thinner, $2.5\ \mu\text{m}$ Mylar membrane and narrower carbon fiber wing veins. This increased the system resonance to $28\ \text{Hz}$, allowing for higher flapping frequencies. Second, wing rotation stops were added to enforce the angle of attack, and third, the actuators were rotated out of the stroke plane to create a more flight-worthy vehicle, as discussed in Section 4.1.

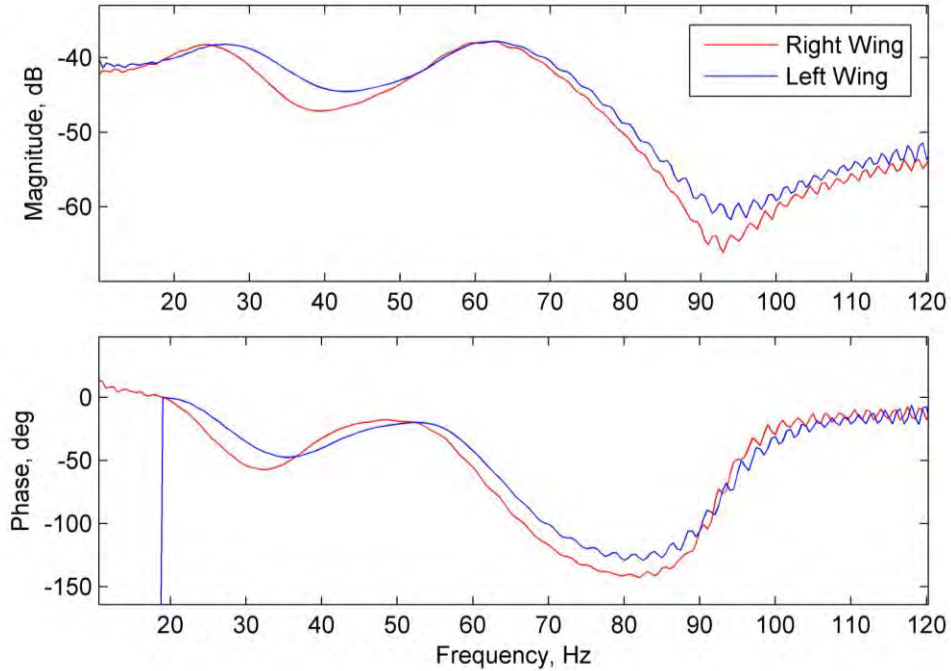


Figure 6.8. Frequency response functions of the right and left wings of the Version 3 MAV prototype.

The combined FRF plots of the right and left wing of this prototype are given in Figure 6.8. There is some measurement noise in the data because it was very difficult to focus the laser on the narrow, half-millimeter wing spars of the version 3 wings. Nevertheless, the system dynamics of the two wing flapping systems are well matched, and are a marked improvement over the previous prototype. The two resonant peaks represent the primary wing flapping mode and the secondary wing rotation mode, which was not present in early FRF plots because the passive wing rotation was poorly implemented. The version 3 prototype required a new mounting configuration which is shown in Figure 6.9. Take note that the new mounting configuration increases the

sensitivities of M_y and M_z , and the data was not adjusted to compensate for this. In addition to these design changes, the test vehicle was pushed harder during testing in that the voltages applied to the wing flapping actuators were closer to the failure limits of the actuators. This increased the wing flapping amplitude and increased aerodynamic force production.

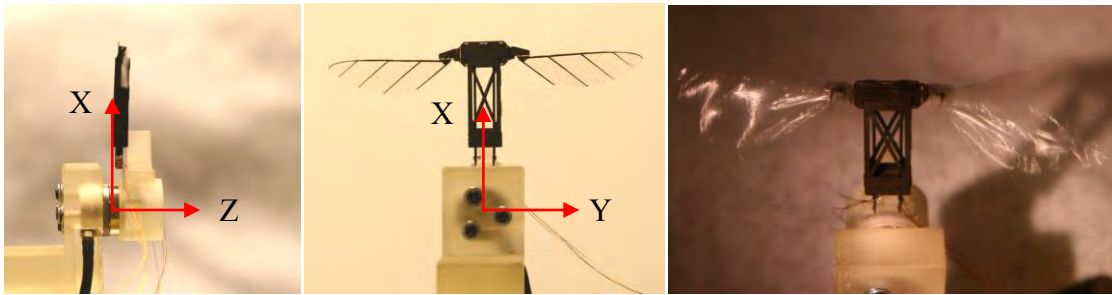


Figure 6.9. Version 3 MAV prototype and test stand with axes labeled.

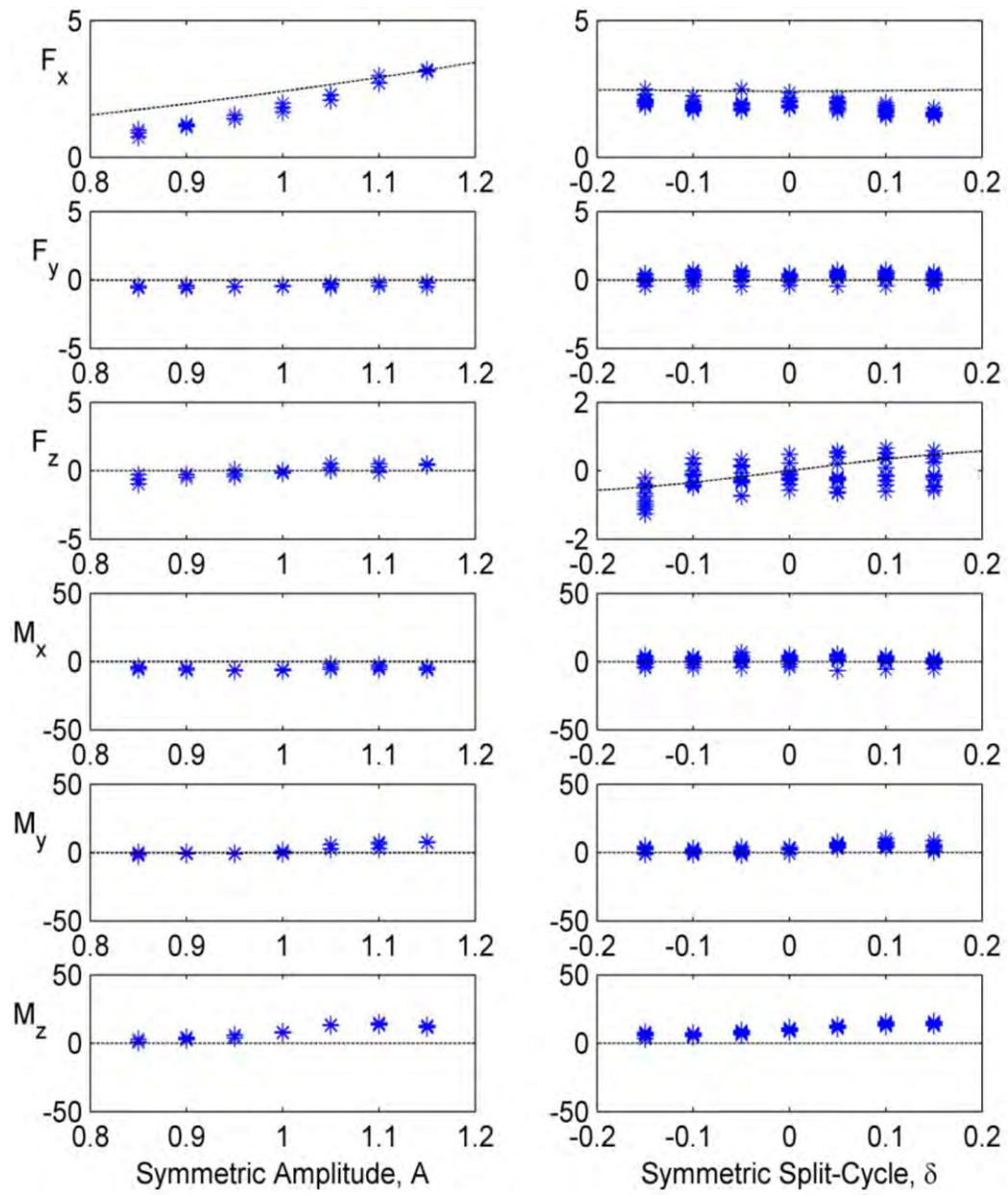


Figure 6.10. Improved force (mN) and moment ($mN\text{-}mm$) measurements for symmetric flapping.

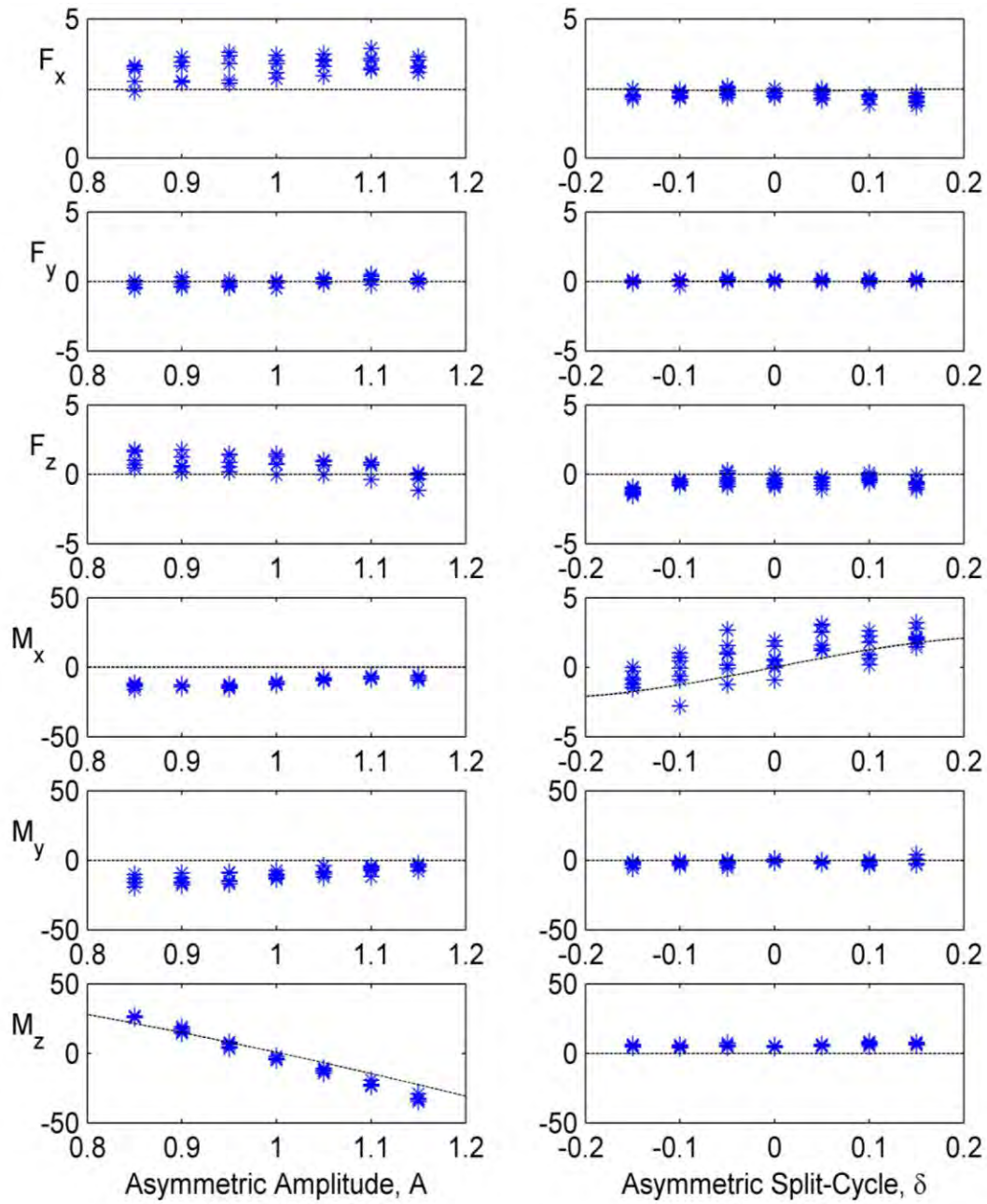


Figure 6.11. Improved force (mN) and moment ($mN\cdot mm$) measurements for asymmetric flapping.

Again, the blade-element based predictions of cycle-averaged control forces and moments are plotted versus each control parameter as dashed lines in Figure 6.10 and Figure 6.11. Compare these with Figure 6.5 and Figure 6.6, and take note that some of the scales vary to capture the full range of measured data. The MAV geometric properties used in the blade element calculations are identical to those given in Table 2, except that the flapping frequency has been increased to 28 *Hz* from 23 *Hz*. Plotted on top of these blade-element predictions are the experimentally measured values, cycle-averaged as described above. For each abscissa value, five to twelve ordinate values are plotted to give an indication of the repeatability of the measurement.

The data shown here with the Version 3 prototype is predictably improved. For the symmetric amplitude experiment (left column of Figure 6.10), the predicted relationship between amplitude modulation and F_x is clearly demonstrated, with little coupling between the other DOF. There is some coupling with M_z . This is likely a result of a slight asymmetry between the two wing amplitudes which generates a net side-force due to span-wise flow. This side-force is then greatly amplified by the aforementioned cantilevered mounting arrangement. Such an asymmetry would be easily corrected by closed-loop feedback in a final MAV design.

Asymmetric amplitude modulation is shown in the left column of Figure 6.11 which plots the measured values against the amplitude of the right wing, so at a given data point, the left wing would be complimentary. For example, when the right wing has an amplitude of 1.15, the left has an amplitude of 0.85 (these values represent 115% and 85% of the nominal amplitude, A_o , respectively). The predicted trend of a strong

relationship between asymmetric amplitude and M_z is clearly demonstrated, with little coupling between the other DOF. Furthermore, the total lift, F_x , remains relatively constant indicating that the vehicle would be capable of yawing into a turn without losing lift.

In addition to amplitude modulation, the MAV's response to frequency modulation was also tested, which has been proposed as an alternative to amplitude modulation [28, 29]. The results of this experiment are given in Figure 6.12. As expected, the MAV generates more lift as frequency increases, but starts to saturate as the frequency departs too far from the system resonance. This suggests that symmetric frequency modulation may be viable as long as the range of frequencies is limited. Of course, this behavior is entirely dependent on the frequency response of the wing flapping system, therefore, it will vary from one vehicle to the next. The larger, and more massive the wings, the stronger resonant peak should be expected and the more critical resonant flapping becomes. For example, compare the FRFs of the version 2 prototype wings given in Figure 6.13 to those of the version 3 prototype given in Figure 6.8. The version 2 wings are relatively heavier than the version 3 wings, so they demonstrate stronger resonant peaks than the version 3 wings that are more susceptible to the damping applied by the air. Further, there may yet be complications with implementing asymmetric frequency modulation, as there will likely be cross-talk between the two wing flapping systems.

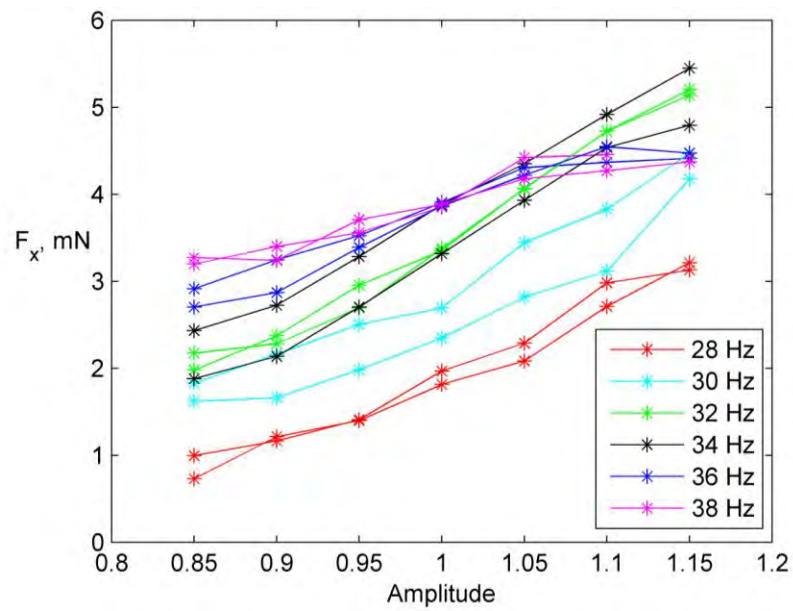


Figure 6.12. Symmetric frequency modulation.

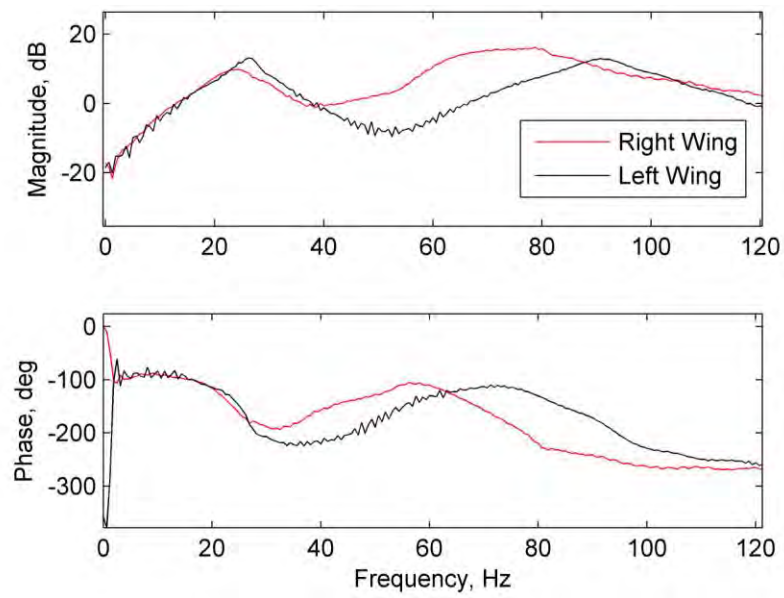


Figure 6.13. FRFs of left and right wings of version 2 prototype.

The split-cycle experiments, shown in the right columns of Figure 6.10 and Figure 6.11 are less definitive. In general, the split-cycle waveform modulation produced net forces that are useful for vehicle control, but they are less consistent and slightly lower than predicted. In the right column of Figure 6.10 the predicted relationship between split-cycle modulation and F_z is somewhat weak. Figure 6.14 shows a detail view of this relationship for all 12 data sets that were obtained. The desired trend exists, but has significant variability. It should be noted that these values are very close to the noise floor of the sensor, and may be suffering from measurement noise. As long as the trend given by the data is a reflection of the actual flow physics, then it should be possible to implement closed-loop control on the final vehicle. The low magnitude of the force will only limit the vehicle's performance along that DOF. Fortunately, the predicted lack of coupling between split-cycle modulation and the other DOF is apparent, which will greatly simplify implementation of the control system. Once again, it is shown that force production remains relatively constant during split-cycle modulation, which is essential to maintain stable flight.

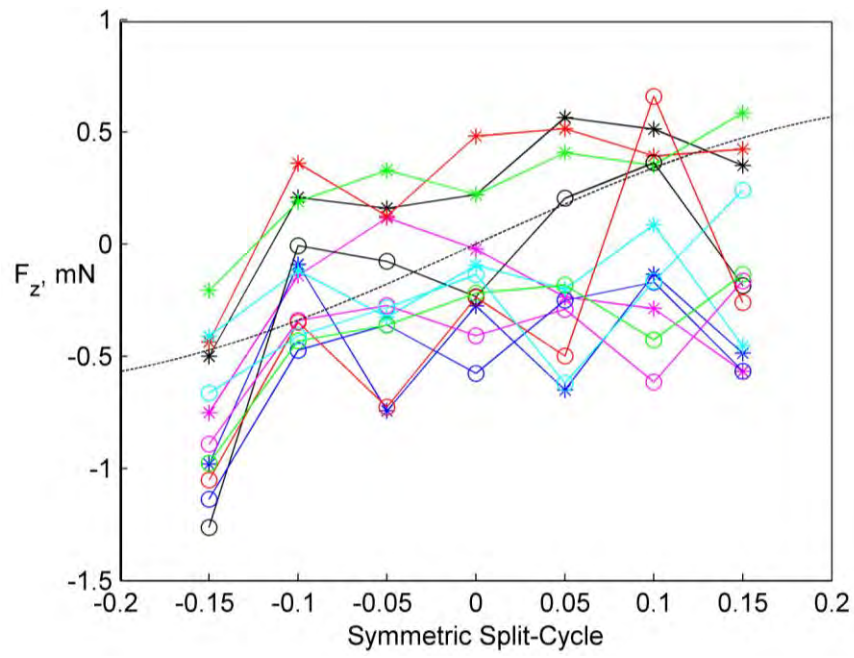


Figure 6.14. Symmetric split-cycle modulation.

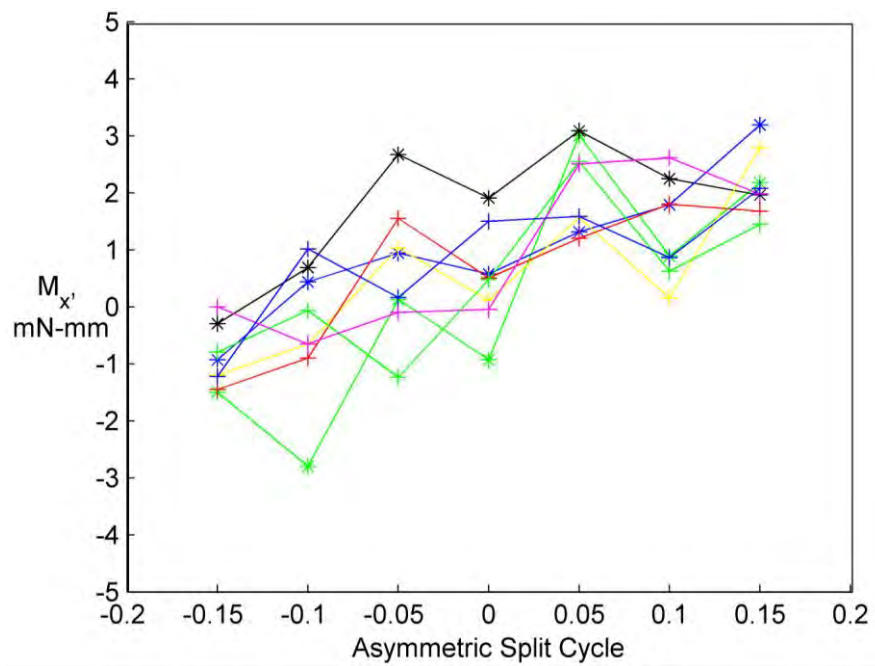


Figure 6.15. Asymmetric split-cycle modulation.

The relationship between asymmetric split-cycle and M_x given in the right column of Figure 6.11 is similar. The measurements match the predicted trend but only in a stochastic sense as there is significant variability. A detailed view is given in Figure 6.15, which clearly shows the predicted trend, though there is variability. To verify that split-cycle motion of the wings was being achieved, the laser vibrometer was used to capture the wing trajectory and the resultant plot is given in Figure 6.16. This figure measured the motion of the tip of the piezo actuator of the right wing, and clearly there is more than just the fundamental flapping frequency present in the wing trajectory. There is also additional high frequency content which is a result of the inelastic collision between the rotating wing and the wing stops. This interaction likely is removing energy from the system, and is undesirable. Future efforts should be made to reduce the magnitude of this interaction, or tune the rotation joint precisely enough that rotation stops are not needed.

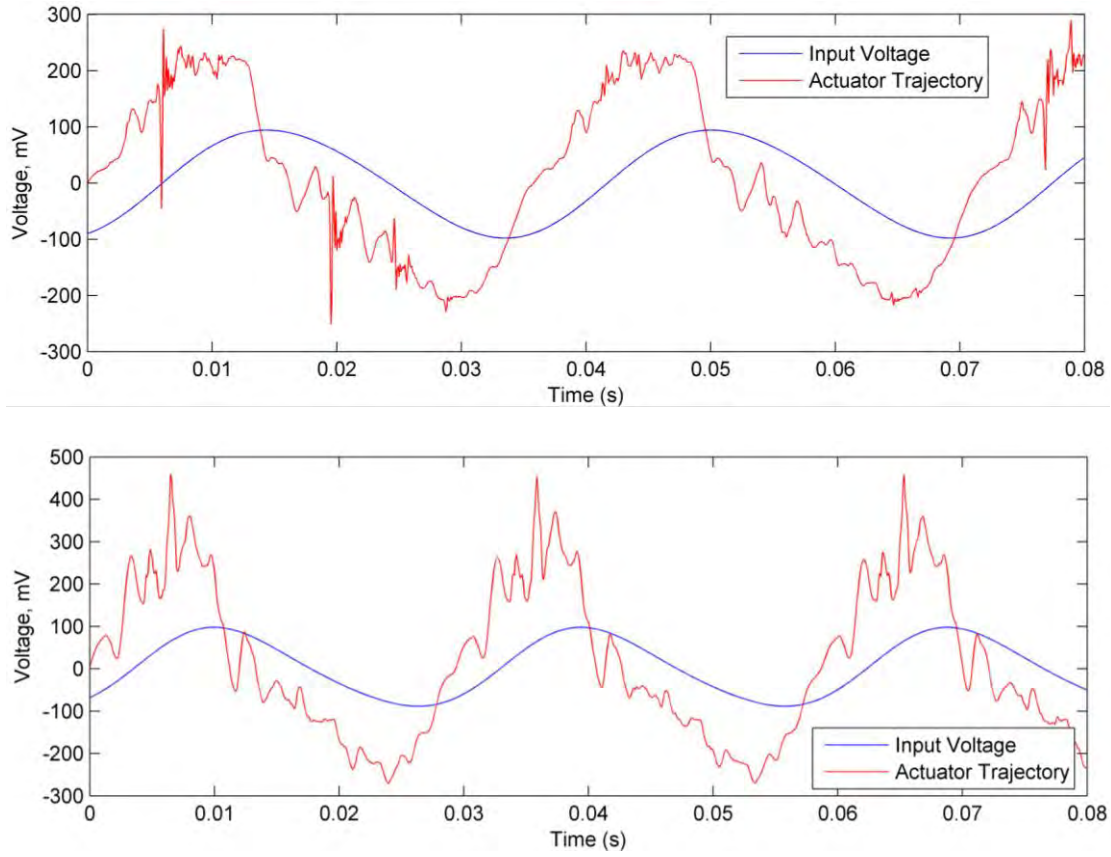


Figure 6.16. Laser vibrometer measurement of right wing trajectory for $\Delta = 0.05$ (top) and $\Delta = 0.15$ (bottom).

As a whole, these force and moment measurements verify that the proposed Biharmonic Amplitude and Bias Modulation technique for flapping wing control does produce forces and moments in four of the five DOF that it was predicted to effect. This is a very encouraging result and a necessary intermediate step on the way to full state closed-loop control. The fifth DOF that was not tested on the force transducer is bias modulation which is predicted to affect the pitching moment, M_y . This DOF was not

tested because the balance was not expected to be sensitive enough to detect the small changes in pitching moment that were predicted by the blade-element model.

An alternative and intriguing approach to measuring the prototype's response to BABM would be to use the MAV itself as the sensor by allowing it to move in a constrained environment. For example, the MAV could be fastened to a vertical tether that allowed it to translate vertically, but constrained all other DOF. This would allow the effects of amplitude modulation to be directly observed, however this introduces new sets of complications such as stiction, gravitational effects, and tethering interactions.

Numerous other kinematic constraints can be implemented that create constrained motion environments to test one, two, or three DOF at a time. Examples of some of the possible constraint combinations are given in Figure 6.17.

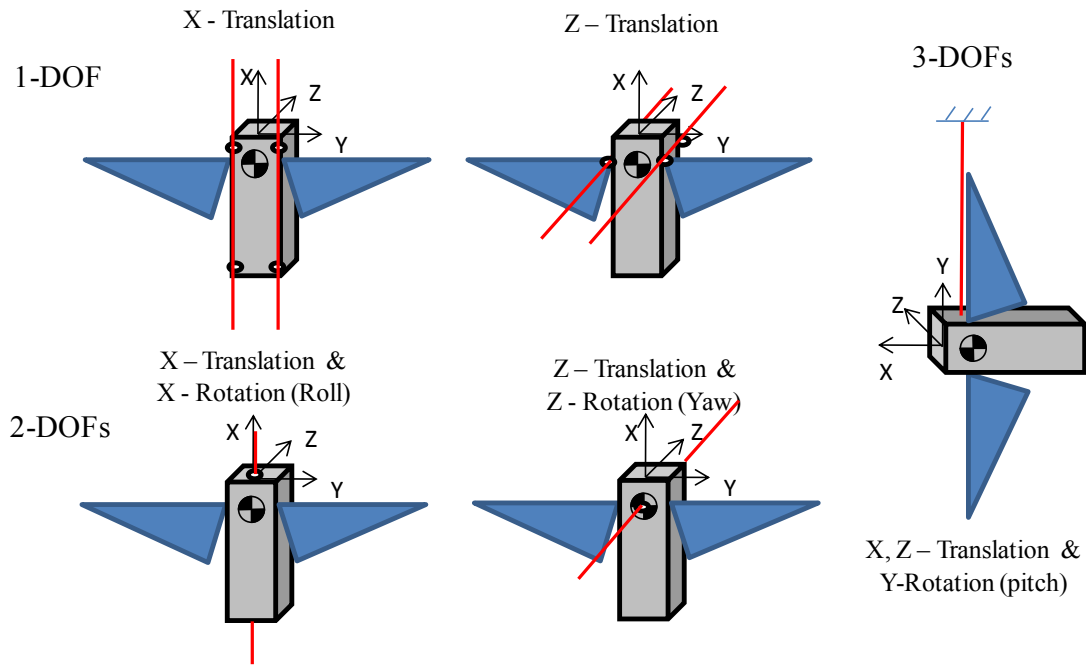


Figure 6.17. Examples of constrained motion MAV flight control experiments.

To date, two such constrained motion experiments have been performed testing pitch (Y-rotation) and yaw (Z-rotation). The pitch experiment setup is shown in Figure 6.18 in which the MAV fuselage is pinned so that it can rotate about the pinned axis. Power to the actuators is supplied from off the vehicle, so the wires will further constrain the vehicle motion. Therefore, care was taken to reduce this influence by aligning the wires with the axis of rotation so that the wires did not need to translate, but only rotate. Nevertheless, the wires inhibited the vehicle motion significantly, making efforts to quantify the resulting motion futile. Instead, only a qualitative assessment was made. The vehicle performed as expected, pitching forward and back as a result of the additional control bias. Figure 6.19 shows video capture of this experiment in which the

MAV can be clearly seen pitching forward as a result of a DC bias being applied to the wing trajectory.

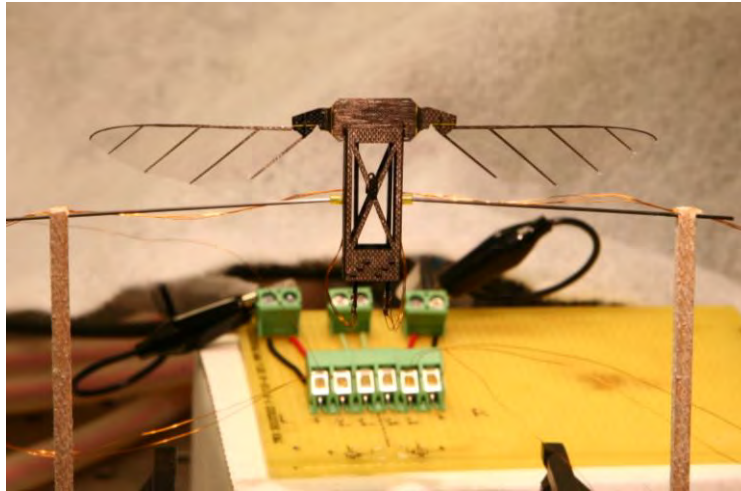


Figure 6.18. Pitch constrained motion experiment.

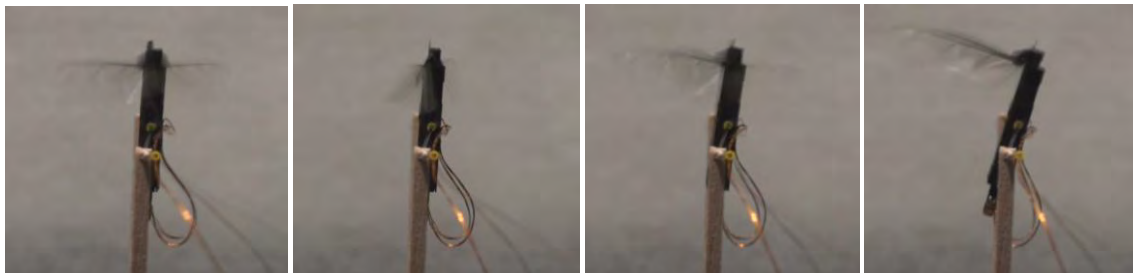


Figure 6.19. Video capture of the MAV pitching forward as a result of wing bias modulation.

A second experiment tested the predicted yaw motion (rotation about Z axis). The test rig is shown in Figure 6.20 in which the MAV is threaded on a narrow steel rod so that it can rotate. Again, the actuator drive wires are routed along the axis of rotation to reduce their influence on the experiment. The vehicle was very responsive to the

asymmetric flapping amplitude modulation, increasing the angular displacement in proportion to the modulated wing amplitudes, and able to yaw to the left and right. A video capture of the resulting experiment is given in Figure 6.21.

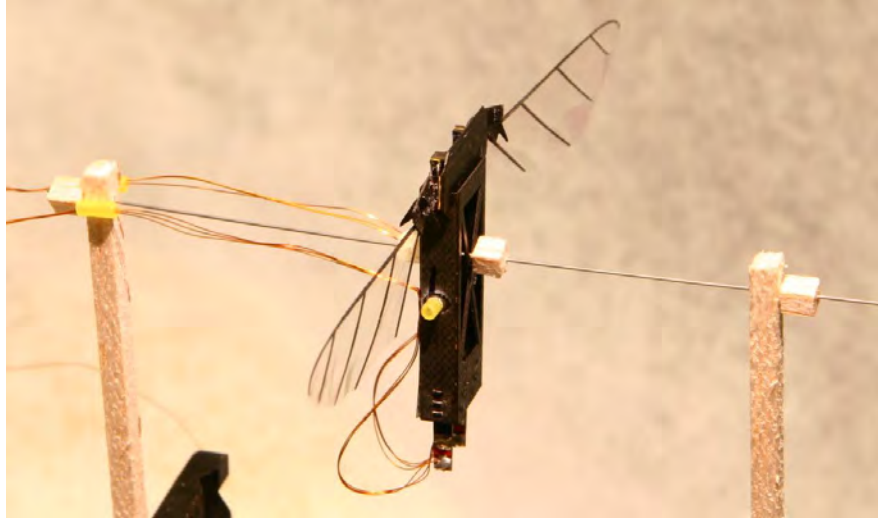


Figure 6.20. Yaw constrained motion experiment.

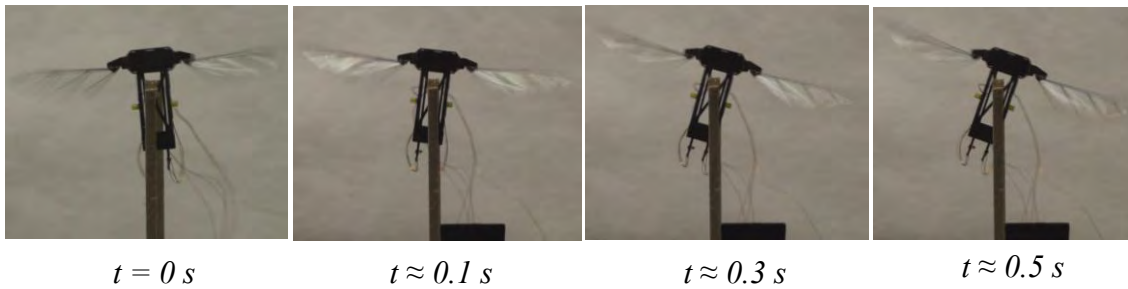


Figure 6.21. Video capture of the MAV yawing as a result of asymmetric wing amplitude modulation.

These two constrained motion experiments demonstrate the feasibility of such methods for qualitatively evaluating a proposed control technique. In particular, they verify the effectiveness of the BABM technique for imparting pitch and yaw moments on the vehicle, which further validate the force and moment measurement experiments. In sum, the three sets of experiments described in this chapter show that the BABM control technique is capable of producing forces and moments to influence five DOF of a flapping wing vehicle. In addition, these experiments have demonstrated that the quasi-steady blade-element based analytical predictions of the effectiveness of the BABM technique were reasonably accurate, despite the numerous assumptions that were necessary to obtain them. This is an important result for the general field of flapping wing control of MAVs because it validates the analytical method as a useful tool for evaluating proposed control techniques.

7. Conclusions

The work described in this document represents a significant research effort towards advancing the field of flapping wing control of MAVs. In the process of this work, several significant contributions have been made which have indeed advanced the field. The stated goal was to evaluate the thesis statement:

Direct modulation of each wing's stroke velocity alone is sufficient to provide a minimum 5-DOF control of an insect-sized flapping wing MAV.

This hypothesis was evaluated over several steps. First, a thorough review was made of previous work. Only a handful of serious attempts had been made to design control techniques for tail-less flapping wing vehicles. These efforts generally consisted of recommendations for how the wing kinematics should be modulated to generate the desired body forces and moments on an MAV, followed by quasi-steady, blade-element based analysis and/or numerical simulations to predict the efficacy of these wing kinematics. These works were pioneering in their novelty, but left many unanswered questions, particularly, whether or not these analysis methods sufficiently predicted the MAV behavior.

Upon reviewing the previous work, a novel flapping wing control technique was developed called Bi-harmonic Amplitude and Bias Modulation. This technique is unique because it is applicable to resonant wing flapping, which will be necessary to optimize efficiency of flapping flight. A detailed analysis was performed that predicted the BABM technique could generate uncoupled forces and moments on a MAV in five

degrees of freedom with active control of only one DOF per wing, thus requiring only two actuators on the vehicle.

While this novel technique appeared promising, much work remained to prove its feasibility beyond numerical simulations. Therefore, an extensive effort was undertaken to develop flapping wing MAV prototypes capable of implementing the BABM control technique. This required a vehicle with wing flapping actuators capable of modulating frequency, amplitude and bias, therefore, piezoelectric bimorph cantilever actuators were selected and tested. In addition, an original wing flapping mechanism was designed and built to transform the linear actuator motion into useful wing flapping. Low inertia, stiff wings were also developed along with vehicle fuselages to complete the prototypes.

Before testing the DHPC/BABM control technique in entirety, it was necessary to demonstrate that a flight-weight wing flapping system could be driven non-harmonically at resonance. Specifically, it was critical to verify that the time-shifted “split-cycle” wing trajectory necessary for BABM control could be performed by the wing. Testing was performed, and a new technique was developed for open-loop wing trajectory control called Discrete Harmonic Plant Compensation. This technique made it possible to flap the wings as desired, without requiring extensive computational effort.

Finally, the entire BABM control technique was tested by measuring the forces and moments produced by the flapping wings. Two sets of experiments totaling over 600 specific tests were performed on two different prototypes. These experiments evaluated BABM by driving the flapping wings with the kinematics specified by the controller, then measuring the resultant forces and moments. The experiments verified that the

BABM technique does in fact produce the forces and moments predicted by analysis, which should be sufficient for vehicle control. Finally, two constrained motion experiments were performed to demonstrate the ability to change the vehicle attitude in two DOF.

7.1 Research Conclusions

The tasks described above and performed in the course of this research were designed to answer specific questions about flapping wing control of MAVs, but additional insights were gained while performing the research and these will all be discussed in detail.

1. Are control schemes that utilize non-harmonic wing flapping trajectories applicable to resonant as well as non-resonant frequencies?

Experiments described in Chapter 5 initially determined that a flight-weight wing flapping mechanism could not track non-harmonic flapping trajectories near resonance, if driven open-loop, or without compensation. However, a novel technique called Discrete Harmonic Plant Compensation (DHPC) was developed to compensate for the wing flapping system dynamics which allows the wings to track non-harmonic flapping trajectories near resonance. In this work we have proven that control schemes that utilize non-harmonic wing flapping trajectories are applicable to resonant as well as non-resonant frequencies when adequately compensated with something like DHPC.

2. Are quasi-steady blade-element analyses adequate for predicting aerodynamic forces and moments for the design of FWMAV controllers?

Experiments presented in Chapter 6 demonstrated that the blade-element analysis accurately predicted the cycle-averaged forces and moments generated by the MAV prototype when flapping with the wing kinematics prescribed by the controller. However, some coupling between DOF were discovered that were not predicted by the blade element analysis. For example, asymmetric amplitude modulation generates an unpredicted side force as a result of span wise flow that is not present in the blade element analysis. Therefore, these blade element predictions are sufficiently accurate for designing FWMAV controllers, but should be verified through experimentation to uncover interactions such as these before implementing closed-loop control.

3. Are the forces and moments generated by non-harmonic wing trajectories with constant angle-of-attack sufficient to control a FWMAV?

The tethered motion experiments performed on the version 3 MAV prototype and described in Chapter 6 (Figure 6.19 and Figure 6.21) demonstrate that the M_z yaw moment generated by asymmetric amplitude modulation and the M_y pitch moment are sufficient to change the attitude of the tested MAV prototype. However, there is insufficient evidence at this time to make a general claim of the ability of generic non-harmonic wing trajectories to control generic FWMAVs.

4. What are the limitations of the BABM control scheme and how would they constrain the design of such a vehicle and/or limit its performance?

Analysis performed and described in Chapter 3 demonstrated that the BABM control scheme is limited in its ability to generate M_x roll moments, and Z-translation as a result of the limited ability to flap the wings non-harmonically. In general, the split-cycle force

development is limited by the wing-actuator system dynamics and voltage limits on the actuator, as described in Chapter 5. The attenuation by the wing flapping system of the higher frequency content in the non-harmonic trajectory requires additional voltage to be applied to the actuators at those higher frequencies which eventually is limited by the capabilities of the actuator. As our MAV designs are improved, it is expected that the vehicle will have greater excess power available. This will make it possible to amplify the higher harmonic of the bi-harmonic trajectory without saturating against the actuator voltage limit.

In addition, the analysis also predicted that the BABM control scheme would be unable to generate side force. In fact, the experiments described in Chapter 6 demonstrated that side force is generated, but it is coupled to yaw moment through the asymmetric amplitude modulation. Fortunately, as long as the wing center of pressure is above the vehicle center of mass, this is an assistive effect, in that the side force acts in the direction of the yaw, so this should not limit vehicle performance.

5. Can insect-sized flapping wing MAV prototypes be built inexpensively and repeatably?

The techniques described in Chapter 4 were used to build MAV prototypes on a shoestring budget. The most expensive pieces of equipment required were the laser machining stations, which can range from tens of thousands to millions of dollars to acquire. However, laser micromachining can be hired out for around \$200 per hour, so it is not necessary to obtain these machines. Furthermore, alternative techniques such as chemical etching or PCB routing could be used to achieve similar results at much lower

costs. The prototypes built demonstrated remarkable repeatability given the amount of assembly steps performed by hand. For example, work published by Sladek demonstrates the structural and aerodynamic repeatability of the AFIT wings, and the FRFs of the wings of the Version 3 prototype given in Figure 6.8 demonstrate the repeatability of the wing flapping mechanism.

The answers to these questions listed above give sufficient insight to evaluate the thesis statement. The work described herein is insufficient to prove the hypothesis that 5-DOF *control* can be achieved through direct modulation of each wing's stroke velocity alone. That statement is too strong because controllability was not directly tested, or otherwise proven. Controllability in the strict sense depends on the vehicle plant, which would be different for every vehicle so it is likely not possible to prove this hypothesis in general. Instead, a slightly weaker, but no less important claim can be made: *Direct modulation of each wing's stroke velocity alone is sufficient to generate forces and moments in 5-DOF of an insect-sized flapping wing MAV.*

7.2 Significant Contributions

In the course of this work, several contributions have been made to the field of FWMAV design and control which are significant:

1. A novel flapping wing control technique, BABM was developed and shown through analysis and hardware testing to be capable of generating forces and moments on the vehicle in 5 DOF while being applicable to resonant wing flapping. To date, this is the most mature and thoroughly tested control technique yet proposed in the literature for insect-sized MAVs. Furthermore,

it requires the fewest actuators of any of the previously proposed techniques so should be simplest to implement [5].

2. Developed, tested and published numerous novel techniques for low cost and repeatable manufacturing of meso-scale composite devices. These techniques were used here for the manufacture of flapping wing micro air vehicles, but could be applied to numerous other micro-robotic devices, or other fields and materials as well [7].
3. Developed the first ever flight-worthy prototype MAV in this size/weight envelope and the first-ever insect-sized vehicle with independently articulated wings. Previously developed flapping wing prototypes in all size regimes uniformly utilize coupled wing flapping wherein a central actuator flaps both wings. This arrangement makes asymmetric flapping impossible, and tailless controlled flight very unlikely. The prototypes developed here are the first in the world capable of evaluating flapping wing flight control [7].
4. Provided a novel technique with low computational cost for generating non-harmonic oscillation trajectories of flexible structures near resonance. The DHPC technique that was developed was necessary to be able to implement the BABM flapping wing control, but may have other applications as well. Any requirement to oscillate an object with a non-harmonic trajectory at resonance could utilize the DHPC technique, including locomotion for terrestrial or aquatic robots, or ultrasonic piezo motors [3, 4].

5. Performed the first hardware-in-the-loop testing of any flapping wing control scheme, creating experience and lessons learned for future researchers. The force and moment measurements were the first experiments ever performed on a flight-weight prototype to evaluate a flapping wing control technique, and gave tremendous insight into flapping flight. Likewise, the constrained motion experiments are the first-ever hardware-in-the-loop experiments to demonstrate the ability to influence the attitude of an insect-sized MAV with its flapping wings alone [6].
6. Determined the feasibility of FWMAV control through non-harmonic wing flapping with passive wing rotation. The force and moment measurements and constrained motion experiments have clearly demonstrated that the BABM control technique and other techniques requiring non-harmonic wing trajectories are feasible for controlling a FWMAV [8].

7.3 Recommendations for Future Work

The work performed here has demonstrated the feasibility of the BABM control technique which should motivate future research to continue its development toward unconstrained flapping wing controlled flight and eventually autonomous flight. To work towards this final goal, several milestones need to be achieved. First, further constrained motion experiments should be performed to test motion in other DOF and to test multiple DOF at once. Closed-loop constrained motion experiments can and should be performed concurrently with these tests, which would be the first of their kind. To accomplish this, feedback will be required, so a means of capturing the vehicle attitude and motion in real

time along the DOF being tested will be necessary. A triangulated video system with feature tracking could be the most expedient option.

Closed-loop motion controllers will need to be designed and tested. These may initially be as simple as single-input, single-output proportional controllers, eventually growing in complexity to a monolithic multi-input, multi-output state-space controller to handle coupling effects. Adaptive and/or nonlinear control techniques may be necessary to account for the often variable and nonlinear force and moment production demonstrated in Chapter 6.

The current prototypes are lifting approximately 50%-75% of their total prototype weight. To most realistically test the ability of BABM to control the vehicle in all DOF, the vehicle should be capable of lifting its own weight. For example, a closed-loop altitude tracking demonstration would be very useful. It could be performed with the current prototype if the vehicle were sliding along a less-than-vertical track so that it only had to lift a portion of its weight, however, the test would be more realistic if it were conducted on a vertical track, and the prototype were capable of lifting itself. Eventually the vehicle will need to be able to lift its own weight and still have excess power available to maximize maneuverability. Therefore, the ongoing efforts to improve the MAV force production should continue.

The process for improving vehicle performance should include both efforts to reduce the vehicle takeoff weight and increase the aerodynamic force production. Weight can be saved by reducing the number and gauge of the actuator wires, and structurally optimizing the fuselage. Aerodynamic force production can be improved in a

number of ways. Efforts to increase the system resonance and flapping frequency by custom building actuators has been very successful, but there is a tradeoff with flapping amplitude. A trade study should be performed to improve this relationship so that flapping amplitude and frequency are both at an optimal level. Furthermore, there is an open question of how much resonance is desirable. It has been shown here that the quality factor of resonant wing flapping can be altered by changing the mass properties of the wing (i.e., all other things being equal a heavier wing will have a higher Q), but it is still not known what quality factor is desirable for the greatest aerodynamic force production.

The interaction between the wing flapping system resonance and wing rotation is complex and critical to performance, which became evident in the effort to increase system resonance [91]. A concerted effort should be made to better understand this relationship so that deliberate decisions can be made in designing prototypes. Along with this is the question of wing rotation joint stops. These enforce a desired AoA, but (as currently designed) certainly reduce the efficiency of flapping by removing energy from the system with each inelastic collision. If the wing rotation could be tuned to the point that the correct AoA could be achieved without stops, the vehicle performance would surely improve. Alternatively, even if the force of impact could be reduced through tuning of the design, an improvement in performance would be achieved.

Furthermore, the question of what the AoA should be has never been addressed. The current figure of 45° was recommended as a result of work performed over a decade ago at a different Re number from that of the current prototypes [71]. Therefore, an

experiment to alter the angle of attack while measuring lift production should be performed on a flight-weight prototype. This could be performed by starting with the current wing rotation stops and incrementally removing pieces of the stop to increase the AoA while taking a lift force measurement at each AoA value. All of these possible avenues for aerodynamic force production improvement would require relatively minor changes to the MAV design, but may require diligent and well-designed experiments to determine what the changes should be.

A tethered, but unconstrained controlled flight of an insect sized MAV should be the near-term goal and logical follow-on to this work. This will require a prototype with sufficient excess power to lift itself and maneuver, a system to perform real-time tracking of the vehicle attitude in 6 DOF with sufficient bandwidth, and a robust and well-vetted multi-input, multi-output BABM controller. It will be a significant challenge to accomplish all of these tasks, but the reward would be a monumental contribution to the field of flapping wing control; the first controlled flight of an insect-sized FWMAV.

Appendix

MAV Prototype Technical Drawings

Contents

Transmission Version 1

Transmission Version 2

Transmission Version 3

Transmission Version 4

Transmission Version 4 - Detail

Fuselage Version 1 (For use with Transmission Version 2)

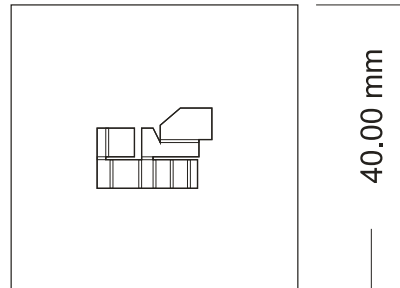
Fuselage Version 4 (For use with Transmission Version 4 and OPT 39.5/2.1/.7 Actuators)

Fuselage Version 4.2 (For use with Transmission Version 4 and Custom Actuators)

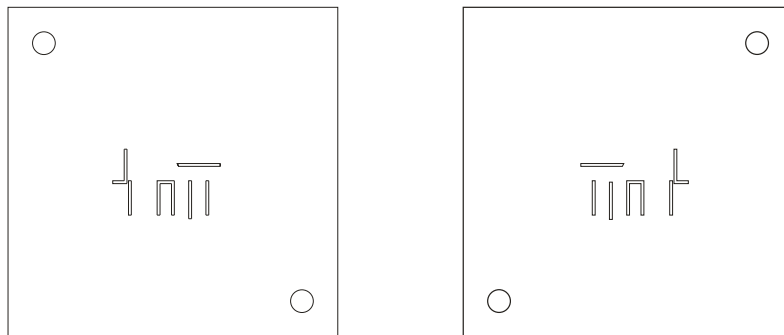
Actuators

Wing Version 4

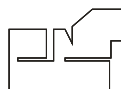
Overview



Pocket Layer

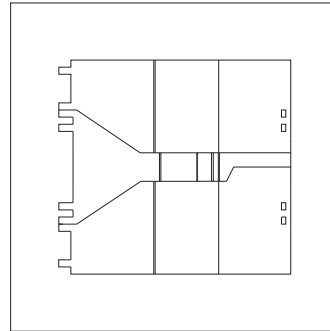
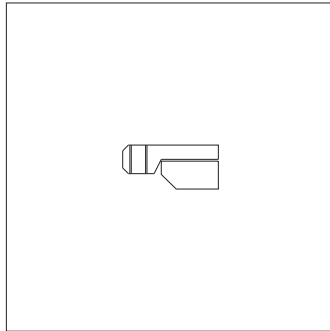


Perimeter Layer

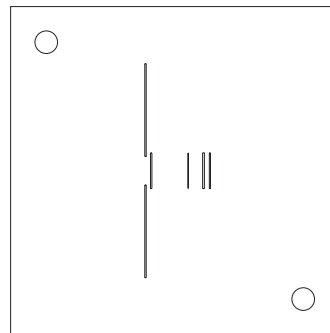
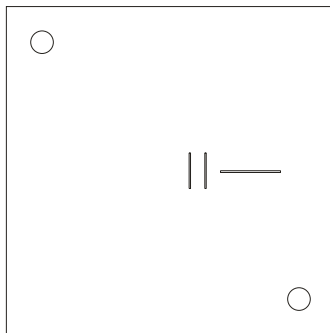


Michael L. Anderson	Transmission
Department of Aeronautics and Astronautics	Version 1
Air Force Institute of Technology	September 2011

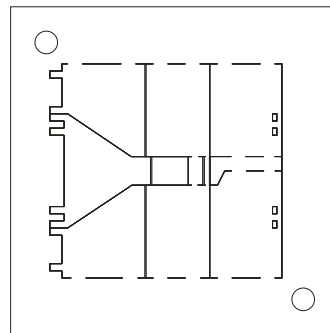
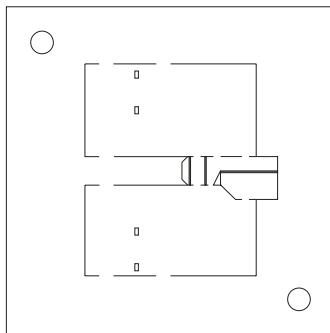
Overview



Pocket Layer



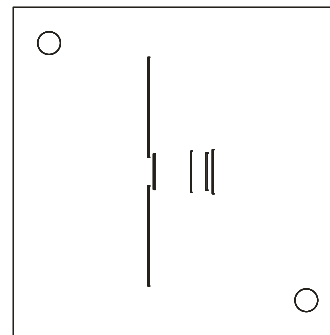
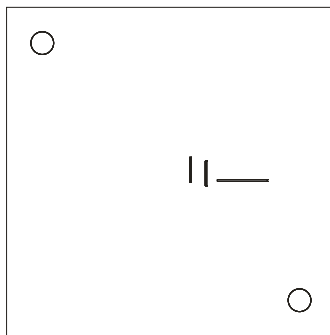
Perimeter Layer



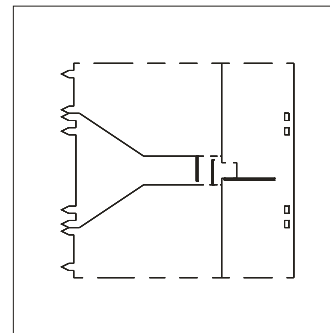
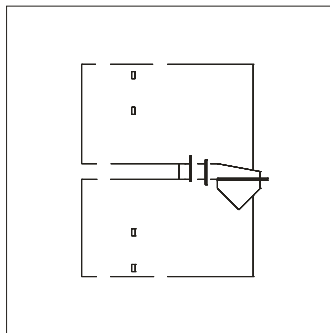
Michael L. Anderson	Transmission
Department of Aeronautics and Astronautics	Version 2
Air Force Institute of Technology	September 2011

Overview

Pocket Layer

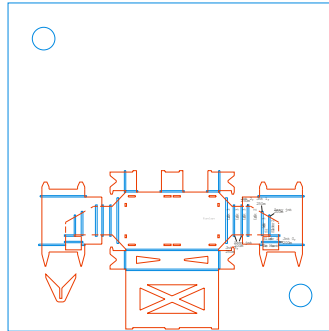


Perimeter Layer

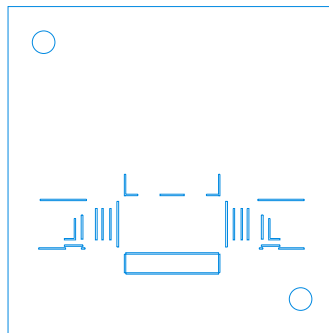


Michael L. Anderson	Transmission
Department of Aeronautics and Astronautics	Version 3
Air Force Institute of Technology	September 2011

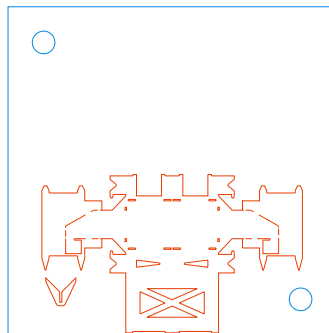
Overview



Pocket Layer

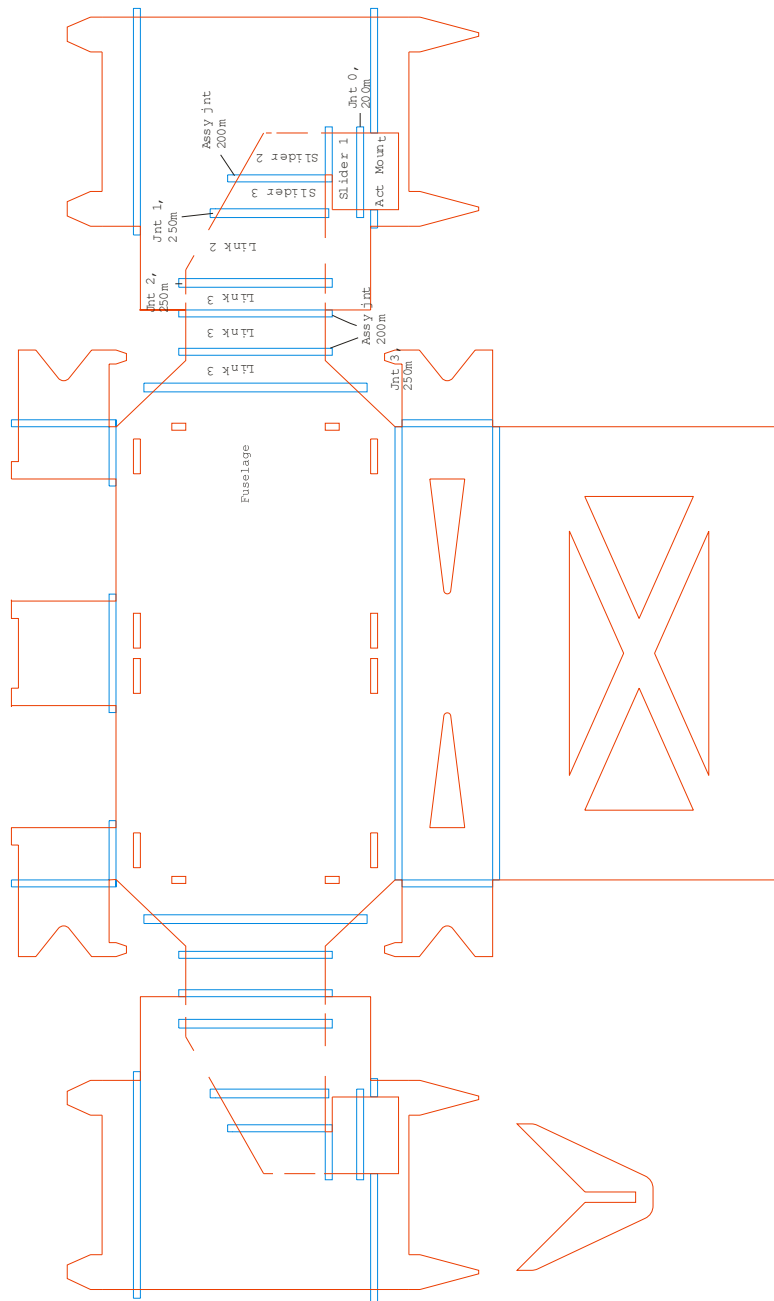


Perimeter Layer



Michael L. Anderson	Transmission
Department of Aeronautics and Astronautics	Version 4
Air Force Institute of Technology	September 2011

Overview



Michael L. Anderson

Department of Aeronautics and Astronautics

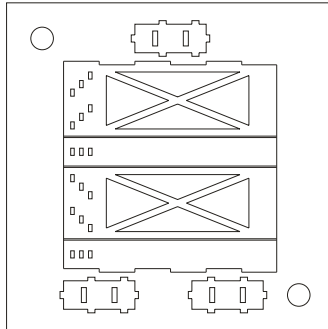
Air Force Institute of Technology

Transmission

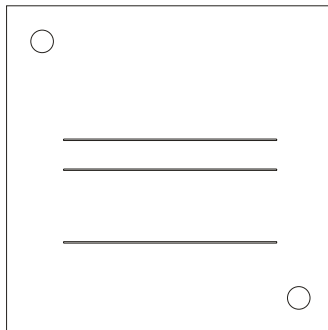
Version 4 - Detail

September 2011

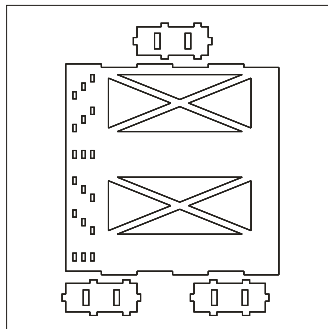
Overview



Pocket Layer

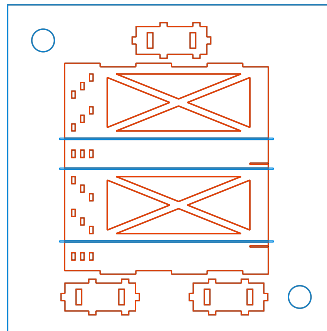


Perimeter Layer

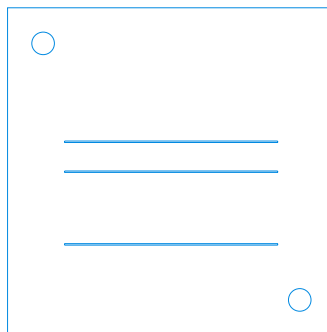


Michael L. Anderson	Fuselage
Department of Aeronautics and Astronautics	Version 1
Air Force Institute of Technology	September 2011

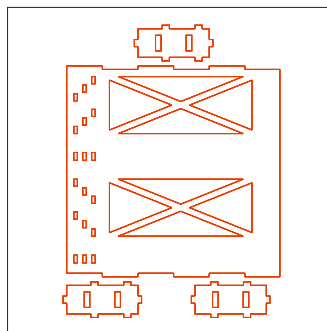
Overview



Pocket Layer

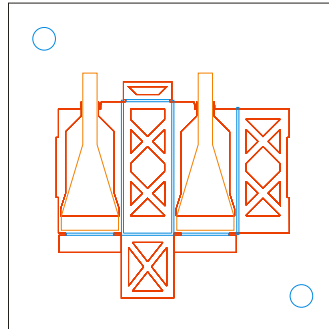


Perimeter Layer

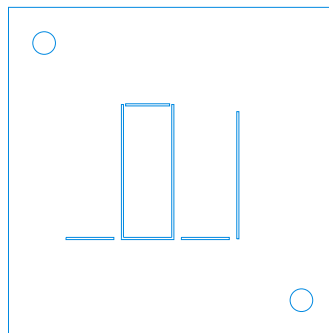


Michael L. Anderson	Fuselage
Department of Aeronautics and Astronautics	Version 4
Air Force Institute of Technology	September 2011

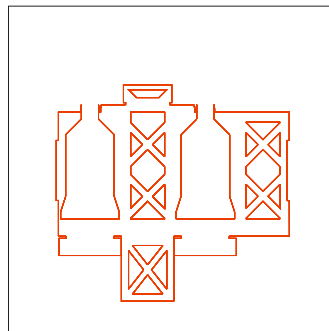
Overview



Pocket Layer

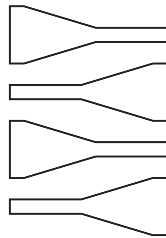


Perimeter Layer

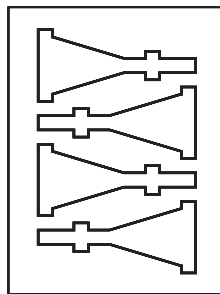


Michael L. Anderson	Fuselage
Department of Aeronautics and Astronautics	Version 4.2
Air Force Institute of Technology	September 2011

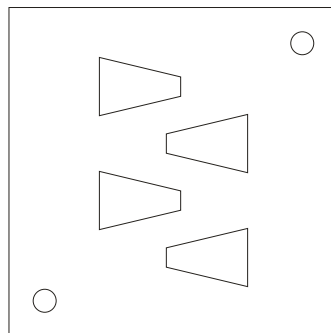
Carbon Fiber Cutouts



Mold Cutout

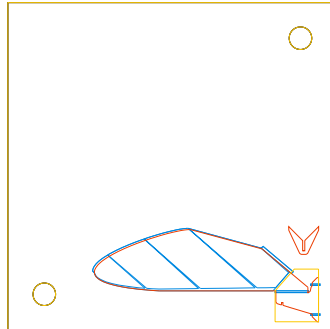


PZT Cutouts

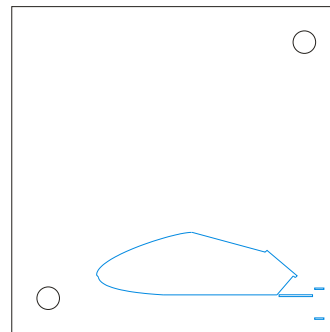
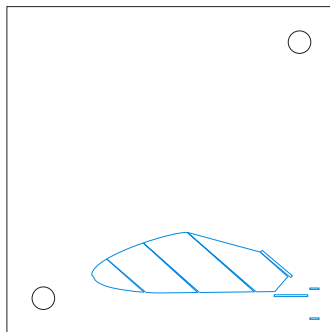


Michael L. Anderson	Actuator
Department of Aeronautics and Astronautics	Version 4
Air Force Institute of Technology	September 2011

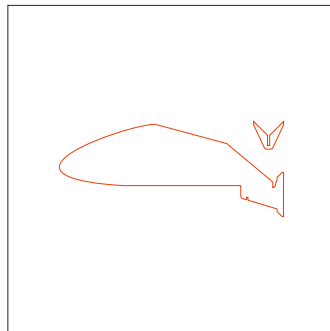
Overview



Pocket Layer



Perimeter Layer



Michael L. Anderson

Department of Aeronautics and Astronautics

Air Force Institute of Technology

Wing

Version 4.2

September 2011

Bibliography

1. Alexander, D.E., *Nature's Flyers*, The Johns Hopkins University Press, Baltimore, MD, 2002.
2. Alexander, R. M., *Principles of Animal Locomotion*, Princeton University Press, 2003.
3. Anderson, M.L., and Cobb, R.G., "Frequency Response of a Micro Air Vehicle Wing Flapping Actuator to Non-Harmonic Forcing," *AIAA Paper 2010-2708*, April 2010.
4. Anderson, M.L., and Cobb, R.G., "Techniques for Non-Harmonic Wing Flapping for the Control of Micro Air Vehicles," *AIAA Paper 2010-7555*, August, 2010.
5. Anderson, and Cobb, "Towards Flapping Wing Control of Micro Air Vehicles," *AIAA Journal of Guidance Control and Dynamics*, (to be published).
6. Anderson, M.L., and Cobb, R.G., "Evaluation of Bi-harmonic Amplitude and Bias Modulation for Flapping Wing MAV Control," *AIAA Paper 2011-1161*, Orlando, FL, Jan 2011.
7. Anderson, M.L., Sladek, N.J., and Cobb, R.G., "Design, Fabrication , and Testing of an Insect-Sized MAV Wing Flapping Mechanism," *AIAA Paper 2011-0549*, Orlando, FL, Jan 2011.
8. Anderson, "Design and Testing of Flapping Wing Control for a Micro Air Vehicle," *AIAA Guidance Navigation and Control Conference*, Portland, OR (to be published).
9. Avadhanula, S., and Fearing, R.S., "Flexure Design Rules for Carbon Fiber Microrobotic Mechanisms," *Proceedings of the IEEE International Conference on Robotics and Automation*, Barcelona, Spain, Apr 2005, pp. 1579-1584.
10. Avadhanula, S., Wood, R. J., Campolo, D., and Fearing, R. S., "Dynamically Tuned Design of the MFI Thorax," *Proceedings of the 2002 IEEE International Conference on Robotics and Automation*, Washington, DC, May 2002.
11. Avadhanula, S., Wood, R. J., Steltz, E., Yan, J., and Fearing, R. S., "Lift Force Improvements for the Micromechanical Flying Insect," *Proceedings of the 2003*

IEEE/RSJ International Conference on Intelligent Robots and Systems, Las Vegas, Nevada, October 2003.

12. Azuma, A., *The Biokinetics of Flying and Swimming*, 2nd ed., AIAA Education Series, Reston, VA, 2006.
13. Balint, C. N., and Dickinson, M. H., "Neuromuscular Control of Aerodynamic Forces and Moments in the Blowfly, *Calliphora vicina*," *The Journal of Experimental Biology*, Vol. 207, 3813-3838.
14. Bansevicius, R., Blechertas, V., "Multi-Degree-of-Freedom Ultrasonic Motors for Mass-Consumer Devices," *Journal of Electroceramics*, Vol 20, 2008, pg 221-224.
15. Bar-Cohen, Y., *Electroactive Polymer Actuators as Artificial Muscles: Reality, Potential and Challenges*, International Society for Optical Engineering, Bellingham, WA, 2004.
16. Bolsman, C. T., Goosen, J.F.L., and van Keulen, F., "Insect-inspired Wing Actuation Structures Based on Ring-Type Resonators," *Proceedings of the SPIE*, Vol. 6928, 2008.
17. Chakravarthy, A., and Albertani, R., "In-Flight Dynamically Adaptive Configurations: Lessons from Live Lepidoptera," *AIAA Paper 2010-2828*, April, 2010.
18. Chakravarthy, A., Albertani, R., Gans, N., and Evers, J., "Experimental Kinematics and Dynamics of Butterflies in Natural Flight," *AIAA Paper 2009-873*, January, 2009.
19. Conn, A. T., Burgess, S. C., and Ling, C. S., "Design of a Parallel Crank-Rocker Flapping Mechanism for Insect-Inspired Micro Air Vehicles," *Proceedings of the Institution of Mechanical Engineers – Part C-- Journal of Mechanical Engineering Science*, Vol. 221, April 2007.
20. de Croon, G.C.H.E., de Clerq, K.M.E., Ruijsink, R., Remes, B., and de Wagter, C. "Design, Aerodynamics, and Vision-Based Control of the DelFly," *International Journal on Micro Air Vehicles*, Vol. 1, No. 2, pp. 71 – 97, 2009.
21. Davis, Kosicki, Boroson, Kostishock, "Micro Air Vehicles for Optical Surveillance," *The Lincoln Laboratory Journal*, Vol. 9, No. 2, 1996.

22. Dawson, D., *Repeatable Manufacture of Wings for Flapping Wing Micro Air Vehicles Using Micro Electromechanical System Fabrication Techniques*, Air Force Institute of Technology (AU), Wright-Patterson AFB OH, March 2011.
23. Deng, X., Schenato, L., Wu, W. C., and Sastry, S. S., "Flapping Flight for Biomimetic Robotic Insects: Part I – System Modeling," *IEEE Transactions on Robotics*, Vol. 22, no. 4, August, 2006.
24. Deng, X., Schenato, L., and Sastry, S. S., "Flapping Flight for Biomimetic Robotic Insects: Part II – Flight Control Design," *IEEE Transactions on Robotics*, Vol. 22, no. 4, August, 2006.
25. Department of Defense. *Unmanned Aircraft Systems Roadmap 2005-2030*. Washington: GPO, 4 August 2005.
26. Dickson, W. B., Straw, A. D., and Dickinson, M. H., "Integrative Model of *Drosophila* Flight," *AIAA Journal*, Vol. 46, No. 9, September, 2008.
27. Doman, D. B., Oppenheimer, M. W., and Bolender, M., "Altitude Control of a Single Degree of Freedom Flapping Wing Micro Air Vehicle," *Proceedings of the AIAA Guidance, Navigation, and Control Conference*, Chicago, IL, 2009.
28. Doman, D. B. and Oppenheimer, M. W., "Dynamics and Control of a Minimally Actuated Biomimetic Vehicle: Part I – Aerodynamic Model," *Proceedings of the AIAA Guidance, Navigation, and Control Conference*, Chicago, IL, 2009.
29. Doman, D. B., Oppenheimer, M. W., and Sigthorsson, D. O. "Dynamics and Control of a Minimally Actuated Biomimetic Vehicle: Part II – Control," *Proceedings of the AIAA Guidance, Navigation, and Control Conference*, Chicago, IL, 2009.
30. Doman, D. B., Oppenheimer, M. W., and Sigthorsson, D. O., "Wingbeat Shape Modulation for Flapping-Wing Micro-Air-Vehicle Control During Hover," *Journal of Guidance, Control, and Dynamics*, Vol. 33, No. 3, May–June 2010.
31. Doman, D. B., Oppenheimer, M. W., and Sigthorsson, D. O., "Dynamics and Control of a Biomimetic Vehicle Using Biased Wingbeat Forcing Functions: Part II – Controller," *AIAA Paper 2010-1024*, January, 2010.
32. Doman, D.B., Tang, C.P, and Regisford, S., "Modeling Interactions Between Flexible Flapping Wing Spars, Mechanisms and Drive Motors," *AIAA Journal of Guidance, Control and Dynamics*, (to be published).

33. Dudley, R., and Ellington, C., "Mechanics of Forward Flight in Bumblebees: I. Kinematics and Morphology," *Journal of Experimental Biology*, Vol. 148, 19-52, 1990.
34. Dudley, R., and Ellington, C., "Mechanics of Forward Flight in Bumblebees: II. Quasi-steady Lift and Power Requirements," *Journal of Experimental Biology*, Vol. 148, 53-88, 1990.
35. Dudley, R., *The Biomechanics of Insect Flight*, Princeton University Press, Princeton, NJ, 2000.
36. Finio, B.M., Shang, J.K., and Wood, R.J., "Body Torque Modulation for a Microrobotic Fly," *Proceedings of the 2009 Institute of Electrical and Electronics Engineers International Conference on Robotics and Automation*, Kobe, Japan, May, 2009.
37. Finio, B.M., Eum, B., Oland, M., Wood, R.J., "Asymmetric Flapping for a Robotic Fly Using a Hybrid Power-Control Actuator," *The 2009 Institute of Electrical and Electronics Engineers /Robotics Society of Japan International Conference on Intelligent Robots and Systems*, St. Louis, MO, Oct., 2009.
38. Fry, S. N., Syaman, R., and Dickinson, M. H., "The Aerodynamics of Free-Flight Maneuvers in *Drosophila*," *Science*, Vol. 300, 495-498, April 2003.
39. Geder, J.D., and Ramamurti, R., "Modeling and Control Design for a Flapping-Wing Nano Air Vehicle," *AIAA Paper 2010-7556*, August, 2010.
40. Harris, C.M., *Shock and Vibration Handbook*, 3rd ed., McGraw-Hill, Blacklick, OH, 1988.
41. Hsu, C., Evans, J., Vytla, S., and Huang, P. G., "Development of Flapping Wing Micro Air Vehicles – Design, CFD, Experiment and Actual Flight," *Proceedings of the 48th AIAA Aerospace Sciences Meeting*, Orlando, Florida, January, 2010.
42. Hu, M., Wei, R., Shi, Z., and Zou, L., "Controllability Issues for Insect Like Flapping Wing Micro-Air Vehicle," *Proceedings of the 7th World Congress on Intelligent Control and Automation*, Chongqing, China, June 2008.
43. Hu, Z., Cheng, B., and Deng, X., "Lift Generation and Flow Measurements of a Robotic Insect," *AIAA Paper 2011-1311*, January, 2011.

44. Jones, K. D., Bradshaw, C. J., Papadopoulos, J., and Platzer, M. F., "Improved Performance and Control of Flapping-Wing Propelled Micro Air Vehicles," *AIAA Paper 2004-0399*, January, 2004.
45. Karni, E., Johnson, M., Stiltner, B., Fogleman, K., Gelhausen, P., Willis, D., Lind, R., and Patil, M., "A Software Suite for Conceptual Design of Flapping Wing MAVs," *AIAA Paper 2011-550*, January, 2011.
46. Karpelson, M., Wei, G.Y., and Wood, R. J., "A Review of Actuation and Power Electronics Options for Flapping-Wing Robotic Insects," *Proceedings of the 2008 IEEE International Conference on Robotics and Automation*, Pasadena, CA, May 2008.
47. Keennon, M. T., and Grasmeyer, J. M., "Development of the Black Widow and Microbat MAVs and a Vision of the Future of MAV Design," *Proceedings of the AIAA/ICAS International Air and Space Symposium and Exposition*, Dayton, Ohio, July 2003.
48. Khan, Z. A., and Agrawal, S. K., "Wing Force and Moment Characterization of Flapping Wings for Micro Air Vehicle Application," *Proceedings of the 2005 American Control Conference*, Portland, Oregon, 2005.
49. Khan, Z., and Agrawal, S., "Design of Flapping Mechanisms Based on Transverse Bending Phenomena in Insects," *Proceedings of the 2006 IEEE International Conference on Robotics and Automation*, Orlando, Florida, May 2006.
50. Khan, Z. A., and Agrawal, S. K., "Control of Longitudinal Flight Dynamics of a Flapping-Wing Micro Air Vehicle Using Time-Averaged Model and Differential Flatness Based Controller," *Proceedings of the 2007 American Control Conference*, New York, New York, July 2007.
51. Khan, Z., Steelman, K., and Agrawal, S., "Development of Insect Thorax Based Flapping Mechanism," *Proceedings of the 2009 IEEE International Conference on Robotics and Automation*, Kobe, Japan, May 2009.
52. Kumar, R., Silin, D., and Shkarayev, S., "Experimental Study of Aerodynamic Performance of Locust and Model Wings," *AIAA Paper 2011-871*, January, 2011.
53. Liang, Z., and Dong, H., "Unsteady Aerodynamics and Wing Kinematics Effect in Hovering Insect Flight," *AIAA Paper 2009-1299*, January, 2009.

54. Liu, C., *Foundations of MEMS*, Pearson Prentice Hall, Upper Saddle River, New Jersey, 2006.
55. Liu, T., "Comparative Scaling of Flapping- and Fixed-Wing Flyers," *AIAA Journal*, Vol. 44, No. 1, 2006.
56. Meirovitch, L., *Methods of Analytical Dynamics*, Dover Publications, Mineola, NY, 2003.
57. Michelson, R. C., "Test and Evaluation of Fully Autonomous Micro Air Vehicles," *ITEA Journal*, 29: 367-374, 2008.
58. Mueller, T. J. (ed.) *Fixed and Flapping Wing Aerodynamics for Micro Air Vehicle Applications*, Progress in Aeronautics and Astronautics, AIAA, Virginia, 2001.
59. Mueller, T.J., Kellog, J.C., Ifju, P.G., Shkarayev, S.V., *Introduction to the Design of Fixed-Wing Micro Air Vehicles*, AIAA Education Series, AIAA, Reston, Virginia, 2007.
60. Mukherjee, S., and Ganguli, R., "Nonlinear Dynamic Analysis of Dragonfly Inspired Piezoelectrically Driven Flapping and Pitching Wing," *AIAA Paper 2011-2073*, April, 2011.
61. Namiki Precision Jewel Company, *DC Coreless and Brushless Motors Catalog*, 2009.
62. O'Hara, R., Palazotto, A., "Structural Identification and Simulation of the Manduca Sexta Forewing," *AIAA Paper 2011-2066*, April, 2011.
63. Oppenheimer, M. W., Doman, D. B., and Sigthorsson, D. O., "Dynamics and Control of a Biomimetic Vehicle Using Biased Wingbeat Forcing Functions: Part I – Aerodynamic Model," *AIAA Paper 2010-1023*, January, 2010.
64. Oppenheimer, M. W., Doman, D. B., and Sigthorsson, D. O., "Multiple Degree-of-Freedom Control of a Flapping-Wing MicroAir Vehicle with Power and Control Actuators," *AIAA Paper 2010-7557*, August, 2010.
65. Oppenheimer, M.W., Sigthorson, D.O., and Doman, D.B., "Body Torque Generation for a Flapping Wing Micro Air Vehicle by Angle of Attack Change," *AIAA Paper 2011-1281*, January, 2011.

66. Orlowski, C.T., and Girard, A.R., "Averaging of the Nonlinear Dynamics of Flapping Wing Micro Air Vehicles for Symmetrical Flapping," *AIAA Paper 2011-1228*, January, 2011.
67. Pornsin-sirirak, T.N., Lee, S.W., Nassef, H., Grasmeyer, J., Tai, Y.C., Ho, C.M., and Keennon, M., "MEMS Wing Technology for a Battery-Powered Ornithopter," *Proceedings of the 13th IEEE Annual International Conference on MEMS*, Miyazaki, Japan, January, 2000.
68. Ramamurti, R., Geder, J., Sandberg, W., and Flynn, A., "Computational Fluid Dynamics Studies of a Flapping Wing Nano Air Vehicle," *AIAA Paper 2010-8117*, August, 2010.
69. Sakhaei, A., and Liu, G., "Model-Based Predictive Control of Insect-Like Flapping Wing Aerial Micro-Robot," *AIAA Paper 2010-7706*, August, 2010.
70. Sallstrom, E., Ukeiley, L., Wu., P., and Ifju, P., "Aerodynamic Forces on Flexible Flapping Wings," *AIAA Paper 2011-569*, January, 2011.
71. Sane, S.P., and Dickinson, M.H., "The Control of Flight Force by a Flapping Wing: Lift and Drag Production," *The Journal of Experimental Biology*, Vol. 204, 2607-2626, 2001.
72. Sane, S.P., and Dickinson, M. H., "The Aerodynamic Effects of Wing Rotation and a Revised Quasi-Steady Model of Flapping Flight," *The Journal of Experimental Biology*, Vol. 205, 1087-1096, 2002.
73. Sherman, A., and Dickinson, M., "Summation of Visual and Mechanosensory Feedback in Drosophila Flight Control," *Journal of Experimental Biology*, Vol. 207, No. 1, 133–142, 2004.
74. Shkarayev, S., and Silin, D., "Aerodynamics of Flapping-Wing Micro Air Vehicles," *AIAA Paper 2009-878*, January, 2009.
75. Shyy, W., Lian, Y., Tang, J., Viieru, D., Liu, H., *Aerodynamics of Low Reynolds Number Flyers*, Cambridge University Press, New York, 2008.
76. Sladek, N.J., *Flapping Wing Micro Air Vehicle Wing Manufacture and Force Testing*, Air Force Institute of Technology (AU), Wright-Patterson AFB OH, March 2011.

77. Spanner, K., "Survey of the Various Operating Principles of Ultrasonic Piezomotors," *Proceedings of the International Conference on New Actuators, Actuator 2006*, 2006.
78. Stanford, B., Kurdi, M., Beran, P., and McClung, A., "Shape, Structure, and Kinematic Parameterization of a Power-Optimal Hovering Wing," *AIAA Paper 2010-2963*, April, 2010.
79. Steltz, E., Avadhanula, S., and Fearing, R. S., "High Lift Force with 275 Hz Wing Beat in MFI," *Proceedings of the 2007 IEEE/RSJ International Conference on Intelligent Robots and Systems*, San Diego, CA, October 2007.
80. Steltz, E., and Fearing, R. S., "Dynamometer Power Output Measurements of Miniature Piezoelectric Actuators," *IEEE/ASME Transactions on Mechatronics*, Vol. 14, No. 1, February 2009.
81. Steltz, E., Seeman, M., Avadhanula, S., and Fearing, R. S., "Power Electronics Design Choice for Piezoelectric Microrobots," *Proceedings of the IEEE/RSJ International Conference on Intelligent Robots and Systems*, 2006.
82. Stevens, B. L., and Lewis, F. L., *Aircraft Control and Simulation, 2nd Ed.*, John Wiley & Sons, Inc., Hoboken, New Jersey, 2003.
83. Sun, M., and Xiong, Y., "Dynamic flight stability of a hovering bumblebee," *The Journal of Experimental Biology*, Vol. 208, 447-459, 2005.
84. Tanaka, H., and Wood, R.J., "Fabrication of Corrugated Artificial Insect Wings Using Laser Micromachined Molds," *Journal of Micromechanics and Microengineering*, Vol. 20, 2010.
85. Taylor, G. K., "Mechanics and aerodynamics of insect flight control," *Biological Review*, Vol. 76, 449-471, 2001.
86. Taylor, G. K., Bomphrey, R. J., and Hoen, J. T., "Insect Flight Dynamics and Control," *Proceedings of the 44th AIAA Aerospace Sciences Meeting*, Reno Nevada, January 2006.
87. Taylor, G. K., and Thomas, A. L. R., "Animal Flight Dynamics II: Longitudinal Stability in Flapping Flight," *Journal of Theoretical Biology*, Vol. 214, 315-370, 2002.

88. Taylor, G. K., and Thomas, A. L. R., "Dynamic flight stability in the desert locust *Schistocerca gregaria*," *Journal of Experimental Biology*, Vol. 206, 2803-2829, 2003.
89. Wang, H., Ando, N., Kanzaki, R., "Active control of free flight manoeuvres in a hawkmoth, *Agrius convolvuli*," *The Journal of Experimental Biology*, Vol. 211, 423-432, 2008.
90. Willmott, A. P., and Ellington, C. P., "The Mechanics of Flight in the Hawkmoth *Manduca Sexta* I. Kinematics of Hovering and Forward Flight," *The Journal of Experimental Biology*, Vol. 200, pg 2705 – 2722.
91. Whitney, J.P., and Wood, R.J., "Aeromechanics of passive rotation in flapping flight," *Journal of Fluid Mechanics*, Vol. 660, 197-220, 2010.
92. Wood, R. J., "Design, Fabrication and Analysis of a 3DOF, 3cm Flapping Wing MAV," *Proceedings of the 2007 IEEE/RSJ International Conference on Intelligent Robots and Systems*, San Diego, CA, November, 2007.
93. Wood, R.J., "The First Takeoff of a Biologically Inspired At-Scale Robotic Insect," *IEEE Transaction on Robotics*, Vol. 24, No. 2, April 2008.
94. Wood, R.J., Avadhanula, S., and Fearing, R.S., "Microrobotics Using Composite Materials," *Proceedings of the IEEE International Conference on Robotics and Automation*, Taipei, Taiwan, May 2003.
95. Wood, R.J., Avadhanula, S., Sahai, R., Steltz, E., and Fearing, R.S., "Microrobot Design Using Fiber Reinforced Composites," *Journal of Mechanical Design*, Vol. 130, May 2008.
96. Wood, R.J., Steltz, E., and Fearing, R.S., "Optimal Energy Density Piezoelectric Bending Actuators," *Sensors and Actuators A*, Vol. 119, 476-488, 2005.
97. Woods, R.D., Liebst, B.S., Cobb, R.G., "A State-Space Model of a Large, Lightly Damped Space Structure". *Proceedings of the AIAA Guidance, Navigation and Control Conference*, Baltimore, MD, 1995, pp. 345-355.
98. Wu, P., and Ifju, P., "Experimental Methodology for Flapping Wing Structure Optimization in Hovering Flight of Micro Air Vehicles," AIAA Paper 2010-2709, April, 2010.
99. Xie, L., Wu, P., and Ifju, P., "Advanced Flapping Wing Structure Fabrication for Biologically-Inspired Hovering Flight," AIAA Paper 2010-2789, April, 2010.

100. Yang, T. M., and Hsiao, F. Y., "Dynamics of Flapping Micro Aerial Vehicles," *Proceedings of the American Control Conference*, St. Louis, Missouri, 2009.
101. Zdunich, P., Bilyk, D., MacMaster, M., Loewen, D., and DeLaurier, J., "Development and Testing of the Mentor Flapping Wing Micro Air Vehicle," *Journal of Aircraft*, Vol. 44, No. 5, September, 2007.

Vita

Michael L. Anderson is a Major in the United States Air Force, currently a PhD Candidate in Aeronautical Engineering at the Air Force Institute of Technology at Wright Patterson Air Force Base, Ohio. He has been researching small UAV's and MAV's since 2006, authoring several papers relevant to the field. He began his professional career in 1999, graduating with honors from the US Air Force Academy with a BS in Mechanical Engineering. He did sustainment engineering of F-16 flight control actuation systems at Hill Air Force Base, Utah before earning his MS in Mechanical Engineering from the University of Utah in 2004 where he researched design and control of quadruped robots. In 2004 he was assigned to the Air Force Academy where he taught courses in structures, dynamics, mechatronics and engineering design while researching small UAVs and MAVs. His research at the Academy focused on innovative design methodologies applied to UAV problems such as energy harvesting and perching. Major Anderson began his PhD program at AFIT in the Fall of 2008.

REPORT DOCUMENTATION PAGE				Form Approved OMB No. 074-0188	
<p>The public reporting burden for this collection of information is estimated to average 1 hour per response, including the time for reviewing instructions, searching existing data sources, gathering and maintaining the data needed, and completing and reviewing the collection of information. Send comments regarding this burden estimate or any other aspect of the collection of information, including suggestions for reducing this burden to Department of Defense, Washington Headquarters Services, Directorate for Information Operations and Reports (0704-0188), 1215 Jefferson Davis Highway, Suite 1204, Arlington, VA 22202-4302. Respondents should be aware that notwithstanding any other provision of law, no person shall be subject to a penalty for failing to comply with a collection of information if it does not display a currently valid OMB control number.</p> <p>PLEASE DO NOT RETURN YOUR FORM TO THE ABOVE ADDRESS.</p>					
1. REPORT DATE (DD-MM-YYYY) 16-09-2011		2. REPORT TYPE PhD Dissertation		3. DATES COVERED (From – To) Sept 2008 – Sept 2011	
4. TITLE AND SUBTITLE Design and Control of Flapping Wing Micro Air Vehicles				5a. CONTRACT NUMBER	
				5b. GRANT NUMBER	
				5c. PROGRAM ELEMENT NUMBER	
6. AUTHOR(S) Anderson, Michael L., Major, USAF				5d. PROJECT NUMBER 11Y270	
				5e. TASK NUMBER	
				5f. WORK UNIT NUMBER	
7. PERFORMING ORGANIZATION NAMES(S) AND ADDRESS(S) Air Force Institute of Technology Graduate School of Engineering and Management (AFIT/EN) 2950 Hobson Way WPAFB OH 45433-8865				8. PERFORMING ORGANIZATION REPORT NUMBER AFIT/DS/ENY/11-12	
9. SPONSORING/MONITORING AGENCY NAME(S) AND ADDRESS(ES) Air Force Research Lab, Air Vehicles Directorate Attn: Greg Parker (937) 255-7550 gregory.parker@wpafb.af.mil 24B 2145 Fifth Street WPAFB, OH 45433				10. SPONSOR/MONITOR'S ACRONYM(S) AFRL/RB	
				11. SPONSOR/MONITOR'S REPORT NUMBER(S)	
12. DISTRIBUTION/AVAILABILITY STATEMENT APPROVED FOR PUBLIC RELEASE; DISTRIBUTION UNLIMITED.					
13. SUPPLEMENTARY NOTES This material is declared a work of the U.S. Government and is not subject to copyright protection in the United States.					
14. ABSTRACT Flapping wing Micro Air Vehicles (MAVs) continues to be a growing field, with ongoing research into unsteady, low Re aerodynamics, micro-fabrication, and fluid-structure interaction. However, research into flapping wing control of such MAVs continues to lag. Existing research uniformly consists of proposed control laws that are validated by computer simulations of quasi-steady blade-element formulae. Such simulations use numerous assumptions and cannot be trusted to fully describe the flow physics. Instead, such control laws must be validated on hardware. Here, a novel control technique is proposed called Bi-harmonic Amplitude and Bias Modulation (BABM) which can generate forces and moments in 5 vehicle degrees of freedom with only two actuators. Several MAV prototypes were designed and manufactured with independently controllable wings capable of prescribing arbitrary wing trajectories. The forces and moments generated by a MAV utilizing the BABM control technique were measured on a 6-component balance. These experiments verified that a prototype can generate uncoupled forces and moments for motion in five degrees of freedom when using the BABM control technique, and that these forces can be approximated by quasi-steady blade-element formulae. Finally, the prototype performed preliminary controlled flight in constrained motion experiments, further demonstrating the feasibility of BABM.					
15. SUBJECT TERMS Micro Air Vehicle, Flapping Wing, Unmanned Air Vehicle, Flight Control, Aircraft Design, Micro Electro Mechanical Systems					
16. SECURITY CLASSIFICATION OF:			17. LIMITATION OF ABSTRACT UU	18. NUMBER OF PAGES 232	19a. NAME OF RESPONSIBLE PERSON Dr. Richard G. Cobb (ENY)
a. REPORT U	b. ABSTRACT U	c. THIS PAGE U			19b. TELEPHONE NUMBER (Include area code) (937) 255-3636, x4559 richard.cobb@afit.edu

